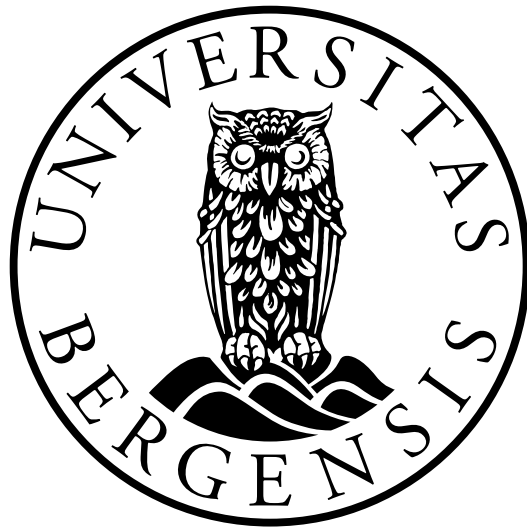


Exploring the Microseismicity of the Gakkel Ridge from Arctic Sea Ice

Gaute Hope

Thesis for the degree
Master of Science



DEPARTMENT OF EARTH SCIENCE
UNIVERSITY OF BERGEN

June 2013

"Vegen blir til medan ein går seg vill."

Fritt etter Dag Eyjenth (2000)

Abstract

Monitoring of microseismicity is an important tool to understand the magmatism, tectonics and hydrothermal circulation of a mid-oceanic ridge. In the presence of sea ice, use of ocean bottom seismometers is not practical, but several experiments with small networks of seismometers drifting with the sea ice have previously been completed successfully.

The goal of this project was to build on the earlier experiments and develop a method for monitoring the microseismicity above the Gakkel Ridge by developing seismic stations tailored for a small network on the Arctic sea ice. The new equipment has been taken from concept through development, building and deployment with data acquisition to data analysis. A 3D location algorithm was developed in order to locate a sample of the recorded events.

Five prototype seismic stations were designed, built and tested in a small network on the sea ice. The stations had individual timing and positioning, and were connected in a wireless network for real time transmission of position, status and data.

The network was deployed on the sea ice above the Gakkel Ridge at $85^{\circ}N$ during the *FRAM-2012* expedition to the Arctic Ocean with the hovercraft *R/H Sabvabaa* in July - September 2012. The network drifted over the rift valley along with the ice and two re-deployments were made, totalling 23 days of recording. The last of the three deployments (7 days) was the most successful, with three of the buoys fully operational. Although technical challenges had to be overcome due to the prototype nature of the equipment, it proved practical and functional.

The last deployment was analyzed and 41 events were identified. To account for the rough bathymetry at the Gakkel Ridge, a 3D grid search based location algorithm was developed, with which three of the events were located.

The prototype and the experiences from the deployment are presented together with an overview of the recorded data, the location algorithm, results from data analysis with the three event locations and interpretations.

Foreword

This master's thesis has been done at the Department of Earth Science, University of Bergen under the supervision of my advisors Yngve Kristoffersen, Lars Ottemöller and Henk Keers. Their comments, advice and concern are highly appreciated.

I would like to thank professor Kristoffersen for the opportunity to participate in an expedition with the hovercraft *R/H Sabvabaa* to the Arctic Ocean, for the months in the ice, the exercise in patience and the experiences. Without his *realistic optimism* I doubt any of it could have been done.

I would also like to thank Henk Keers for the useful discussions, the concern, and for his help and encouragement in pursuing my master's degree.

Furthermore, thanks to Lars Ottemöller for the concern, and the down to earth advice in this project.

I would also like to thank Ole Meyer for providing very helpful tips and encouragement throughout building and deploying the buoys.

Without Dr. John K. Hall we would still be on land, his polar passion has made *R/H Sabvabaa* reality.

Finally I would like to thank my fellow students for the good time, my family for the support, and Astrid for valuable comments and for sticking it out.

June 2013

Gaute Hope

Contents

| | |
|---|-----|
| Abstract | i |
| Foreword | i |
| Contents | i |
| List of Figures | vi |
| List of Tables | xii |
| 1 Introduction | 1 |
| 1.1 Extension of the Mid-Atlantic Ridge into the Arctic Ocean | 2 |
| 1.2 Gakkel Ridge - the diverging plate boundary in the Arctic Ocean | 3 |
| 1.3 Method | 8 |
| 1.3.1 Past microearthquake studies in an ice-covered ocean | 9 |
| 1.4 The new approach | 10 |
| 2 An Efficient Earthquake Location Algorithm | 12 |
| 2.1 Wave propagation | 12 |
| 2.2 Ray theory | 15 |
| 2.3 Locating seismic events | 16 |

| | | |
|----------|--|-----------|
| 2.3.1 | HYPOSEARCH - Hypocenter grid search routine for a 3D model | 17 |
| 2.3.1.1 | Algorithm | 18 |
| 2.3.1.2 | Ray tracing through layers with constant velocity | 18 |
| 2.3.1.3 | Error calculation | 22 |
| 2.3.1.4 | Matching to grid cells | 24 |
| 2.3.1.5 | Synthetic tests | 25 |
| 3 | The Seismic Station and Survey Outline | 31 |
| 3.1 | Microearthquake studies in an ice-covered ocean | 31 |
| 3.2 | Outline of the survey | 32 |
| 3.3 | Instrumentation | 34 |
| 3.3.1 | Analog to digital interface | 38 |
| 3.3.2 | The Station | 41 |
| 3.3.3 | Seismometer | 42 |
| 4 | The Field Experiment and Data Acquisition | 43 |
| 4.1 | Drift G1 | 45 |
| 4.2 | Drift G2 | 47 |
| 4.3 | Drift G3 | 49 |
| 4.4 | Technical observations | 50 |
| 5 | Data Analysis | 53 |
| 5.1 | Preparation and organization of recorded data | 53 |
| 5.2 | Data overview | 54 |
| 5.3 | Event discrimination and phase identification | 57 |
| 5.4 | Event types | 60 |

| | | |
|---|---|-----------|
| 5.4.1 | Weak event | 60 |
| 5.4.2 | Strong event | 62 |
| 5.5 | Seismometer | 63 |
| 5.6 | Ambient noise levels | 65 |
| 5.6.1 | Noise from Hovercraft | 68 |
| 5.6.2 | Cryogenic, human and discarded events | 70 |
| 5.7 | Locations | 72 |
| 5.7.1 | Event: 03-2300-00L.S201209 | 74 |
| 5.7.2 | Event: 04-1400-01L.S201209 and 04-1400-02L.201209 | 75 |
| 5.7.3 | Summary | 80 |
| 6 | Discussion and Conclusion | 82 |
| 6.1 | Evaluation of equipment and experiment | 82 |
| 6.2 | Results from acquisition | 84 |
| 6.3 | Location algorithm | 86 |
| 6.4 | Interpretation of event locations | 87 |
| 6.5 | Conclusion | 88 |
| 6.6 | Further work | 90 |
| Bibliography | | 92 |
| Appendices | | 98 |
| A The Buoy and Network - Concept and Specification | | 99 |
| A.1 | Overview | 99 |
| A.1.1 | Prototype and Goals | 100 |
| A.1.1.1 | Prototype | 100 |

| | | |
|---------|---|-----|
| A.1.1.2 | Goals | 100 |
| A.2 | Specification | 101 |
| A.2.1 | Analog components | 101 |
| A.2.1.1 | Power supply | 103 |
| A.2.1.2 | Buffer and decoupling | 105 |
| A.2.1.3 | Analog to digital converter | 105 |
| A.2.1.4 | Hydrophone | 106 |
| A.2.1.5 | Antenna | 106 |
| A.2.2 | Instrument response and analog analysis | 107 |
| A.2.2.1 | Derivation of transfer function | 107 |
| A.2.2.2 | Analysis | 108 |
| A.2.2.3 | Digital filter | 115 |
| A.2.2.4 | Hydrophone characteristics | 116 |
| A.2.3 | Digital components | 117 |
| A.2.3.1 | Main board with Central Processing Unit | 117 |
| A.2.3.2 | GPS | 118 |
| A.2.3.3 | Radio (RF) | 118 |
| A.2.3.4 | AD converter | 119 |
| A.2.3.5 | SD card | 119 |
| A.2.3.6 | Pin map | 119 |
| A.2.4 | Construction and assembly | 120 |
| A.3 | Operating system (OS) | 121 |
| A.3.1 | Storage | 121 |
| A.4 | Positioning and timing (GPS) | 121 |
| A.4.1 | Time representation | 122 |

| | | |
|----------|--|------------|
| A.4.2 | Determining time | 122 |
| A.4.2.1 | Assumptions | 122 |
| A.4.3 | Determining a new reference | 123 |
| A.4.4 | Accuracy | 123 |
| A.5 | Communication and network | 123 |
| A.5.1 | Central logging point | 123 |
| A.5.2 | Network Protocol | 124 |
| B | File Format | 126 |
| B.1 | Data structure and file format | 126 |
| B.1.1 | Entities | 126 |
| B.1.2 | Structure | 127 |
| B.1.2.1 | Index | 128 |
| B.1.2.2 | Reference: Timing, position and status | 128 |
| B.1.2.3 | Status | 129 |
| B.1.2.4 | Sample | 130 |
| B.1.3 | Formats | 130 |
| B.1.3.1 | Binary format: DAT | 130 |
| B.1.3.2 | ASCII format: DTT | 133 |
| B.1.4 | Data capacity budget | 135 |

List of Figures

| | |
|---|----|
| 1.2.1 (a) Distribution of earthquakes with magnitudes equal or larger than 3.5 and depths shallower than 40 km (1967-2007). (b) Plate boundaries. From DeMets <i>et al.</i> (2010). | 4 |
| 1.2.2 Spreading rates for the Arctic and north Atlantic basin (from DeMets <i>et al.</i> , 2010). | 5 |
| 1.2.3 Teleseismically recorded events from the West Gakkel Ridge 1955-1999 (from Engen & Eldholm (2003)). | 7 |
| 1.2.4 Teleseismically recorded events from the East Gakkel Ridge 1955-1999 (from Engen & Eldholm (2003)). | 7 |
| 1.2.5 Rock composition of samples collected during AMORE 2001 from the Gakkel Ridge segments (from Michael <i>et al.</i> (2003)). | 8 |
| 2.3.1 HYPOSEARCH algorithm outline | 19 |
| 2.3.2 Reflected and transmitted rays | 21 |

| | |
|---|----|
| 2.3.3 HYPOSEARCH matching grid cells to traced rays in region of interest. Blue rays are initial rays shot from station (black star at 0 m depth) onto the triangulation of the bathymetry (in blue, from IBCAO). The ray parameter of the refracted ray is determined by the angle of incidence of the incoming ray and the inclination of the matched triangle together with the velocity of the layers on each side of the interface (water layer in the case of the bathymetry). In the model used in this thesis all the interfaces below the bathymetry are horizontal (consisting of two triangles). However, they could be as complicated as the bathymetry, but at the cost of requiring more computation since more triangles need to be matched against rays. The blue boxes represents the grid cells that are matched to the ray (red) | 24 |
| 2.3.4 Error values at grid cells are plotted in increasingly hotter colors. Stations (green, black, yellow) are plotted along with the best match (cyan) and synthetic source (blue). Top plots only consider P and S phases, bottom plots uses P, S, M and MM for travel time differences. | 26 |
| 2.3.5 traveltimes plotted for distance between station GAK2 and synthetic source (at depth 5 km). | 28 |
| 2.3.6 traveltimes and differences plotted as function of depth at a distance of 2.8 km. | 29 |
| 2.3.7 traveltimes and differences plotted as function of depth at a distance of 14 km. | 30 |
| 3.2.1 Overview of network setup | 34 |
| 3.3.1 Buoy interior with components. Power regulators are located below the top layer (left). On the left top layer: main board, radio and GPS. On the right lower layer: the AD converter along with buffer and hydrophone decoupling. | 35 |
| 3.3.2 Diagram of operating system hierarchy. Components (control and drivers) (except SD card with FAT filesystem) inside gray box have been developed as part of this project. Minor modifications were made to the libmaple library and the SD/FAT library. | 37 |
| 3.3.3 Frequency response of complete analog system, equation A.2.9. | 39 |

| | |
|--|----|
| 3.3.4 The buoy connected to the hydrophone let through a hole in the ice with antenna mounted and the battery connected. The hydrophone cable in this picture is not yet covered in snow to avoid noise from wind. | 41 |
| 4.0.1 Drift track for all deployments, starting with the first drift in the east and progressing with westward component of the general ice drift. | 44 |
| 4.1.1 Drift path during G1. The path of station GAK1 quickly stopped as it had powered down. It was not picked up before the others. It can be seen that station GAK3 (located next to <i>RH Sabvabaa</i>) sporadically loses the GPS fix and the affected sections of the path is missing. | 45 |
| 4.1.2 Field experiment, from top left, clockwise: the <i>RH Sabvabaa</i> approaching a deployed buoy; melting hydrophone out of ice using hot water to avoid damage; buoy melted into ice and covered by fresh snow (we observed the red indicator light on the GPS blinking to signify full position and timing fix); computer acting as central logging point in the cabin of <i>RH Sabvabaa</i> | 47 |
| 4.2.1 Drift path during G2. The GPS problems resulted in no path for station GAK3 (yellow). | 48 |
| 4.3.1 Drift path during G3 | 49 |
| 4.3.2 Relocating the GPS device within the box was sufficient to mitigate GPS problems. | 50 |
| 5.3.1 Ray paths for event 04-1400-02L with IBCAO bathymetry from the side (top) and the top (bottom). | 59 |
| 5.4.1 Event 03-2200-00L filtered between 1 - 50 Hz (left) and 20 - 50 Hz (right) on stations GAK2 (top) and GAKS (bottom). | 60 |
| 5.4.2 Spectrogram of event 03-2200-00L for the individual stations (filtered above 8 Hz). | 61 |
| 5.4.3 Trace from station GAK2 of event 04-2000-00L.S201209 showing a possible T-phase tail. | 62 |

| | |
|---|----|
| 5.4.4 Trace of event 04-1400-01L.S201209, filtered between 1 - 50 Hz. Phase pickings are shown for the buoys. Station GAKS (the seismometer, bottom three traces) is located a few meters from station GAK2. | 62 |
| 5.4.5 Spectrogram of event 04-1400-01L (filtered above 8 Hz) for all stations. | 63 |
| 5.5.1 Seismometer failure, top: Seismometer failure due to drift or tilting. One of the horizontal components is unable to recover (the digitizer was resetting the seismometer if the output passes a set level for a predefined time). Bottom: Seismometer has been re-balanced manually and all components recover. | 64 |
| 5.6.1 PDF of power spectrum density for station GAK2 (2012-09-03). | 66 |
| 5.6.2 PDF of power spectrum density for station GAK2 (left) (2012-09-05) showing a 20 Hz peak and GAK4 (right) (2012-09-01) showing a small peak around 70 Hz | 66 |
| 5.6.3 PDF of power spectrum density for station GAK3 (2012-09-02). | 67 |
| 5.6.4 PDF of power spectrum density for station GAK4 (2012-09-02). | 68 |
| 5.6.5 Hovercraft engine noise spectrogram and trace. | 69 |
| 5.6.6 Hovercraft engine noise spectrogram and trace for all stations (both filtered above 8 Hz). | 70 |
| 5.6.7 Man-made noise, most likely man-made noise (green arrows) only recorded on seismometer and station GAK2 next to the hovercraft. | 71 |
| 5.6.8 Cryogenic and man-made noise, red arrows show cryogenic signals, green either man-made or cryogenic while blue is a time glitch resulting in a spike in the filtered data. The two events at the red arrows could be the same as are recorded slightly later on stations GAKS and GAK2, they are however not visible on station GAK3. The horizontal components of the seismometer show higher amplitude than for the vertical. | 72 |
| 5.7.1 Location for event 03-2300-00L. The triangles show the station locations at the time of recording, the stars show the solutions for the same event using HYPOCENTER (red), HYPOSEARCH (only considering P and SP phase) (blue), HYPOSEARCH (only considering P, SP and M phases) (cyan) and HYPOSEARCH (considering all phases) (black). | 74 |

| | |
|---|-----|
| 5.7.2 Location for event 04-1400-01L. The triangles show the station locations at the time of recording, the stars show the solutions for the same event using HYPOCENTER (red), HYPOSEARCH (only considering P and SP phase) (blue) and HYPOSEARCH (only considering P, SP and M phases) (cyan). | 76 |
| 5.7.3 Traces for the hydrophone stations of event 04-1400-01L.S201209 with phase pickings. The emergent character of the assumed SP phase is particularly visible in the top (GAK2) and bottom (GAK4) traces. | 77 |
| 5.7.4 Location for event 04-1400-02L. The triangles show the station locations at the time of recording, the stars show the solutions for the same event using HYPOCENTER (red), HYPOSEARCH (only considering P and SP phase) (blue) and HYPOSEARCH (only considering P, SP and M phases) (cyan). The blue and cyan star (HYPOSEARCH solutions) coincide and only the cyan star is displayed. | 79 |
| 5.7.5 All three located events, different color signifies different event (regional map). | 80 |
| 5.7.6 All three located events, different color signifies different event. | 81 |
| 6.4.1 Cross section of spreading ridge for a) an asymmetrical case and b) a symmetrical case (figure from Escartín <i>et al.</i> , 2008). | 88 |
| A.2.1 Complete wiring diagram for buoy, component symbols have only relevant pins drawn. | 102 |
| A.2.2 Suggested decoupling for hydrophone (AQ-18) (Teledyne Benthos, 2012a). . . | 105 |
| A.2.3 Hydrophone decoupling and buffer (equivalent circuit) | 107 |
| A.2.4 Bode plot of the transfer function for the buffer stage (equation A.2.5), showing peak response at 33.9 Hz. | 109 |
| A.2.5 Impulse response of complete analog system, equation (A.2.9). | 112 |
| A.2.6 Step response of complete analog system, equation (A.2.9). | 112 |
| A.2.7 Zoomed in step response of complete analog system, equation (A.2.9). . . . | 113 |
| A.2.8 Pole Zero map of the transfer function $H(s)$ from equation (A.2.9). | 114 |

| | |
|--|-----|
| A.2.9 Sinc filter response (from Texas Instruments, 2007). | 115 |
| A.2.10 FIR filter response (from Texas Instruments, 2007). | 115 |
| A.2.11 Frequency response plot of hydrophone (from 7 Hz, the hydrophone is however specified from 1 Hz), AQ-18, figure from Benthos (Teledyne Benthos, 2012c). | 117 |
| A.5.1 Screenshot of central logging point server, a client monitoring one buoy and MATLAB showing data as it is received. | 124 |

List of Tables

| | | |
|-----|---|-----|
| 2.1 | Synthetic velocity model | 25 |
| 2.2 | Positions for synthetic test | 25 |
| 2.3 | Synthetic traveltimes calculated by TauP | 27 |
| 2.4 | Traveltimes for best solution calculated by HYPOSEARCH | 27 |
| 5.1 | Initial number (left) and final number (right) of events for drift GAK3 . . . | 55 |
| 5.2 | Event P-arrival times for drift G3, continued below in table 5.3. | 56 |
| 5.3 | Event P-arrival times for drift G3 continued. | 57 |
| 5.4 | Velocity model used for locating events | 73 |
| 5.5 | Observed onset times and travel times calculated with HYPOSEARCH. . . | 78 |
| A.1 | Power budget | 104 |
| A.2 | Pin and wire map of components to the Olimexino STM32 H103 main board. | 120 |
| A.3 | Network protocol telegrams | 125 |
| B.1 | Store structure | 127 |
| B.2 | Status flag bit mapping | 129 |
| B.3 | Binary index file, fields, start and size are given in bytes. | 131 |
| B.4 | Binary reference, fields, start and size are given in bytes. | 132 |

| | | |
|-----|--|-----|
| B.5 | Binary batch, fields, start and size are given in bytes. | 132 |
| B.6 | Binary data file, fields, start and size are given in bytes. | 133 |
| B.7 | Local data capacity budget | 136 |

Chapter 1

Introduction

Monitoring of microseismicity is an important tool to understand magmatism, tectonic processes and hydrothermal circulation at a mid-oceanic ridge. For the Gakkel Ridge in the Arctic ocean, the slowest spreading ridge in the global system of mid-oceanic ridges, the presence of sea ice has made the use of ocean bottom seismometers impractical. To overcome this challenge, unconventional approaches to monitoring of seismic activity have been sought and to this end several experiments have been done with seismic networks on the drifting sea ice.

The purpose of this project was to further advance this method by developing seismic stations for a network designed for the Arctic environment. The network of stations were taken from concept through development to building and deployment above the Gakkel Ridge using a hovercraft.

The goal was further to determine the suitability of the method by evaluating the experiences from the deployment, analyzing the data and developing a 3D location algorithm to locate a sample of the recorded earthquakes. In this way the potential of the method is sought to be determined.

Five prototype seismic stations (buoys) for a small network were designed and built, with the intention of creating a practical and robust network. The stations had independent timing and position, and transmitted position and status as well as data wirelessly.

The network was deployed with a hovercraft during the FRAM-2012 expedition (July -

September 2012) and recorded data above the Gakkel Ridge for a total of 23 days, of which the last 7 days were the most successful.

The topography of the Gakkel rift valley is extreme, with valley walls sloping 20-30° towards an axial valley 1-2 km wide. In order to locate the recorded seismic events, it was deemed necessary to develop a location algorithm which takes this rough bathymetry into account.

In this thesis, the method is evaluated and the potential of the recorded data is explored. The experiences from the deployment of the seismic network are presented together with the recorded data, the location algorithm, results from the data analysis and the results from locating three of the events.

1.1 Extension of the Mid-Atlantic Ridge into the Arctic Ocean

Topography rising above the abyssal plain along the center of the Eurasia Basin was first recognized from spot soundings by Elmendorf & Heezen (1957) and the association of this topography with seismicity suggested to Heezen & Ewing (1961) a link to the North Atlantic mid-ocean ridge system. Sykes (1965) studied telesismically recorded earthquakes from the growing number of stations around the Arctic, and was able to see a remarkably narrow and straight belt (50 km wide) across the Eurasian basin, typical of mid-oceanic ridges.

The first continuous bathymetric profiles across the ridge were obtained (by the pioneer crossings of the polar basin) by nuclear submarines Nautilus in 1957 (Dietz & Shumway, 1961) and Skate (Johnson & Eckhoff, 1966). More bathymetric data was subsequently published by Vogt *et al.* (1979), Feden *et al.* (1979), Kristoffersen *et al.* (1982) and Johnson *et al.* (1990).

Modern multi-beam swath mapping of the Gakkel Rift valley (0°E and 60°E) by an ice-breaking vessel in 1991 Jokat *et al.* (1995), heralded a new era in deep Arctic Ocean exploration, providing bathymetric charts of the Gakkel Ridge. This mapping were followed in 1999 by the innovative Science Ice Exercise (SCICEX) program utilizing nuclear submarines (Edwards & Coakley, 2003) and culminated with the joint Arctic Mid-Ocean Ridge Expedition (AMORE) which used two icebreakers with swath mapping capabilities (Michael *et al.*, 2003) to cover the rift valley for about 1000 km of the 1800 km long ridge.

The name Gakkel Ridge was adopted by the Russian Geographical Society in 1966 in honor of the Soviet geologist Ya. Ya. Gakkel (Naryshkin, 1987).

1.2 Gakkel Ridge - the diverging plate boundary in the Arctic Ocean

The seismicity at the Gakkel Ridge is an expression of divergence between the European and North American lithospheric plates (Figure 1.2.1). The motion is described by a pole of rotation currently located at $62^{\circ}N$, $140^{\circ}E$ in northern Siberia, due south of the Laptev Sea (DeMets *et al.*, 2010). The opening rate is less than 15 mm/year (figure 1.2.2) and it makes the Gakkel Ridge an ultra-slow spreading center in the global system of mid-ocean ridges (Dick *et al.*, 2003).

Engen & Eldholm (2003) generated an Arctic Catalog of 1189 earthquakes north of $72^{\circ}N$ for the period January 1955 to December 1999 mostly using the source catalogs from Engdahl *et al.* (1998) and Sykes (1965). A compilation of the seismicity of the Gakkel Ridge by Engen & Eldholm (2003) is shown in figure 1.2.3. The modern detection level of the global seismograph network varies between magnitudes Ms 3.3-3.6 and is about Ms 3.4 at the western Gakkel Ridge.

The principal selection criteria of Engen & Eldholm (2003) required an event to be recorded by ≥ 12 stations and the surface wave magnitude to exceed 3.0. While these criteria corresponds to a statistical mean location error of 10 km (Engdahl *et al.*, 1998), real errors commonly exceed 15 km in the Eurasia Basin. This is primarily caused by a large azimuthal gap towards Asia in the distribution of recording stations (Engen & Eldholm, 2003). Therefore the location error is comparable to the width of the narrow rift valley.

The majority of epicenters are confined to and distributed along the Gakkel rift valley, but a few locations fall on the inward facing slope of the crestal mountains (Figure 1.2.3). Events within the 45 year time span of the Arctic Catalog show a tendency toward clustering, notably at $31^{\circ}E$, $85^{\circ}E$, $96^{\circ}E$, $114^{\circ}E$ and possibly several other locations. An earthquake swarm of 252 teleseismically recorded events of body-wave magnitude 3.2-5.8 occurred between $72^{\circ}E$ and $90^{\circ}E$ during the first half of 1999, and has in part been related to a volcanic eruption which covered about 40 km^2 of the rift valley floor (Müller & Jokat, 2000; Edwards

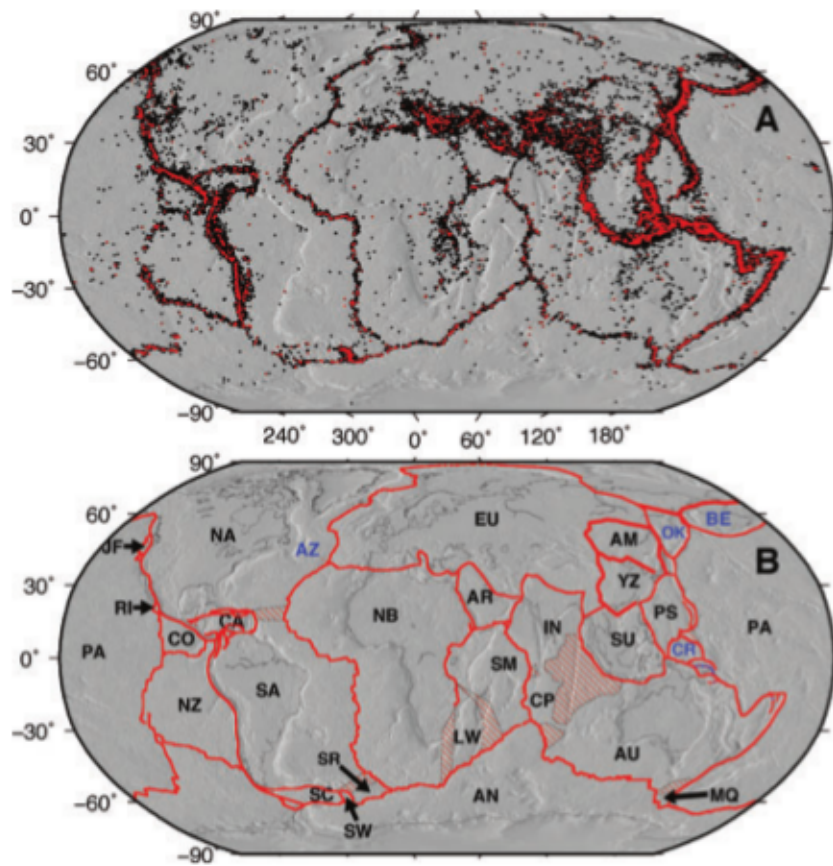


Figure 1.2.1: (a) Distribution of earthquakes with magnitudes equal or larger than 3.5 and depths shallower than 40 km (1967-2007). (b) Plate boundaries. From DeMets *et al.* (2010).

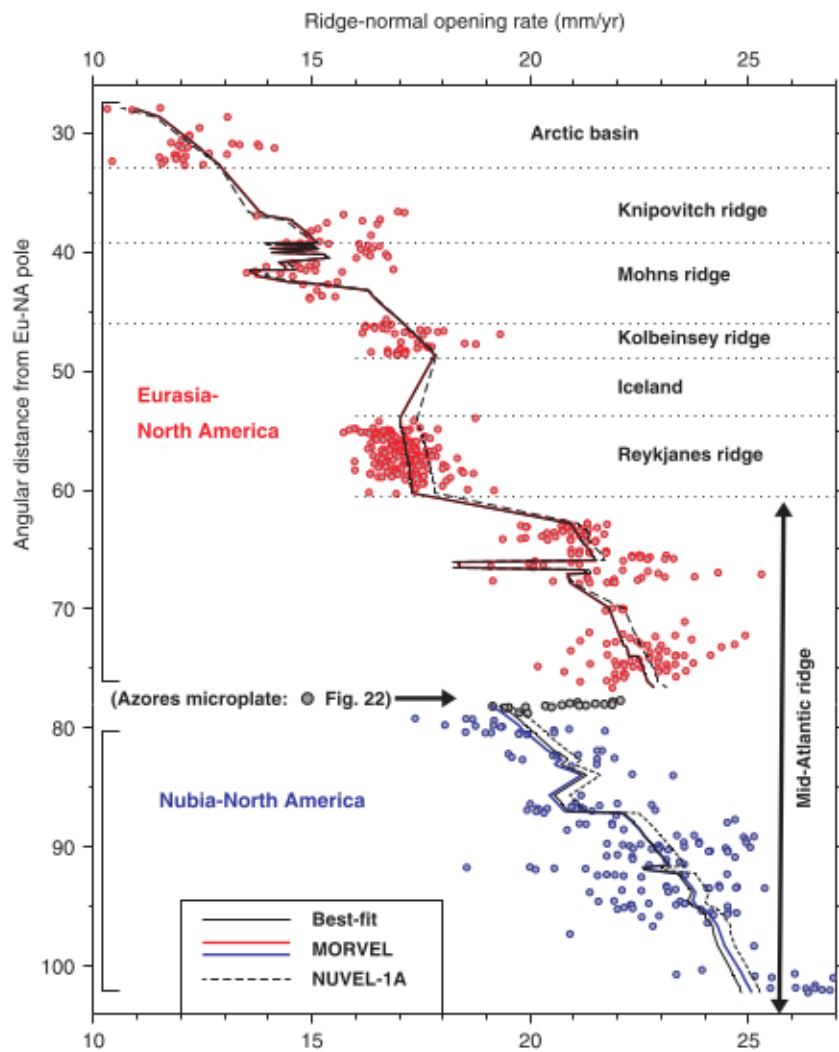


Figure 1.2.2: Spreading rates for the Arctic and north Atlantic basin (from DeMets *et al.*, 2010).

et al., 2001; Tolstoy *et al.*, 2001). Gaps in the teleseismically recorded earthquakes are present at the far western end of the Gakkel spreading center, at $3^{\circ} - 11^{\circ}E$ and $15^{\circ} - 28^{\circ}E$ (Figure 1.2.3).

The majority of the focal mechanisms of the earthquakes show normal faulting (Figure 1.2.4). The dominance of normal faulting is also reflected by the linear bathymetric expression of the Gakkel spreading center, with no significant offsets of the axial valley.

At a spreading center, the accommodation space generated by divergent plate motion may be compensated by magmatic and/or amagmatic tectonic processes. The AMORE expedition in 2001 sampled rocks and carried out a suite of other investigations at about 200 localities along more than half of the total length of the Gakkel spreading center. Surprisingly, the recovered rock types indicate that melt production and volcanism at the ultraslow spreading center do not scale down directly with an eastward decreasing opening rate.

The surveyed ridge section can be divided into three provinces: abundant volcanism in the relatively fast spreading western zone ($7^{\circ}W - 3^{\circ}E$); the relatively slowest spreading eastern zone ($29^{\circ}E - 85^{\circ}E$) with focused volcanism from large centers spaced 50-160 km apart; and in between, a central section of the rift valley, 300 km long ($3^{\circ}E - 29^{\circ}E$), where peridotites are abundant on the sea floor (Michael *et al.*, 2003). This is a “sparsely magmatic” zone sandwiched in between two magmatic ridge sections. This magmatic segmentation occurs in the absence of any tectonic segmentation of the lithosphere and is interpreted as evidence for the importance of magmatic segregation processes in the upper mantle (Michael *et al.*, 2003).

Note in particular the correspondence between the apparent gap in seismicity of the section of the axial valley at $3^{\circ}E - 11^{\circ}E$ as recorded by the global seismograph network, and the lack of magmatic products recovered from the sea floor, but rather ultramafic peridotite in abundance within the same section (Figure 1.2.3 and Figure 1.2.5). Observation and interpretation of the implied amagmatic and tectonic processes in this area is the subject of the field work of this master thesis study.

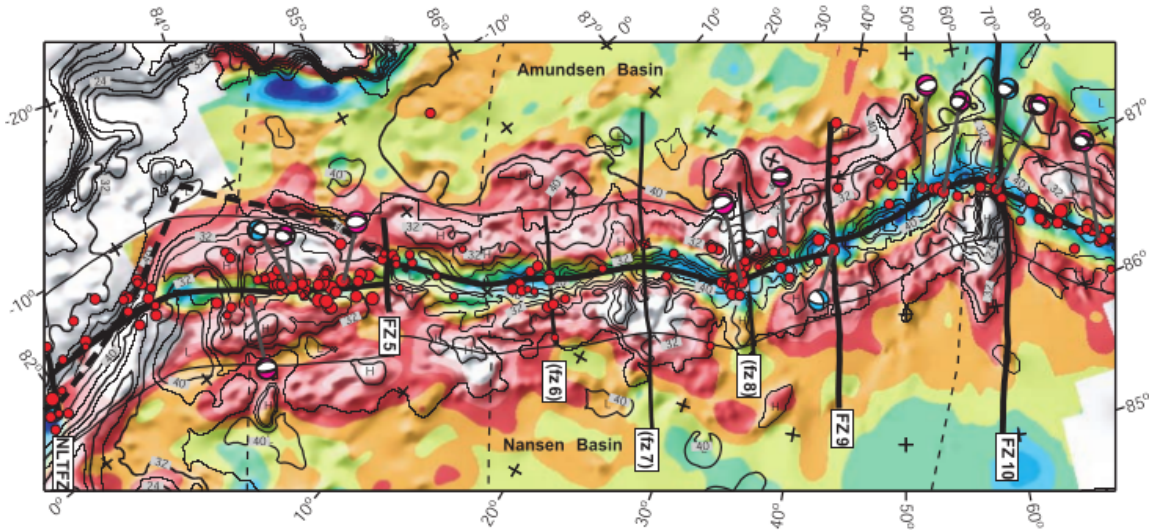


Figure 1.2.3: Teleseismically recorded events from the West Gakkel Ridge 1955-1999 (from Engen & Eldholm (2003)).

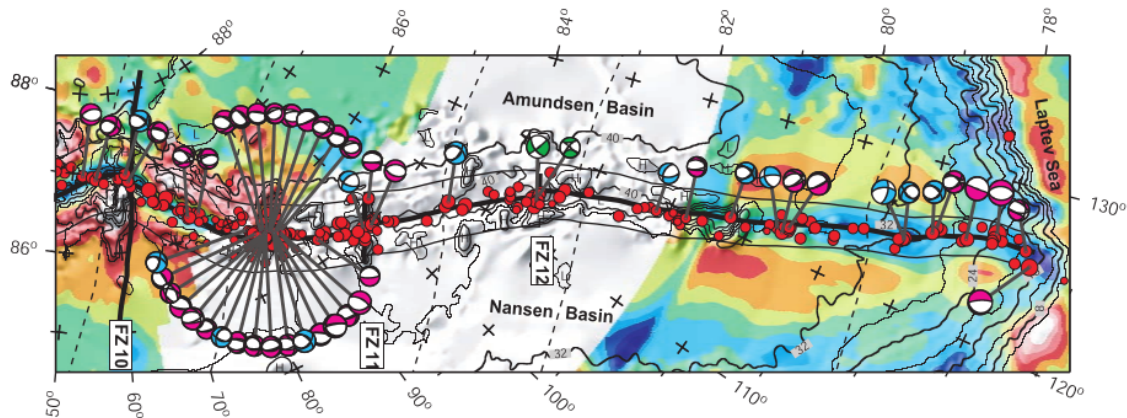


Figure 1.2.4: Teleseismically recorded events from the East Gakkel Ridge 1955-1999 (from Engen & Eldholm (2003)).

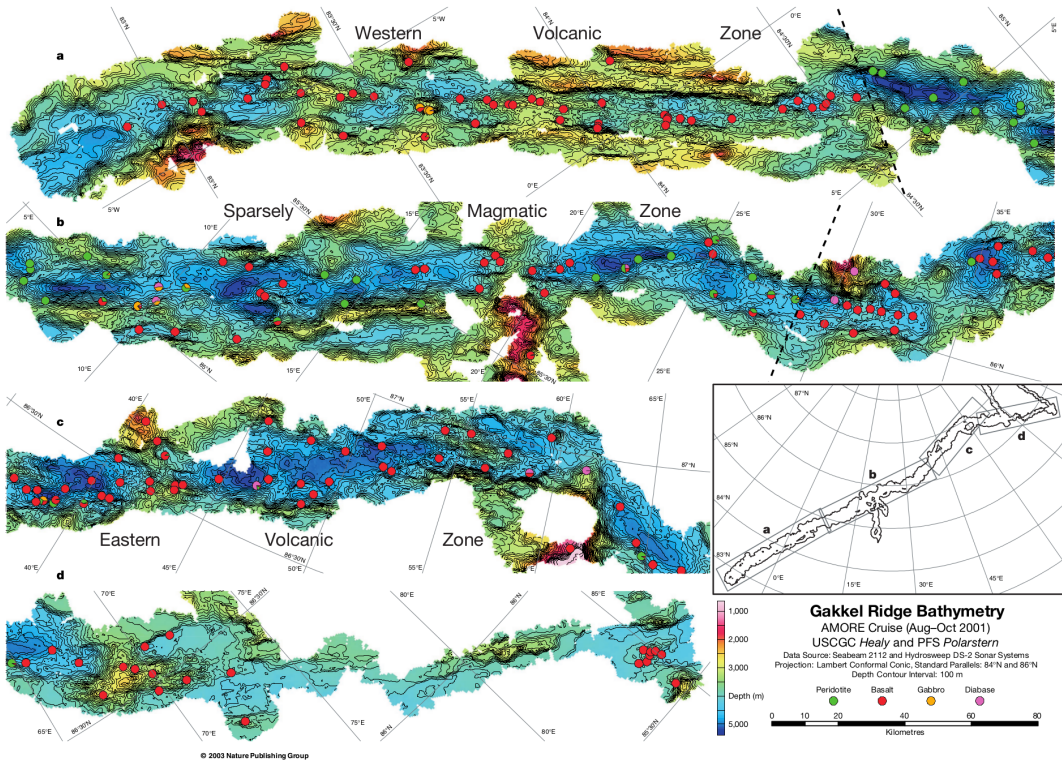


Figure 1.2.5: Rock composition of samples collected during AMORE 2001 from the Gakkel Ridge segments (from Michael *et al.* (2003)).

1.3 Method

The microseismic signals from magmatic, tectonic and hydrothermal processes of mid-oceanic ridges are largely too weak to be recorded by the nearest land-based seismic stations. A microseismic study is therefore part of a comprehensive study of the ultra-slow spreading mid-oceanic Gakkel Ridge to understand these processes.

The conventional method for performing a microseismic study at a mid-oceanic ridge is by deploying Ocean Bottom Seismometers (OBS), serviced from ships. However, the all-year Arctic sea ice prevents their recovery, creating a need to see new approaches in studying the microseismicity of the Gakkel Ridge.

1.3.1 Past microearthquake studies in an ice-covered ocean

In 1979 a 4 km long array of six modified military sonobuoys (AN-SSQ-41) was deployed on drifting sea ice and operated continuously for six weeks in April-May while the FRAM-I ice station drifted 200 km from the north on to the flank of the Gakkel Ridge (Kristoffersen *et al.*, 1982). From a total of 60 identified earthquakes, 21 events with magnitudes in the range of mb 1 to 4 could be located at a distance of 15-100 km within the Gakkel Rift valley. By using records from seismometers in northeastern Greenland and Svalbard, the earthquakes could be located to within 4 to 10 km.

Another approach is to use seismometers on the ice instead of hydrophones in the water. Läderach & Schlindwein (2011) deployed small arrays of modern seismometers on the drifting sea ice during AMORE 2001 and the following AGAVE 2007, LENA 2008 and LENA 2009 expeditions. The first experiment during AMORE 2001, close to the $85^{\circ}N$, $85^{\circ}E$ volcanic complex, showed that it was possible to record large amounts of acoustic signals from the ongoing volcanic eruption, and to record low-magnitude local seismicity by using seismometers deployed on the sea ice.

The procedure used by Läderach & Schlindwein (2011) involved deploying a small array of 3-4 broadband seismometers on the ice using a helicopter from an icebreaker. Individual stations were up to 1-2 km apart on a single ice floe to maintain the array geometry. Because the drifting ice largely dictates what is possible, the choice of array geometry may not be ideal.

The ice drifts up to 10-20 km/day, so depending on the drift direction relative to the axial valley, redeployment may be needed after 4-5 days or, in favorable conditions, after up to 15 days. Helicopter flights were dependent on the difficult weather conditions of the Arctic. Moreover, weight limitations and flight range (often limited distance away from the host icebreaker) require careful planning of deployment and recovery.

Each station in these recent experiments consisted of a seismometer, a data logger with GPS, several batteries and an ARGOS buoy. The ARGOS buoy was powered by a separate battery and was used to track the array drift for recovery (transmits the position each hour). The equipment for each station fit into one aluminum Zarges box and weighed about 70 kg. For each station two to three 80 Ah batteries were required for power. The seismometer was mounted on a plywood plate painted white to avoid melting into the ice which would

cause tilting of the seismometer. The seismometer was covered in snow to prevent tilt from melting or signal drift due to temperature changes. Installation and setup took about 30 minutes with the help of the helicopter pilot. The system was then quickly checked, but there was no time for on-site calibration.

These stations were able to operate for about 20 days at temperatures around $0^{\circ}C$. Upon recovery, the seismometers usually showed a tilt of about 0.5° . Only the center station required an ARGOS transmitter, since suitable, stable, multi-year ice floes were chosen and the station geometry remained constant. For the experiments AGAVE 2007 and LENA 2008, three arrays were deployed in a small drifting network on different ice floes.

The weight of the equipment, although relatively light compared to a land based station or an Ocean Bottom Seismometer (200 to 500 kg) (OBSIP, 2013), is still considerable with the available logistics.

1.4 The new approach

This project was based on the earlier methods of hydrophone arrays (Kristoffersen *et al.*, 1982) and seismometers on ice (Schlindwein *et al.*, 2007). Five prototype seismic stations to be operated in a small network (2 - 5 km diameter) on the sea ice were designed and built.

Each station consisted of a combined digitizer and control unit, built by the author as part of this project. The digitizer was connected to a hydrophone that is let through a hole in the ice. A 3-component seismometer was deployed with one of the stations for comparison as well as to exploit the horizontal components to discriminate between cryogenic events and the more vertical incident seismic events (Läderach & Schlindwein, 2011).

The stations and network were quick to deploy, and were connected in a wireless network for transmission of position, status and real-time transfer of data.

The network was deployed with the hovercraft *R/H Sabvabaa* during the FRAM-2012 expedition (July - September 2012). The stations were installed on the ice upstream, north of the rift valley at the Gakkel Ridge. The first deployment was done at approximately $11^{\circ}E$, and two re-deployments were made to maintain proximity to the rift valley. The third and last deployment was the most successful and was done above some of the deepest parts of

the Gakkel Ridge at approximately $3^{\circ} E$. All three deployments were in the westernmost part of the sparsely magmatic zone of the Gakkel Ridge.

Chapter 2

An Efficient Earthquake Location Algorithm

When an earthquake occurs energy is released. Much of this energy propagates in the form of waves that spread throughout the Earth. Some of this energy finds its way to the surface of the Earth where it can be recorded by seismic instruments, as in the experiment described in this thesis.

These recordings can be used to study both the Earth structure and the earthquake (for example the location, timing and mechanism of the earthquake). In this chapter it is briefly described how the waves generated by an earthquake propagate and how these recordings can be used to determine the location of an earthquake.

2.1 Wave propagation

Seismic waves propagating through an elastic medium satisfy the equation (e.g. Aki & Richards (1980); Pujol (2003)):

$$\rho \ddot{\mathbf{u}} = \nabla \cdot \boldsymbol{\tau} + \mathbf{f} \quad (2.1.1)$$

or, in component form:

$$\rho \frac{\partial^2 u_i}{\partial t^2} = \partial_j \tau_{ij} + f_i \quad (2.1.2)$$

Here \mathbf{u} is the seismic displacement, ρ is the density, τ is the stress tensor and \mathbf{f} denote the body forces. Using Hooke's law the components of the stress tensor in an isotropic medium, characterized by the Lame's parameters μ and λ , are given as:

$$\tau_{ij} = \lambda \delta_{ij} \partial_k u_k + \mu (\partial_i u_j + \partial_j u_i) \quad (2.1.3)$$

Inserting this in the wave equation, equation 2.1.1, gives:

$$\rho \ddot{\mathbf{u}} = (\lambda - 2\mu) \nabla \nabla \cdot \mathbf{u} - \mu \nabla \times \nabla \times \mathbf{u} \quad (2.1.4)$$

Given a body wave source and a medium characterized by ρ , μ and λ , which all three are functions of \mathbf{x} one of the main tasks in seismology is to solve this equation (2.1.4), i.e. to find the wavefield caused by the earthquake. In principle this can be done numerically using for example a finite difference method. However, this is in general very computationally expensive. This is especially so for cases where there is a complex and steep topography, such as the Gakkel rift valley, as this requires a very fine grid to accurately model the curved interfaces. If the grid is too coarse then the steep and changing bathymetry will generate artificial diffractions from the gridded interface.

A computationally less intensive approach is to trace the wave front using rays. For this we rewrite the wave equation. We can express the displacement \mathbf{u} from the wave equation 2.1.4 in terms of potentials. First we express the equation in terms of P-wave velocity, α , and S-wave velocity, β :

$$\alpha^2 = \frac{\lambda + 2\mu}{\rho} \quad (2.1.5)$$

$$\beta^2 = \frac{\mu}{\rho} \quad (2.1.6)$$

$$\ddot{\mathbf{u}} = \alpha^2 \nabla \nabla \cdot \mathbf{u} - \beta^2 \nabla \times \nabla \times \mathbf{u} \quad (2.1.7)$$

By using the Helmholtz decomposition theorem, we express displacement \mathbf{u} by the P-wave scalar potential (ϕ) and S-wave vector potential (ψ):

$$\mathbf{u} = \nabla\phi + \nabla \times \psi \quad (2.1.8)$$

since $\nabla \cdot \nabla \times \psi = 0$, the P wave displacement is given by the gradient of:

$$\nabla \cdot \mathbf{u} = \nabla^2\phi \quad (2.1.9)$$

and S wave displacement is given by the curl of ψ :

$$\nabla \times \mathbf{u} = -\nabla^2\psi \quad (2.1.10)$$

since $\nabla \times (\nabla\phi) = 0$. By similarly separating equation 2.1.4 into the scalar field, P-wave, and vector field, S-wave, and rewriting it in terms of the potentials from equation 2.1.9 and 2.1.10 we arrive at equations (e.g. Pujol, 2003; Shearer, 2009):

$$\nabla^2\phi = \frac{1}{\alpha^2} \frac{\partial^2\phi}{\partial t^2} \quad (2.1.11)$$

$$\nabla^2\psi = \frac{1}{\beta^2} \frac{\partial^2\psi}{\partial t^2} \quad (2.1.12)$$

which describe the wave propagation in terms of potential, and in the case of the P-wave (equation 2.1.11): acoustic pressure.

If we apply the Fourier transform to the equation 2.1.11, we arrive at the wave equation in the frequency domain:

$$\nabla^2\phi(\mathbf{x}, \omega) - \frac{\omega^2}{\alpha(\mathbf{x})^2}\phi(\mathbf{x}, \omega) = 0 \quad (2.1.13)$$

Known as the *Helmholtz* equation, it describes the pressure field ϕ of \mathbf{x} and for frequency, f , $\omega = 2\pi f$.

2.2 Ray theory

If solution of the form:

$$\phi(\omega) = A(\mathbf{x})e^{-i\omega[T(\mathbf{x})]} \quad (2.2.1)$$

is assumed, where T is the phase factor and A is the amplitude, then the problem of solving the wave equation is transformed into the problem of solving for T and A . Expanding the spatial and temporal derivatives for ϕ and substituting into equation 2.1.11, we obtain:

$$\nabla^2 A - \omega^2 A |\nabla T|^2 - i[2\omega \nabla A \cdot \nabla T + \omega A \nabla^2 T] = -\frac{A\omega^2}{\alpha^2} \quad (2.2.2)$$

For large ω (high frequencies) solving for $|\nabla T|^2$ the equation 2.2.2 reduces to:

$$|\nabla T|^2 = \frac{1}{\alpha^2} \quad (2.2.3)$$

This equation is known as the *eikonal* equation. A similar equation may be derived for the S-wave using the velocity β . The phase factor T , may also be described as the travel time function. The wavefront is now defined by the surfaces on which $T(\mathbf{x})$ is constant. Rays are the lines perpendicular to these surfaces and thus point in the direction of $\nabla T(\mathbf{x})$. In practice one can either solve the above eikonal equation or the equivalent equations for the raypaths (e.g. Cerveny, 2005). One advantage of doing the latter is that multiple arrivals (caused by crossing of the wavefront surfaces) can be taken into account. The ray equations are:

$$\frac{d\mathbf{x}}{dt} = \alpha^2 \nabla \mathbf{p} \quad (2.2.4)$$

$$\frac{d\mathbf{p}}{dt} = -\frac{1}{\alpha} \nabla \alpha \quad (2.2.5)$$

with initial conditions $\mathbf{x}(0) = \mathbf{x}_s$ and $\mathbf{p}(0) = \mathbf{p}_0$ where \mathbf{x}_s is the source (earthquake) location and \mathbf{p}_0 is the direction in which the ray leaves the source. The traveltime along the ray path now is the independent parameter t . In the smoothly varying part of the medium the

ray equations may be solved using standard algorithms for solving ordinary differential equations (such as Runge-Kutta algorithms). At interfaces the rays are refracted according to Snell's law:

$$\frac{\sin(\theta_1)}{v_1} = \frac{\sin(\theta_2)}{v_2} \quad (2.2.6)$$

where θ_1 and v_1 are the incidence angle and velocity in the layer and θ_2 and v_2 are the exit angle and velocity in the next layer.

In this thesis the velocity model consists of a number of layers with constant velocity, but with possibly undulating interface (especially the bathymetry). In this case the ray paths consist of straight line segments in the layers that are refracted according to Snell's law.

It should be noted that the ray path will be very sensitive to strong topography of an interface or discontinuities in the velocity model, this means that phenomena like diffraction are very hard to model with ray tracing and these cases also may create chaotic ray behavior.

For the purpose of locating an earthquake source, one of the main goals of the expedition described in this thesis, the ray paths of the seismic phases we observe must be determined. These are the direct P-wave, the S-wave converted to P-wave at seafloor (transverse waves can not propagate in a fluid and the energy will either be converted to longitudinal energy or be reflected), the P-wave reflected at the surface and at the seafloor (first multiple and the second P-wave reflection (second multiple)). In the next section an algorithm is given that traces these rays and uses the traveltimes of the rays to locate the earthquake.

2.3 Locating seismic events

The rough topography of the Gakkel Ridge, with the steep rift valley with sides sloping at 20-30° angles presents challenges for many existing iterative hypocenter algorithms which do not take the topography into account. A valley floor deeper than 5500 meters, in contrast to the valley flanks with seamounts that reach heights of less than 2000 meters below sea level, will strongly affect the wave propagation and cause chaotic ray behavior for reflected rays. Correct determination of the ray paths of the phase arrivals at each station is imperative to accurately locating the hypocenter of recorded events.

Algorithms exist for 3D velocity models based on grid searches (e.g. Oye & Roth (2003)), however normally the stations are located at a fixed position, and ray paths may be pre-computed for all grid cells for all stations and are re-used for all events.

In the case of this experiment the position of the stations changes continuously, hence this optimization cannot be done. Therefore an initial location is found using a simpler 1D iterative method like HYPOCENTER or HYPOSAT and then a 3D grid search solver which searches the constrained region is applied.

2.3.1 HYPOSEARCH - Hypocenter grid search routine for a 3D model

In order to be able to account for the strong topography at the rift valley a new localization routine (HYPOSEARCH) was written, which makes use of the IBCAO bathymetry (Jakobsson *et al.*, 2012) and supports a simplified 3D velocity model. It works as an enhanced brute force grid search by interpolating new ray parameters from initially guessed ray parameters, in order to achieve better coverage and constrain the number of unnecessary traced rays. It is written in MATLAB.

An initial attempt using a continuous velocity model and a Runge-Kutta ODE solver for the ray equations 2.2.4 and 2.2.5 was abandoned because of uncertainties in model parameters and the computational requirements.

The HYPOSEARCH routine accepts a model of an arbitrary number of 3D interfaces defined on a Cartesian grid (using e.g. UPS coordinates), with a layer defined by its two bounding interfaces. Each layer may only have constant velocities, so that Snell's law (equation 2.2.6) is sufficient for tracing the rays.

The ray path and their traveltimes for the phases P (direct upgoing wave), SP (S to P converted phase at the seafloor), first water multiple of P and second multiple of P are calculated. The phases are hereafter referred to as P, SP, M and MM respectively.

This limitation in the velocity model allows theoretical rays to be computed faster, while still maintaining a model which matches the bathymetry and velocity structure with a similar level of accuracy as they are presently known. For this implementation the interfaces may not intersect each other.

The interfaces are defined at arbitrary points as a function of depth. The points are triangulated using Delaunay triangulation (e.g. . de Berg *et al.*, 2008) so that the interface is represented internally as a continuously piecewise set of discrete triangles.

HYPOSEARCH is written to compute rays in parallel, for stations and phases, allowing the computation to be distributed on the same number of CPUs as the total number of phases: $3 \times 4 = 12$ CPUs which significantly reduces computation time.

2.3.1.1 Algorithm

Figure 2.3.1 shows the outline of the HYPOSEARCH algorithm. A HYPOSAT solution or equivalent is used as an initial guess for the earthquake location to determine the needed extent of the model and the grid cell size.

A region of interest can be specified as any arbitrary shape (following for instance the bathymetry) and can be limited to cover only a region of the model. This limited region is divided in a grid of rectangular boxes. The size of the cells determines the accuracy of the ray tracer, since any ray hitting the cell boundaries (box) is considered a solution for the center point of the grid cell. This approximation results in some inaccuracy.

All coordinates are specified in a Cartesian system for direct usage with UPS coordinates (which the IBCAO bathymetry is given in), but it can be used on any reference grid. The interfaces can even be spherical (discretized) if the distances are great enough so that the flat earth model no longer is valid.

2.3.1.2 Ray tracing through layers with constant velocity

Since the layers have constant velocity the problem of tracing a ray is reduced to determining where the ray intersects the interface (to calculate the inclination of the interface and angle of incidence) and applying Snell's law (equation 2.2.6) to determine the transmitted ray as well as calculating the reflected ray.

Although the rays travel from the source to the stations, the rays are attempted to be traced backwards from the station to all possible grid cells in the region of interest, so that the two-point ray path can be calculated using less computations.

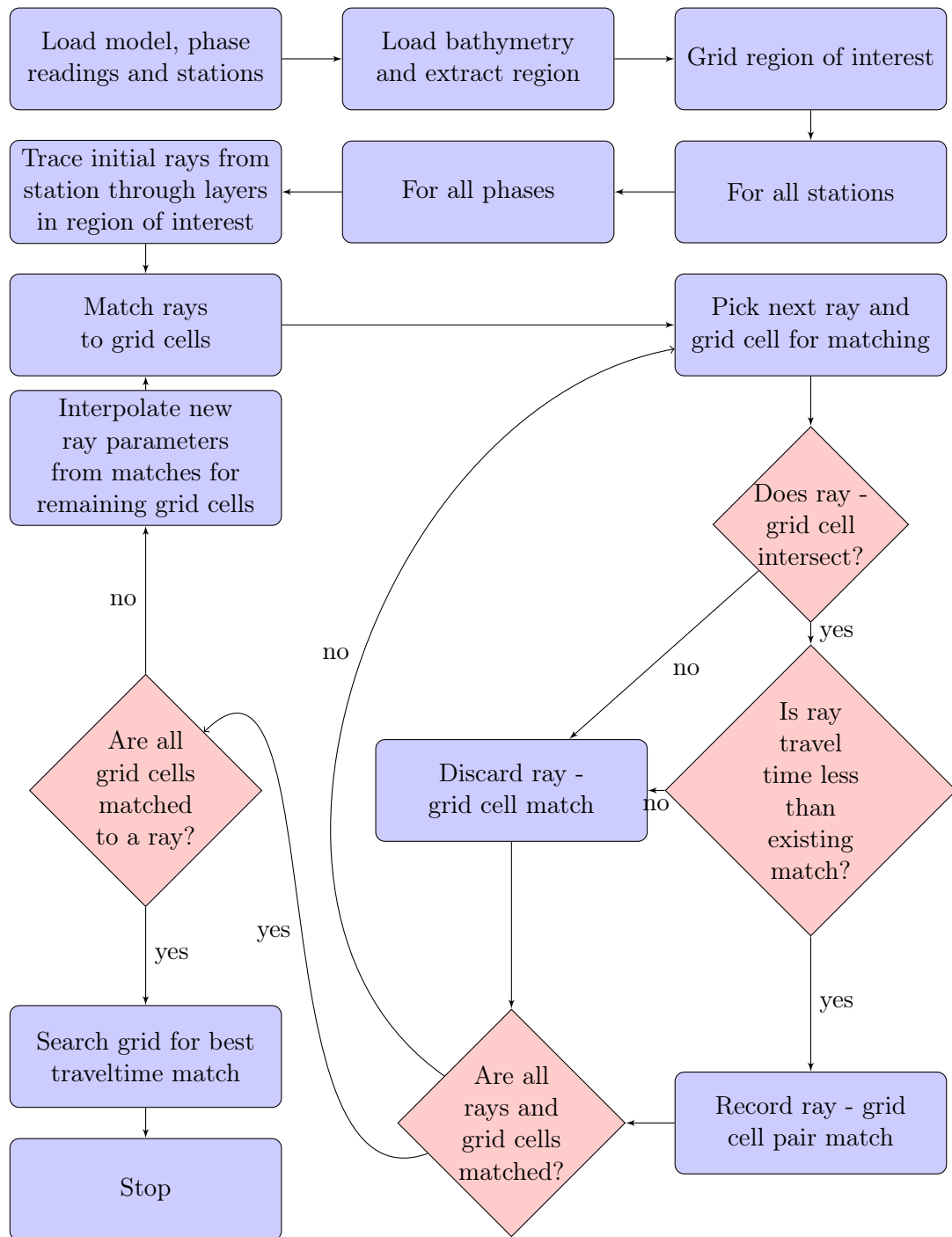


Figure 2.3.1: HYPOSEARCH algorithm outline

The rays are represented by their take-off parameters, azimuth (ϕ) and polar angle (θ), and may be expressed in vectorized form as:

$$\bar{\mathbf{p}} = \begin{bmatrix} x \\ y \\ z \end{bmatrix} = \begin{bmatrix} \cos(\phi) \times \sin(\theta) \\ \sin(\phi) \times \sin(\theta) \\ \cos(\theta) \end{bmatrix}$$

Where $\bar{\mathbf{p}}$ is the unit direction vector of the ray, which when multiplied with slowness gives the ray parameter.

In the case of initial shots being calculated from a grid on the seafloor, the take-off vector and parameters are calculated from the station $\bar{\mathbf{s}}$ and the point on the grid $\bar{\mathbf{g}}$, $\bar{\mathbf{p}} = \frac{\bar{\mathbf{g}} - \bar{\mathbf{s}}}{\|\bar{\mathbf{g}} - \bar{\mathbf{s}}\|}$, where the spherical parameters of $\bar{\mathbf{p}}$ may be derived from:

$$\begin{aligned} \theta &= \arccos(z) \\ \phi &= \arctan\left(\frac{y}{x}\right) \quad \left\{ \phi \in \langle -\pi, \pi \rangle \right. \end{aligned}$$

The spherical parameters are stored so that interpolation of the ray (spherical) parameters to new grid cells can be done simpler and be better determined (since of the three components of the vector $\bar{\mathbf{p}}$ there are only two independent parameters).

The next step in the tracer is to determine with which triangle (if any) the ray intersects. When a triangle ray intersection is found, the direction vector of the reflected ray ($\bar{\mathbf{r}}$, figure 2.3.2) of the P-wave is calculated from (Keers *et al.*, 1997):

$$\bar{\mathbf{r}} = 2(-\bar{\mathbf{p}} \cdot \bar{\mathbf{n}})\bar{\mathbf{n}} + \bar{\mathbf{p}}$$

where $\bar{\mathbf{n}}$ is the normal to the triangle. $\bar{\mathbf{n}}$ can be calculated as the cross product of any two vectors created by its vertices and $\bar{\mathbf{p}}$ is the normalized direction vector of the incoming ray.

The direction of the transmitted ray ($\bar{\mathbf{t}}$, Figure 2.3.2) is calculated from a vectorized form of Snell's law (e.g. de Greve, 2006):

$$\begin{aligned}
N &= \frac{\frac{1}{v_1}}{\frac{1}{v_2}} \\
\cos(\theta_i) &= -(\bar{n} \cdot \bar{p}) \\
\sin(\theta_t)^2 &= N^2 \cdot (1 - \cos(\theta_i)^2) \\
\cos(\theta_t) &= \sqrt{(1 - \sin(\theta_t)^2)} \\
\bar{t} &= N\bar{p} + (N \cos(\theta_i) - \cos(\theta_t))\bar{n}
\end{aligned}$$

where N is the relative refractive index.

If $\sin(\theta_t)^2$ is greater than 1 the ray has been internally reflected (total internal reflection), in which case we terminate the ray tracing and ignore the ray.

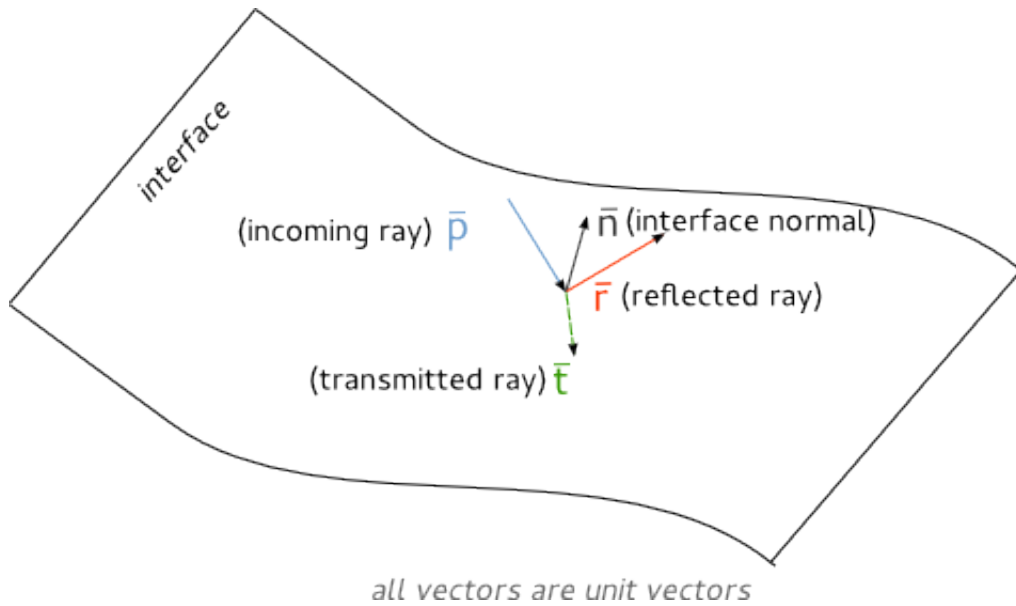


Figure 2.3.2: Reflected and transmitted rays

This allows us to store only the points of intersection, which completely describe the ray path. The distance is the L2 norm of the vectors between the points, and the travel time is the length of each vector multiplied with the slowness of each layer.

Triangle Ray intersection To determine whether a ray intersects a triangle, a MATLAB implementation by Tuszyński (2011) based on an implementation by Möller & Trumbore (1997) is used. The algorithm is fast and does not require the plane equation to be computed or stored.

A ray may be represented as $\mathbf{R}(t) = \bar{\mathbf{s}} + \bar{\mathbf{p}}t$, where $\bar{\mathbf{s}}$ is the source (origin) point and $\bar{\mathbf{p}}$ is the normalized direction vector, t is the distance from $\bar{\mathbf{s}}$. A triangle can be defined by its three vertices $\bar{\mathbf{V}_0}$, $\bar{\mathbf{V}_1}$ and $\bar{\mathbf{V}_2}$.

The transformation $\mathbf{T}(u, v) = (1-u-v)\bar{\mathbf{V}_0} + u\cdot\bar{\mathbf{V}_1} + v\cdot\bar{\mathbf{V}_2}$ translates a point in Barycentric coordinates into a point in the triangle in Cartesian coordinates.

By finding $\mathbf{R}(t) = \mathbf{T}(u, v)$, the intersection point of the ray and triangle is determined.

$$\begin{bmatrix} -\bar{\mathbf{p}} & (\bar{\mathbf{V}_1} - \bar{\mathbf{V}_0}) & (\bar{\mathbf{V}_2} - \bar{\mathbf{V}_0}) \end{bmatrix} \begin{bmatrix} t \\ u \\ v \end{bmatrix} = \bar{\mathbf{s}} - \bar{\mathbf{V}_0} \quad (2.3.1)$$

The linear system from equation 2.3.1 may then be solved to find t , u and v . If $u \geq 0$, $v \geq 0$ and $u + v \leq 1$ the Barycentric coordinates are valid and the ray intersects the triangle. A positive t means the ray intersects in the forward direction.

$$\begin{aligned} M &= [-\bar{p} \quad (\bar{V}_1 - \bar{V}_0) \quad (\bar{V}_2 - \bar{V}_0)] \\ \begin{bmatrix} t \\ u \\ v \end{bmatrix} &= M^{-1}(\bar{s} - \bar{V}_o) \end{aligned}$$

2.3.1.3 Error calculation

By default the origin time is calculated using only the P and S phase, whereas the traveltime differences between all P, S, M and MM phases may be used. M and MM phases are excluded from origin time calculation because a great part of the traveltime is (for near earthquake sources) spent in near vertical travel in the water column. This means that onset angle will be strongly dependant on bathymetry, and not location. The errors in onset and the

total error in differences are weighted equally. The difference error is weighted equally for all phase combinations. The origin time is calculated by equation 2.3.2 for all grid points using:

$$T_{origin} = \frac{\sum_{\phi}^s \sum_{\phi}^{\phi} (T_{s,\phi} - t_{s,\phi}) \times \omega_{origin,\phi}}{\sum_{\phi}^{\phi} \omega_{origin,\phi}} \quad (2.3.2)$$

where $T_{s,\phi}$ is the phase(ϕ) arrival time for the station (s) and $t_{s,\phi}$ is the calculated travel time. The weights for the origin time calculation, $\omega_{origin,\phi}$, are 1 for P and S, otherwise 0. The travelttime difference is calculated for all grid points using equation 2.3.3:

$$\xi_{td} = \sqrt{\frac{\sum_{i=1}^s \sum_{k=i+1}^{N_{\phi}-1} \sum_{\phi}^{N_{\phi}} [(T_{s,\phi_k} - T_{s,\phi_i}) - (t_{s,\phi_k} - t_{s,\phi_i})]^2}{N_{\phi} \times N_s}} \quad (2.3.3)$$

where N_{ϕ} is the number of phases and N_s the number of stations. The origin time error is calculated for every grid cell by equation 2.3.4:

$$\xi_{origin} = \sqrt{\frac{\sum_{\phi}^s \sum_{\phi}^{\phi} [(T_{origin} - (T_{s,\phi} - t_{s,\phi})) \times \omega_{origin,\phi}]^2}{N_s \times \sum_{\phi}^{\phi} \omega_{origin,\phi}}} \quad (2.3.4)$$

The total error is computed by equation 2.3.5:

$$\xi_{total} = \frac{\omega_o \times \xi_{origin} + \omega_{td} \times \xi_{td}}{(\omega_o \times N_s \times \sum_{\phi}^{\phi} \omega_{origin,\phi}) + (\omega_{td} \times N_{\phi} \times N_s)} \quad (2.3.5)$$

where the weights ω_o and ω_{td} are both 1. The grid cell with minimum ξ_{total} is chosen as the solution for hypocenter and origin time.

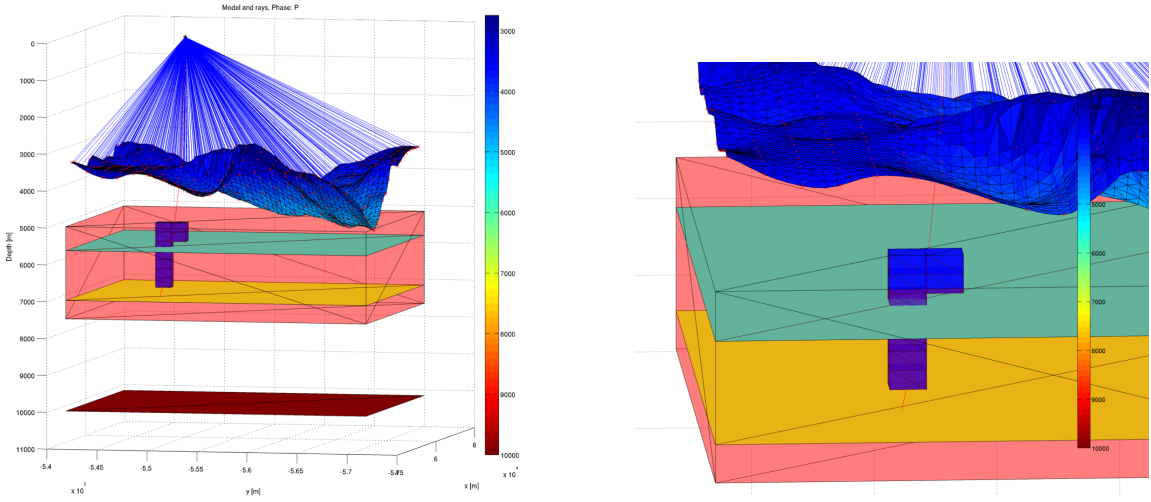


Figure 2.3.3: HYPOSEARCH matching grid cells to traced rays in region of interest. Blue rays are initial rays shot from station (black star at 0 m depth) onto the triangulation of the bathymetry (in blue, from IBCAO). The ray parameter of the refracted ray is determined by the angle of incidence of the incoming ray and the inclination of the matched triangle together with the velocity of the layers on each side of the interface (water layer in the case of the bathymetry). In the model used in this thesis all the interfaces below the bathymetry are horizontal (consisting of two triangles). However, they could be as complicated as the bathymetry, but at the cost of requiring more computation since more triangles need to be matched against rays. The blue boxes represent the grid cells that are matched to the ray (red).

2.3.1.4 Matching to grid cells

The process of matching the rays to the grid cells starts by constructing a box of triangles around the entire region of interest. The rays that have reached the layer in which the region is are checked for whether they intersect the triangles of the box. For each grid cell, a similar rectangular box of triangles is constructed, and all the rays that intersected the region box are checked against the grid cell boxes to determine which grid cells they hit.

Each ray normally hits several boxes. A ray that hits a cell box is considered to have hit the center point of the grid cell, this means that the grid cell size determines the accuracy of the ray tracer.

Figure 2.3.3 shows HYPOSEARCH during ray tracing and matching against grid cells for one phase for one station.

2.3.1.5 Synthetic tests

To verify the HYPOSEARCH routine, theoretical traveltimes should be calculated using an existing solution. By using the TauP package (Crotwell & Owens, 1999) traveltimes for a flat layered model were computed. The TauP package assumes a spherical earth while the interfaces in HYPOSEARCH were specified to be horizontal (although curved interfaces could be specified, in which case the resolution of the triangulation would determine the error from a real sphere). For the purpose of this thesis this difference is ignored, as the tests are done on relatively small models (< 50 km).

For the synthetic test a simple two layered model was used (table 2.1).

| Depth [m] | V_P [m/s] | V_S [m/s] | |
|-----------|-------------|-------------|------------|
| 0 | 1500 | 1500 | (water) |
| 3000 | 5800 | 3200 | (seafloor) |

Table 2.1: Synthetic velocity model

The positions source and stations are given in Cartesian coordinates (table 2.2):

| Station | X (longitude) [km] | Y (latitude) [km] | Distance to source [km] |
|---------------------|--------------------|-------------------|-------------------------|
| Source (5 km depth) | 10 | 10 | 0 |
| GAK2 | 0 | 0 | 14.142 |
| GAK3 | 0 | 5 | 11.180 |
| GAK4 | 5 | 5 | 7.071 |

Table 2.2: Positions for synthetic test

Traveltimes are calculated using TauP (interface specified at 3 km depth), which gives the results shown in table 2.3:

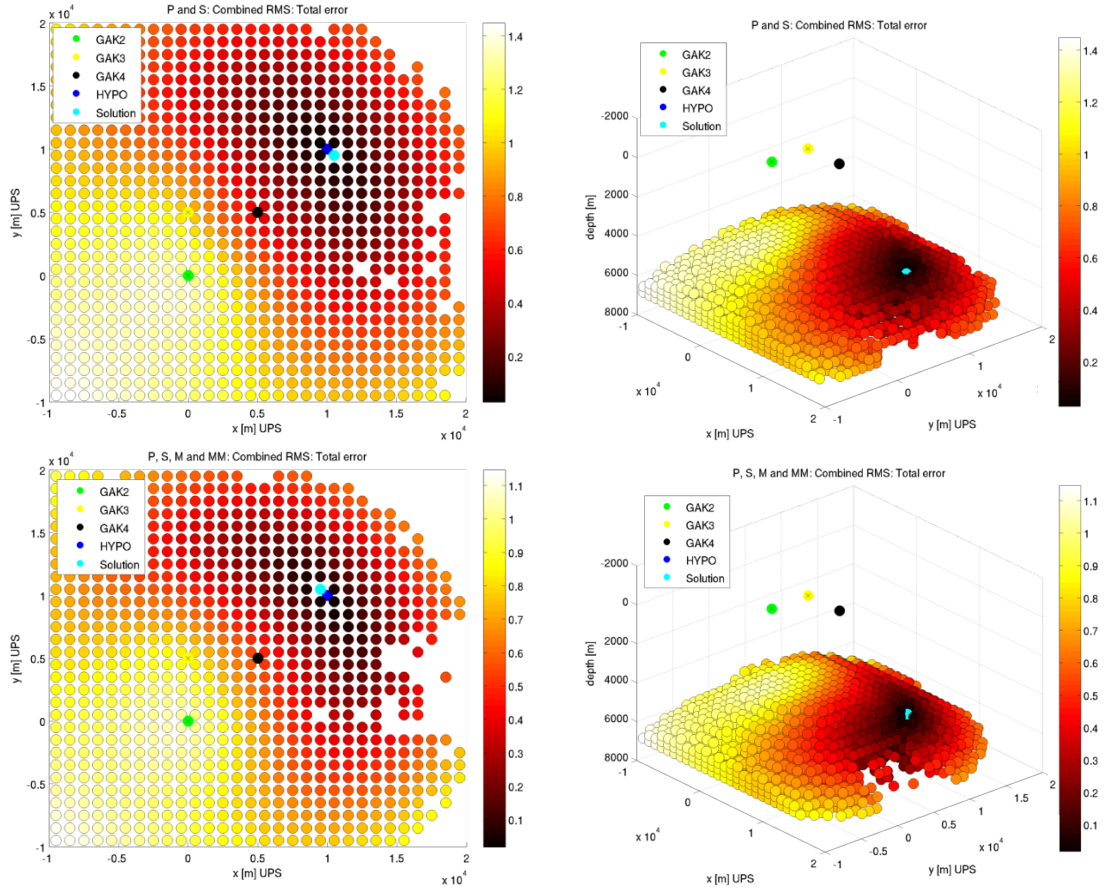


Figure 2.3.4: Error values at grid cells are plotted in increasingly hotter colors. Stations (green, black, yellow) are plotted along with the best match (cyan) and synthetic source (blue). Top plots only consider P and S phases, bottom plots uses P, S, M and MM for travel time differences.

| Station | Phase | | | |
|-------------|-----------------|------|-----------|-----------------|
| | p | s3p | p^0Pv3p | p^0Pv3p^0Pv3p |
| | P | SP | M | MM |
| | Travel time [s] | | | |
| Origin time | | | 0 | |
| GAK2 | 4.39 | 6.23 | 8.26 | 12.13 |
| GAK3 | 3.89 | 5.32 | 7.76 | 11.63 |
| GAK4 | 3.20 | 4.08 | 7.08 | 10.97 |

Table 2.3: Synthetic traveltimes calculated by TauP

These traveltimes were used as input for the HYPOSEARCH routine which calculated the traveltimes and RMS value at each grid point (as shown in figure 2.3.4). The best solution was then verified to match the synthetic source used for the synthetic travel time generation.

| Station | Phase | | | |
|------------------------------|-----------------|-------|-------|-------|
| | P | S | M | MM |
| | Travel time [s] | | | |
| HYPOSEARCH origin time | -0.025 | | | |
| HYPOSEARCH RMS | 0.011 | | | |
| GAK2 | 4.41 | 6.26 | 8.28 | 12.15 |
| Residual to TauP travel time | 0.02 | 0.03 | 0.02 | 0.02 |
| GAK3 | 3.87 | 5.29 | 7.72 | 11.61 |
| Residual to TauP travel time | -0.02 | -0.03 | -0.04 | -0.02 |
| GAK4 | 3.23 | 4.14 | 7.12 | 11.01 |
| Residual to TauP travel time | 0.03 | 0.06 | 0.04 | 0.04 |

Table 2.4: Traveltimes for best solution calculated by HYPOSEARCH

The source time was set to be 0 s (or 1970-01-01 00:00 UNIX time). Table 2.4 shows the calculated traveltimes for the best solution found by HYPOSEARCH. Given that ray paths are selected as soon as they intersect the boundaries of a grid cell, there will always be some numerical errors introduced by the coarseness of the grid.

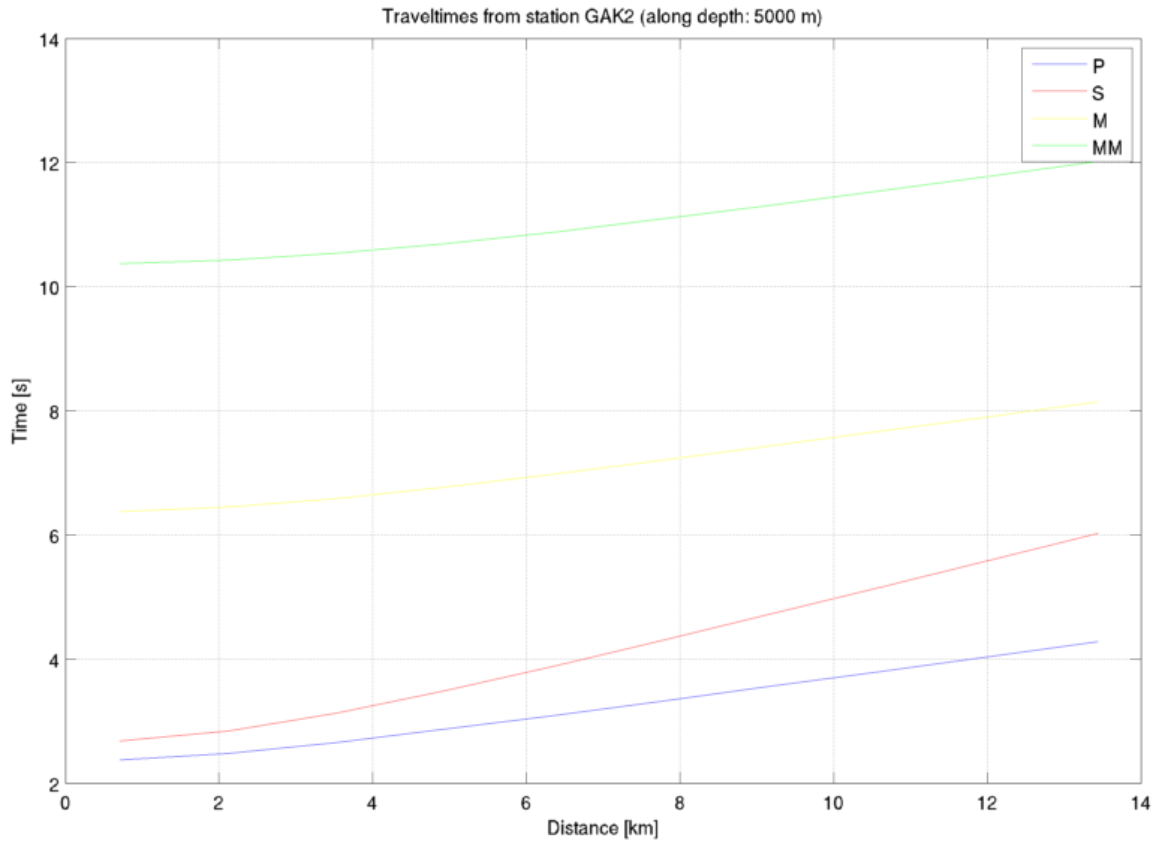


Figure 2.3.5: Traveltimes plotted for distance between station GAK2 and synthetic source (at depth 5 km).

Traveltime as a function of distance, calculated by HYPOSEARCH, is shown in figure 2.3.5. When the multiples (phases M and MM) can be traced and solved as seen in figure 2.3.4, they will aid in constraining the epicenter as the RMS error will grow faster with more constraints. However they do not aid significantly in constraining the depth of the source.

Figures 2.3.6 and 2.3.7 show the lack of dependence on depth for traveltimes and travel time differences for 2.8 km and 14 km distance respectively.

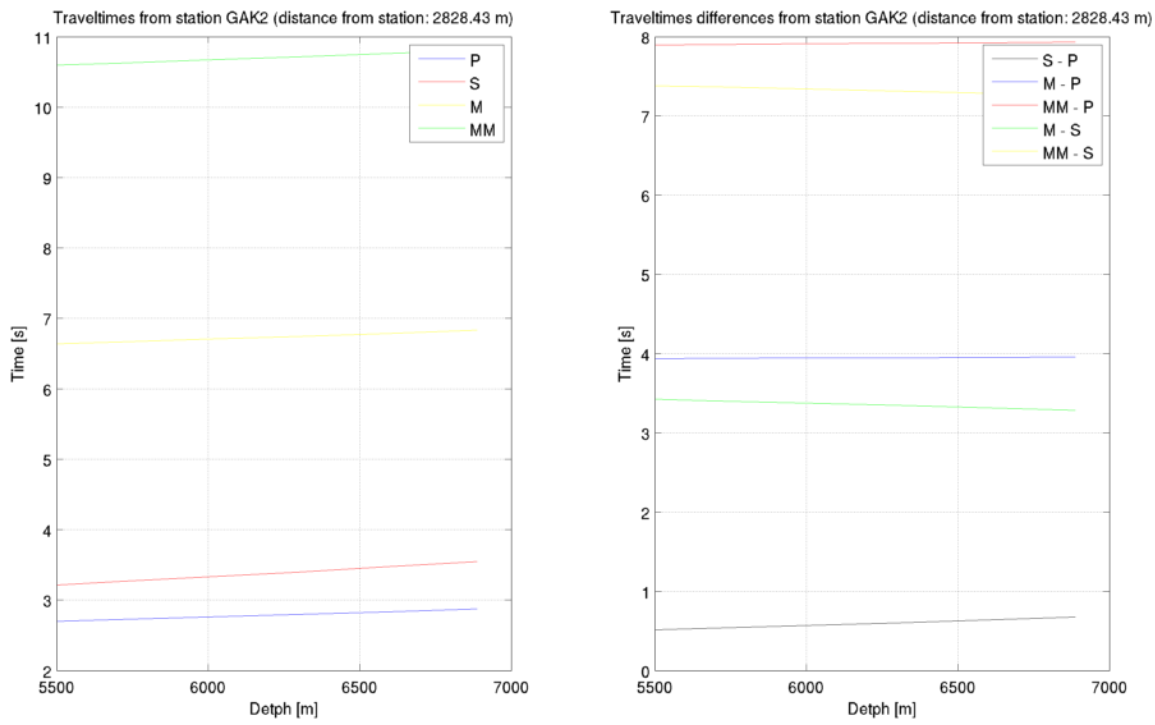


Figure 2.3.6: Traveltimes and differences plotted as function of depth at a distance of 2.8 km.

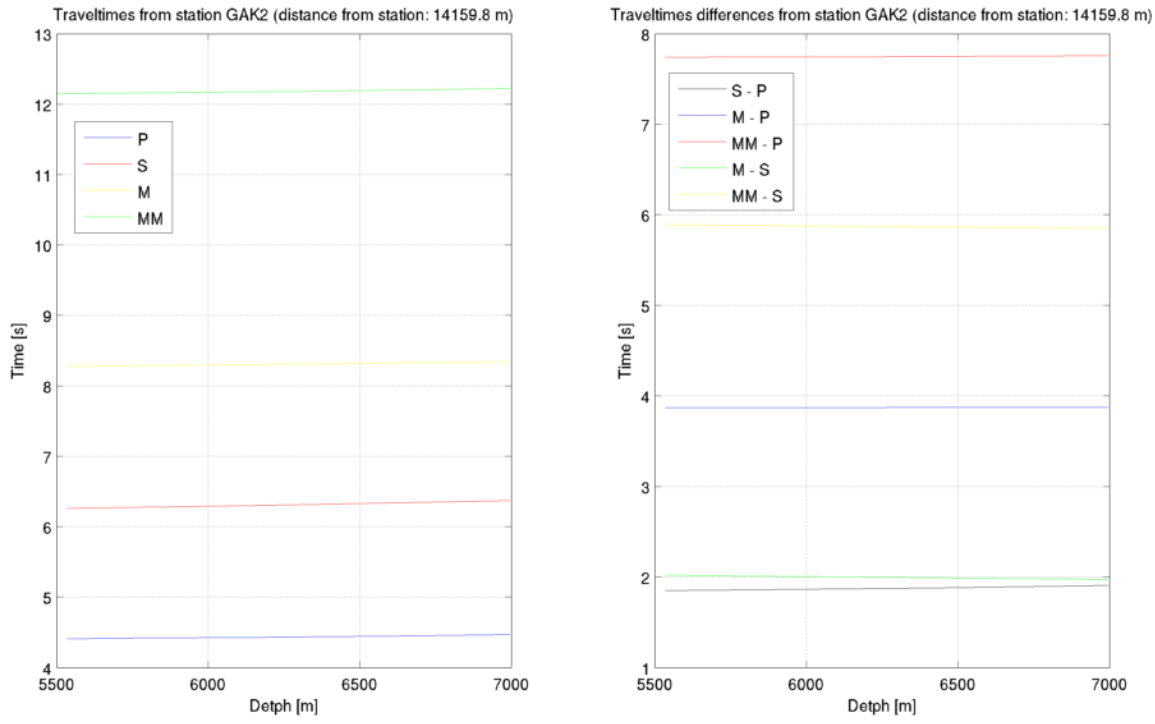


Figure 2.3.7: Traveltimes and differences plotted as function of depth at a distance of 14 km.

The tests show that in order to get a good depth constraint the network must be (almost) above the source. Moreover, since the bathymetry is highly variable it is important to take this bathymetry explicitly into account.

Chapter 3

The Seismic Station and Survey Outline

3.1 Microearthquake studies in an ice-covered ocean

The sea ice above the Gakkel Ridge is continuously moving because of the tide, wind and ocean currents. The general drift direction is due south and through the Fram strait. The changing and unpredictable weather strongly influence the drift, and the wind can easily blow the ice northward against the general drift or accelerate it southward, constantly affecting the position of the stations and causing minor changes in network geometry.

The ice at these latitudes, around $85^{\circ}N$, is mostly continuous (although September 2012 saw a record low in the Arctic sea ice extent (Parkinson & Comiso, 2013)). However, the variable size ice floes drift apart and are pressed together depending on the external forces. Even though the geometrical configuration of the ice floes is not constant, there is very little rotation of the individual ice floes.

If a suitable multi-year (and strong) ice floe a few kilometer in diameter can be found, a fairly stable network geometry can be achieved. However, finding suitable ice floes might take too much time, but it was relatively easy to find large areas of adjacent, wide and level, ice floes with few open fissures.

Having individual positioning on the stations removes this restriction, and it was not neces-

sary to deploy the network on a single ice floe, so it was possible to achieve a larger aperture and more ideal network geometry.

Läderach & Schlindwein (2011) required a single large ice floe since only the position of the center station in their array could be retrieved.

The risk of the ice floes drifting somewhat apart is still present, so being able to receive status and position information from the stations is important to secure recovery.

In this experiment the hovercraft stayed near the network, and the stations could therefore be maintained and recovered more easily.

3.2 Outline of the survey

The experiment was performed in July to September 2012 by deploying a small network of five buoys upstream of the Gakkel rift valley. Each buoy tracked position and timing independently, through an accurate GPS receiver, and stored the continuously acquired signals, from a hydrophone that was let through the ice, locally. The buoys were connected in a wireless network for real time communication, transmission of status and positioning, and, when signal strength permitted it, data was transferred back to the logging central at the hovercraft in real time (Figure 3.2.1).

The digitizer and control part at each station were lightweight (less than 1 kg) and operated for more than 14 days on a single 72 Ah car battery. To set up a station, a hole was drilled in the ice (ice thickness was normally about 2 m). The buoy and antenna (for wireless communication) were anchored with a piece of wood to the ice. Recording started immediately upon connecting the buoy to the battery.

To be able to verify the performance of the buoys, a seismometer (Nanometrics Trillium 120) and a standard digitizer (Nanometrics Taurus) were co-located with one of the stations. In addition to signal comparison with the buoys, the horizontal components would aid in discriminating between cryogenic and seismic signals. Since the first priority of the experiment was to set up the buoys in the network, the preparations and setup of the seismometer were simpler than in the experiments of Läderach & Schlindwein (2011). To mitigate the simpler setup and to prevent failures the seismometer was re-balanced two times a day.

A regular laptop with a radio unit along with an antenna mounted on the hovercraft constituted the central logging station. After deploying a station, the incoming data was checked to ascertain that the buoy was functioning and that the signal from the hydrophone was reasonable. There was, however, no time for long or comprehensive checks.

Before and during the first deployment, it became evident that two of the five stations had unfixable failures either in recording from the hydrophone or in excessive power usage. Thus the first deployment consisted of four stations and one seismometer, while the second and third deployments had three stations and one seismometer.

Around 15 minutes were required to deploy a single station, and it took around 5 hours deploying the entire triangular network with side lengths of ca 5.5 km. Due to the risk of changing weather conditions, continuous southward drift and marginal hovercraft fuel reserves, set-up of the network was limited to as short time as possible. This was to ensure that the entire network was operational and ready before it drifted into the rift valley.

After the network was deployed on the northern flank of the rift valley, the direction of drift was generally southward, modulated by the force of winds and ocean currents. When the network had drifted past the southern flank, the deployment ended and the stations were recovered. The data was subsequently downloaded from the local storage, the batteries were charged and the buoys were checked. The buoys were ready for re-deployment the same day.

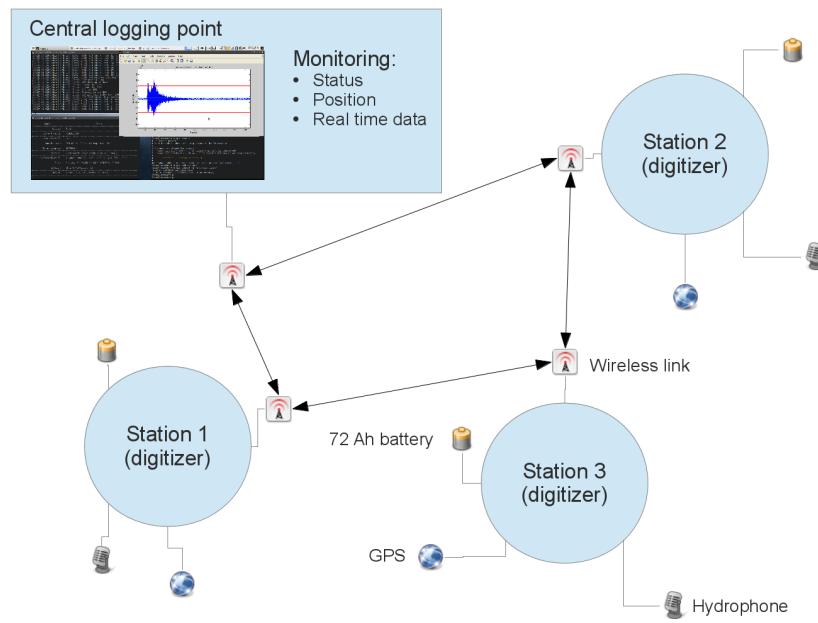


Figure 3.2.1: Overview of network setup

3.3 Instrumentation

This section describes the design and build-up of the buoys (Figure 3.3.1).

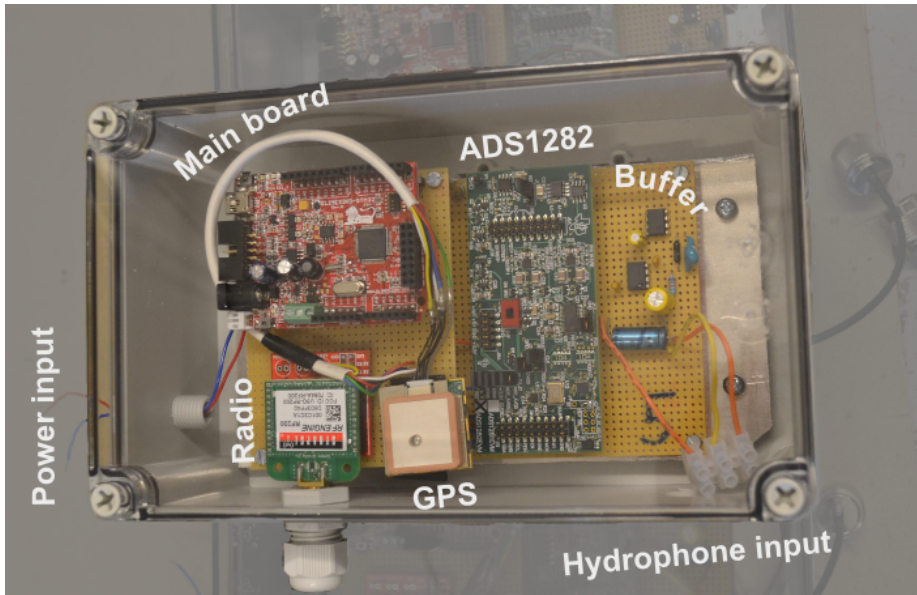


Figure 3.3.1: Buoy interior with components. Power regulators are located below the top layer (left). On the left top layer: main board, radio and GPS. On the right lower layer: the AD converter along with buffer and hydrophone decoupling.

Each buoy was powered by a 12 V 72 Ah car battery. The internal regulator accepted power between 9 V - 36 V so that even though the battery was almost discharged the buoy would still function.

Internally the voltage was regulated into several different levels, powering the digital parts with power efficient switching regulators, and the analog, noise sensitive parts, by low-dropout regulators (LDO). The latter provided very low noise regulated current, but at a somewhat lower efficiency. The circuit layout is shown in figure A.2.1 in appendix A.2.

The casing was specified to IP67 and is waterproof to below one meter. Cable throughputs potentially make it less waterproof, but care was taken to keep them watertight.

The main board, an *Olimexino STM-32 H103* (Olmexino Ltd., 2011), contains the operating system (OS). The main board is based on an ARM7 CPU, STM32F103RBT6 (STMicroelectronics, 2012), running at 72 MHz with only 20 kB of RAM and 168 kB of FLASH ROM for storing the operating system. The board is power efficient and industrial standard.

Through careful programming and extensive usage of interrupt driven programming (in

order to achieve multi-threaded behavior) the complete operating system (OS) could be loaded into the available FLASH ROM. The OS handles input from the AD converter and GPS unit, drives the network protocol interfaced with the radio unit, and stores the samples on the SD card (with a FAT32 file system using the file format specified in appendix B). The data throughput from hydrophone to storage had to be completed quickly since very little data could be stored in RAM and at the same time allow the rest of the OS to be driven. The operating system was written in C++ and was based on the Maple low-level library for ARM platforms (libmaple, (LeafLabs, 2012)). Figure 3.3.2 shows a diagram of the operating system hierarchy.

The radio unit was a Synapse RF200 (Synapse Wireless, 2011) which runs on regular wireless frequencies, 2.4 GHz. A similar unit was connected to the central logging computer. The RF200 supports a built-in mesh network which allows communication to follow any path between the network nodes from transmitter to receiver, and thus achieves a longer range (multi hop) and a more stable network.

The radio units were programmed in a Python like language. However, the main protocol was built into the operating system described above. Some logic was nevertheless programmed into the radio unit, which allowed network transmission speed to be adjusted, nodes to be addressed and activated, and the RF200 nodes to be remotely instructed to hard-reset the main board in case of a lock up.

The network was specified to have a maximum range of 4.8 km. To further extend the range, antennas with 15 dB(isotropic) amplification were applied as well as the use of a 1 W amplifier at the logging station (power limitations at the stations prevented the use of amplifiers on them).

For positioning and timing a GPS, *EM-406A* based on *SiRF III* (GlobalSat, 2012), was used. It provided a pulse-per-second (PPS) signal accurate to $1 \mu s$. This allowed independent timing and positioning to be acquired on all buoys. A position was provided each second and time was calibrated at each PPS and referenced to the samples as they were recorded.

The samples were stored on a SD card (hardware socket available on the *Olimexino STM-32 H103*). The samples were organized in batches of 1024 samples and each batch was referenced with a timestamp so that the recorded traces have a reference approximately every 4 seconds. The AD sampled the hydrophone output level at 250 Hz. A file format was

designed so that the samples could easily be written as they were recorded requiring a minimal of on-board processing. The central logging station used a text based file format to store the data received over the wireless network. Section B describes the formats in detail.

The drivers for the component were implemented in the operating system using an object-oriented approach with one class for each component. A main class set up the other classes and ran the main loop which executed the iterations of the components at each main loop iteration. Sampling and GPS timing were interrupt driven and the routines were run almost instantly when a new sample was ready or when a new GPS time was ready. The other less time critical tasks were run at each main loop, so that the data queue was stored on the SD card and emptied, radio communication was handled or a new position was calculated.

The critical tasks (e.g. checking whether the sample queue was full) were also run while routines that could take some time (e.g. transferring a batch of samples over the wireless network) to make sure that they were not delayed too long. A CPU watchdog was set up so that if a lock-up occurred, the buoy would be reset and re-initialized along with all the components. The routines were coded so that they to the largest possible degree did not block on any operations, so that the sample rate and timing could be maintained.

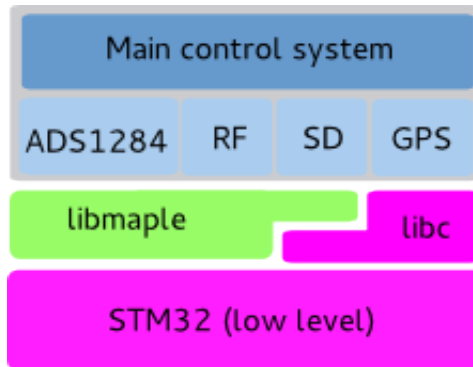


Figure 3.3.2: Diagram of operating system hierarchy. Components (control and drivers) (except SD card with FAT filesystem) inside gray box have been developed as part of this project. Minor modifications were made to the libmaple library and the SD/FAT library.

3.3.1 Analog to digital interface

An *ADS1282-EVM* (Texas Instruments, 2009) with a built-in *ADS1282* (Texas Instruments, 2007) was used as analog to digital converter. It is a sigma-delta AD converter configured (by the main board) to filter the signal between 20 seconds periods and 250 Hz. Sample rate is set to 250 Hz and the theoretical maximum dynamic range was specified to be 130 dB¹ at this frequency. The suggested decoupling for the hydrophone (Teledyne Benthos, 2012a) was extended with a buffer and decoupling (high-pass) stage interfaced to the input terminals of the AD converter. The extension added an additional analog low-pass filter (capacitor) and an operational amplifier which provided a buffer at the interface, so that the hydrophone was connected to a high-impedance terminal, which drove the AD input terminals.

There were several stages of analog anti-alias filtering before the signal reached the modulator of the sigma-delta digitizer. The modulator had an input clock frequency of 4.096 MHz and an output sample rate of 1.024 MHz. At the Nyquist frequency of the modulator, $f_{Nq} = 512 \text{ kHz}$, the attenuation of the analog filters is -72.48 dB . The AD converter had internal digital filters (FIR and sinc) which provided more than 140 dB of attenuation (Texas Instruments, 2007) above the Nyquist frequency of the output sample rate ($250 \text{ Hz} \mapsto 125 \text{ Hz}$). There may be some noise originating from the frequencies above f_{Nq} , however because of the sigma-delta design, and assuming the noise has a flat spectra, the total energy of this noise will be divided on all the frequencies up to the input f_{Nq} and only a fraction of it will be in the pass band of the digital filters up to the output Nyquist sample rate, 125 Hz. The largest concern was periodic electrical noise, which do not have a flat frequency response. For future experiments the AD converter may be configured to output samples at frequencies as high as 4000 Hz, though testing will be required to determine whether the main board and operating system can handle the throughput.

$$H_a = \frac{8.2698 \times 10^{15}s}{(s + 9.551 \times 10^5) \times (s + 1.667 \times 10^5) \times (s + 1.247 \times 10^5) \times (s + 0.2128)} \quad (3.3.1)$$

Figure 3.3.3 shows the frequency response of the analog interface, the transfer function is

¹Table 1, p. 13, Texas Instruments (2007)

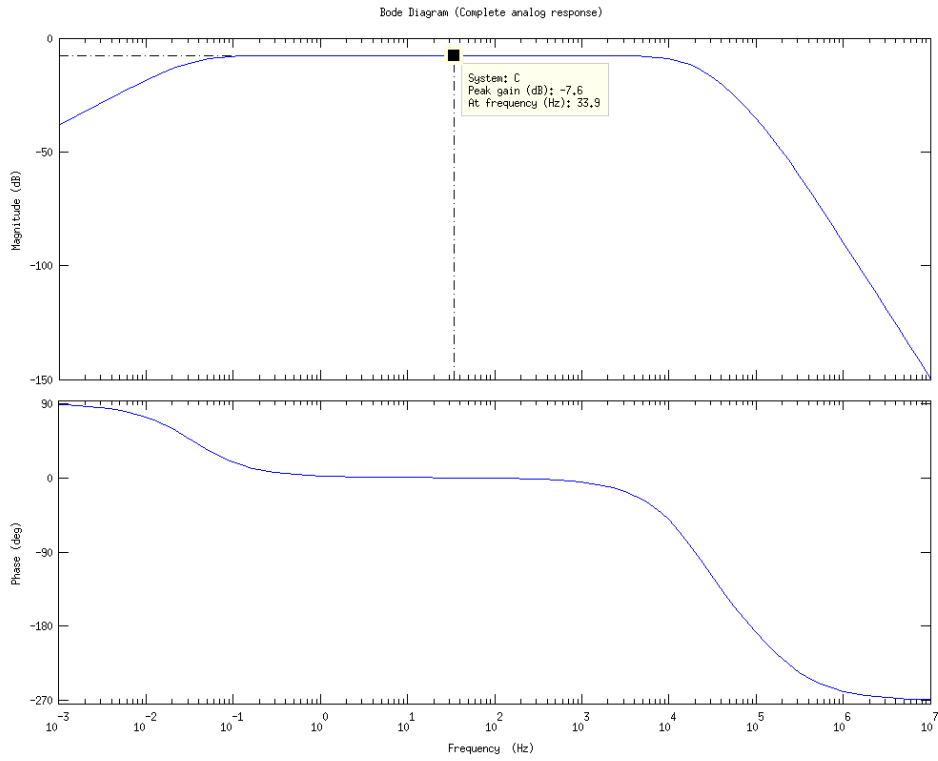


Figure 3.3.3: Frequency response of complete analog system, equation A.2.9.

given by equation 3.3.1.

A Benthos AQ-18 hydrophone was chosen (Teledyne Benthos, 2012a,b). It was specified to have a flat response between 1 Hz - 10 kHz. For this frequency band the output of the hydrophone is related to hydroacoustic pressure by the equation 3.3.2:

$$H_{Hyd} = -171 \text{ dBv re } 1 \text{ uPa} = 10^{8.55} \frac{\text{V}}{\text{uPa}} \quad (3.3.2)$$

Temperatures during the experiment varied around 0° C, and some characteristics of the analog and digital system may be affected by the slightly lower than normal temperatures. When possible, components specified to industrial standard (-40° C to 80° C) were chosen.

More details and derivation of the transfer function can be found specified in appendix A.2. The decoupling stage, part of the transfer function (equation 3.3.1), scales the output from the hydrophone from $\pm 6 V$ to $\pm 2.5 V$ which was the configured range of the AD converter. The output of this range was a 32 bit signed integer which maps to the range $\langle -2^{31}, 2^{31} - 1 \rangle$ counts.

3.3.2 The Station

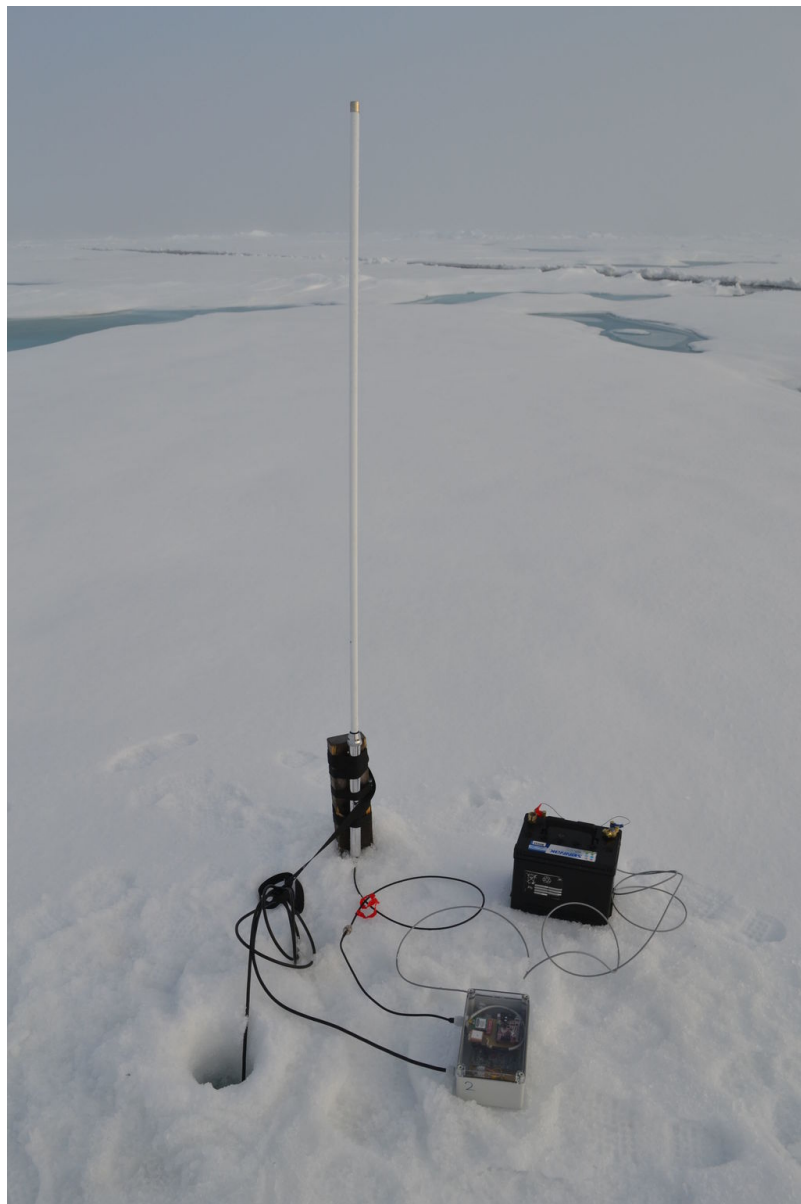


Figure 3.3.4: The buoy connected to the hydrophone let through a hole in the ice with antenna mounted and the battery connected. The hydrophone cable in this picture is not yet covered in snow to avoid noise from wind.

Figure 3.3.4 shows the setup of a station on the ice. The hydrophone was lowered just below the ice since a periodic signal could be observed when the cable was extended longer, possibly originating from strumming caused by ice drift and ocean current. With the hydrophone just below the ice or just inside it this periodic signal completely disappeared.

3.3.3 Seismometer

A Nanometrics Trillium seismometer was placed inside a Zarges box (to protect it from wind and weather) together with a Nanometrics Taurus digitizer. It was either powered from the same battery as the buoy it was located next to, or when possible, separately. This setup was monitored manually and batteries could be replaced when needed since the hovercraft was located at this station during drift.

The digitizer was configured in a similar way as Läderach & Schlindwein (2011) had done. When the sensor output drifted, either from ice movement or tilt, and approached maximum it was reset. If the seismometer was tilted the resetting would have little effect on the horizontal component since the seismometer mass would not be able to center, but failures due to ice movement could be prevented. The vertical component is the most reliable, although it as well was affected by tilt and drift.

Chapter 4

The Field Experiment and Data Acquisition

The plan for the *FRAM-2012* expedition was to leave Longyearbyen 16th of July 2012 with the hovercraft *Sabvabaa* for the earthquake survey of the Gakkel Ridge two weeks ahead of the accompanying icebreaker *Oden*. Upon *Oden*'s arrival at the Gakkel Ridge, the hovercraft would terminate monitoring of the seismicity, be refuelled and the two vessels would move on to the main geological work area on the Lomonosov Ridge. The hovercraft was loaded on board an ice-strengthened freighter in Longyearbyen and transported to the ice edge at $80^{\circ}52'N$, $15^{\circ}E$, put on the water in the morning of 18th of July and fueled. The hovercraft arrived at $84^{\circ}39'N$, $12^{\circ}E$, about 30 nautical miles from the target area, on 27th of July when progress halted due to difficult ice and alternator failure. Consequently the hovercraft was grounded until spare parts could be brought in by air and *Oden* arrived on August 3rd. The plan was now to follow *Oden* and defer the earthquake monitoring. However, the hovercraft was not able to keep up with the icebreaker due to periods of poor visibility and areas of difficult ice. The decision was made to abort and concentrate on the Gakkel Ridge objective for the next five and a half weeks until the icebreaker returned south.

The first deployment over the rift valley was completed on the 9th of August and a total of three deployments gave 23 days of array recording time. Of the initial five stations, three in addition to the seismometer were functional during the entire experiment. The last 7 day long deployment was the most successful with all systems operational. In this thesis,

the analysis will focus on the last data set.

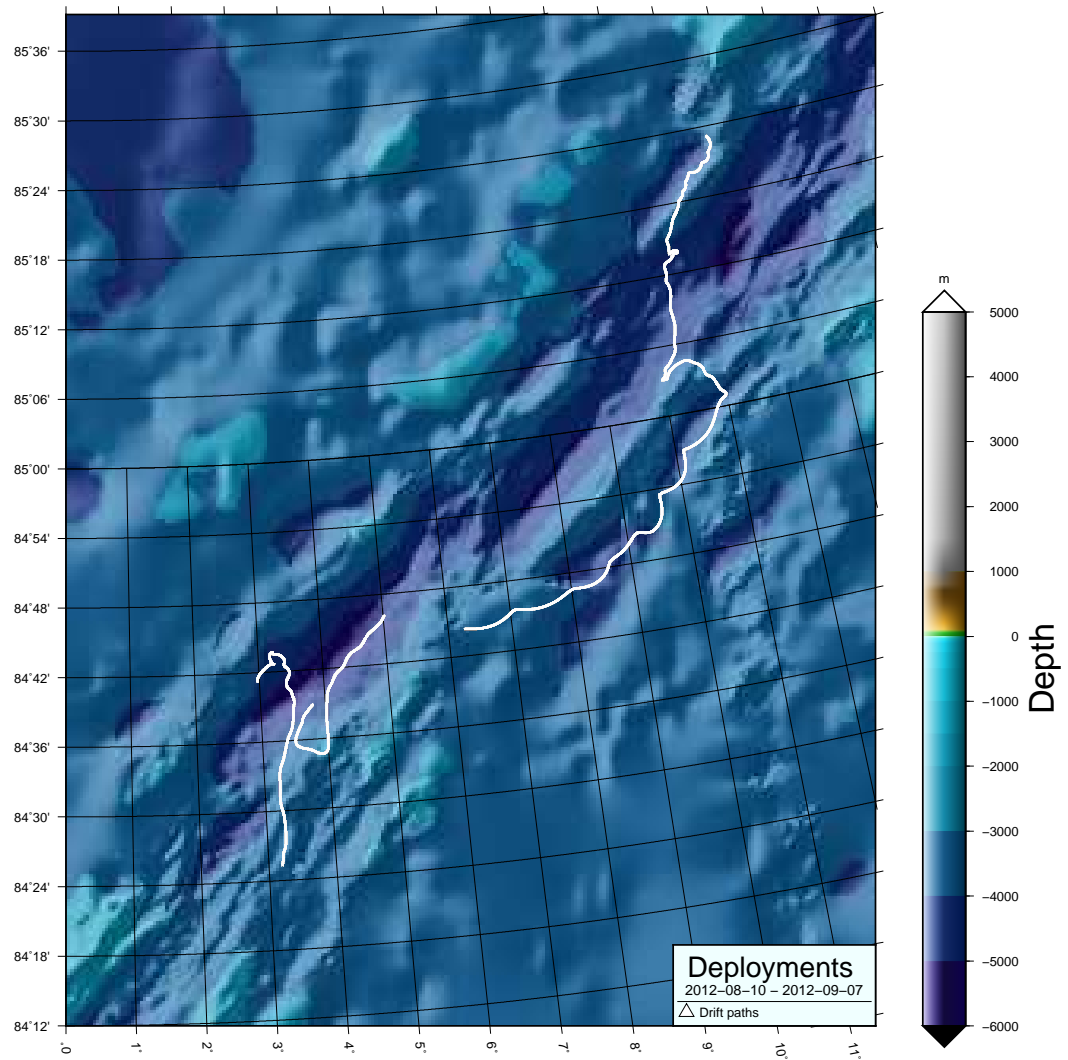


Figure 4.0.1: Drift track for all deployments, starting with the first drift in the east and progressing with westward component of the general ice drift.

4.1 Drift G1

The first drift lasted from 2012-08-10 to 2012-08-23 (figure 4.1.1). Four stations were deployed as well as one seismometer.

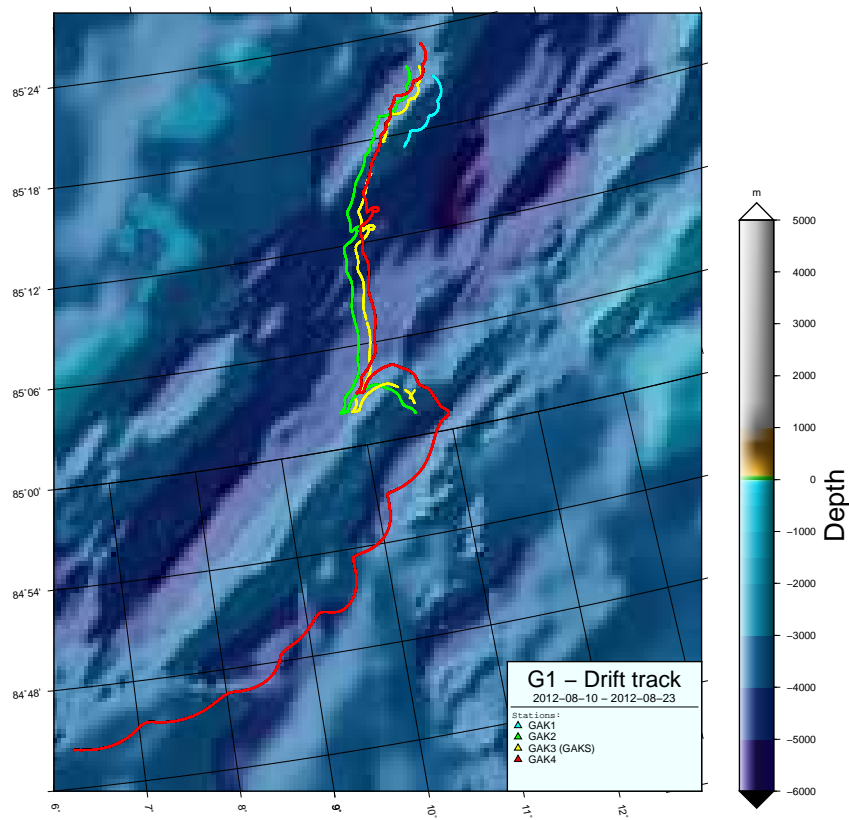


Figure 4.1.1: Drift path during G1. The path of station GAK1 quickly stopped as it had powered down. It was not picked up before the others. It can be seen that station GAK3 (located next to *RH Sabvabaa*) sporadically loses the GPS fix and the affected sections of the path is missing.

The stations were placed in a triangle with one station in the middle (approximately 2.5 km radius from the middle station) together with the seismometer and the hovercraft. Two of the corner stations had problems recording, however it was possible to fix one (station GAK4) after the deployment. The other station (GAK1) seemed to have a short-circuit which drained the battery, and could not be fixed. Although some of the recorded data appears to be valid the buoy quickly powered down and the data was not considered trustworthy. Contact over the wireless network was achieved with station GAK4 during the drift and it became evident that although the timing and positioning were functional, the signal was flat except for electronic noise.

Station GAK5 was not able to record from the hydrophone, this could not be fixed with the available tools and it was never deployed.

During this deployment the station next to the hovercraft recorded a periodic signal that could last for hours. If the hydrophone was removed from the water the signal disappeared. By positioning the hydrophone just below the ice or slightly inside the ice, the problematic signal disappeared. The noise may therefore be related to strumming or turbulence below the ice.

Several strong seismic events were recorded, and roughly 10 smaller events a day. Because of the few working stations it will not be possible to locate the events.

Bad weather during pickup delayed retrieving of the last station for several days which resulted in it being the longest running station which operated for 15 days. Voltage levels were still good at the time of recovery. Although this station was not working optimally during drift, it was running for more than 14 days as was the design goal for the buoy. The last station was picked up 88 km from the deployment point.

It was discovered that the GPS had problems achieving a good enough signal, this resulted in inaccurate timing and a less accurate position. No solution could be found before the next deployment and so that the two first deployments were affected. Before re-deploying, the operating system was upgraded and the storage routines were optimized. They had in the previous version in some rare cases resulted in the data throughput not being handled fast enough and that some samples were lost.

To recover the stations, the drift vector of the hovercraft was added to the deployment position, correcting slightly for the expected drift during deployment (drift was usually

around 0.1-0.2 knots). Even though bad weather (and strong drift due to wind) interrupted the recovery by several days, the movements and drift could be correctly summed up and used to determine the new position of the last station, where it was picked up more than 80 km away.



Figure 4.1.2: Field experiment, from top left, clockwise: the *RH Sabvabaa* approaching a deployed buoy; melting hydrophone out of ice using hot water to avoid damage; buoy melted into ice and covered by fresh snow (we observed the red indicator light on the GPS blinking to signify full position and timing fix); computer acting as central logging point in the cabin of *RH Sabvabaa*.

4.2 Drift G2

The second drift session is shown in figure 4.2.1 and lasted from 2012-08-24 to 2012-08-29. Station GAK4 could be repaired, and together with station GAK2, GAK3 and the seismometer (next to station GAK4) it was deployed in a triangle. As with the first drift, the GPSs of the stations were only able to gain a full position and time fix sporadically.

Station GAK3 lost the position completely during most of the drift. However, the relative time could be usable and the position is fairly accurate, so that it in some cases may be used for locating events. The position of station GAK3 can be calculated, as Läderach & Schlindwein (2011) have done for their array, by assuming a constant network geometry.

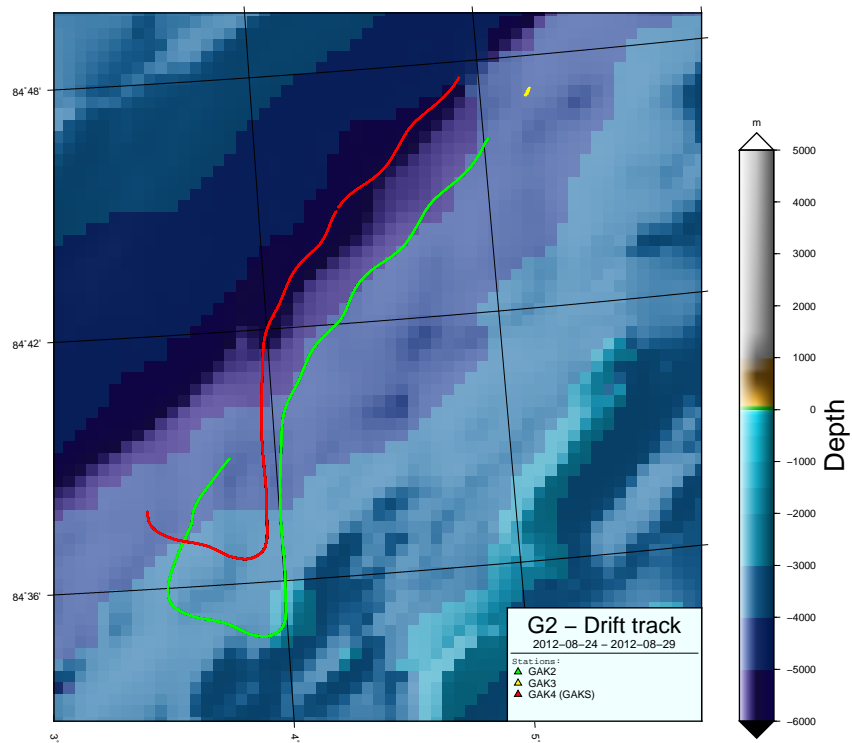


Figure 4.2.1: Drift path during G2. The GPS problems resulted in no path for station GAK3 (yellow).

4.3 Drift G3

The last drift session lasted from *2012-09-01* to *2012-09-07*. Figure 4.3.1 shows the path.

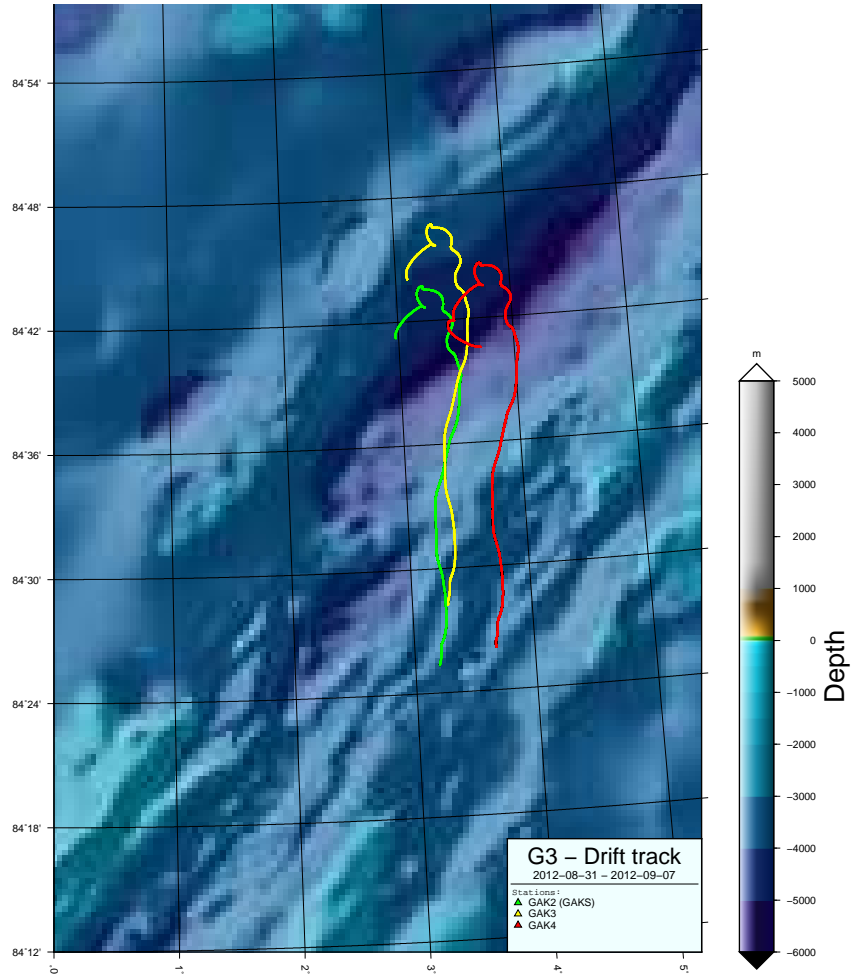


Figure 4.3.1: Drift path during G3

Extensive testing and debugging of the GPS units of the buoys revealed that it was a hardware problem with the GPS and not a software issue in the buoy that caused the lack of a sure position and timing fix. Eventually by the time of the third deployment the source of the GPS problems was discovered: interference from the radio unit had resulted

in the GPS being unable to gain a fix (they are both in a similar GHz spectrum). By moving the GPS receiver inside the digitizer slightly (< 15 cm, Figure 4.3.2) the issues were resolved. The GPS had previously been mounted directly above the RF unit, but was already originally connected to the digitizer with a longer cable to allow it to be fixed to the box, which allowed it to be moved easily. As a result this last drift had good timing and positioning throughout the entire run.

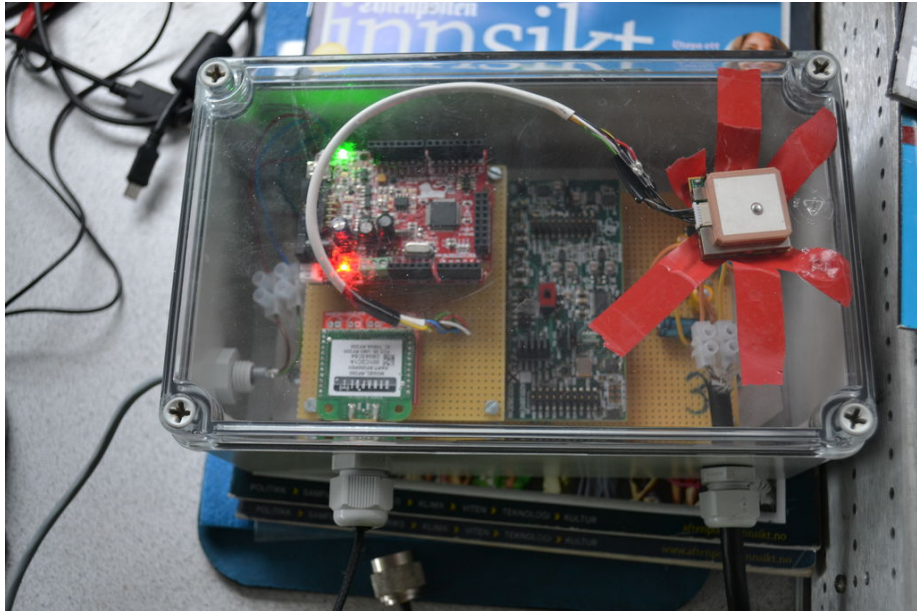


Figure 4.3.2: Relocating the GPS device within the box was sufficient to mitigate GPS problems.

Flags were mounted at each station so that they could more easily be spotted during recovery. In this final deployment the network had the largest aperture with 5.5 km side lengths.

4.4 Technical observations

During the deployments all stations which functioned properly (except for the GPS failures) showed that the battery provided (72 Ah) was sufficient for deployments of more than 10 days. Station GAK4 had an uptime of more than 14 days during the first deployment,

however, it must be taken into account that it during this drift was not working optimally. During the third drift the battery levels were generally less than 1 V lower when collected (after 7 days).

When possible the seismometer and its digitizer were powered by a separate battery, since the battery had to be replaced every 3-4 days (they could not be powered by a voltage level of lower than 11.7 V, which is higher than the usually specified voltage levels of around 10.5 V for a completely discharged battery). The buoys worked with voltage levels as low as 9.81 V.

The voltage drop of a battery is non-linear, but there was an average drop of 0.187 V / day. Assuming that for a healthy 70 Ah battery the maximum and minimum voltages are 12.7 V and 10.5 V, the apparent daily usage corresponds to approximately 5.94 Ah. This is reasonable compared to the calculated daily usage (5 Ah) in table A.1 in appendix A.2. It should be noted that the real capacity of the battery is only as high as specified under optimal conditions. A real capacity lower than what is specified would result in an apparently higher usage.

To deploy the seismometer, the upper layer of snow was first removed and the underlying harder ice was flattened before placing the Zarges box directly on the ice with the seismometer and digitizer inside the box. During the first days, depending on temperature, the seismometer had to be re-balanced (using the water level on the sensor) two times each day before it stabilized.

The failures of two of the stations could have resulted from a loosened solder point during transportation or possibly a burnt component. Determining and repairing the error proved difficult during the experiment. However, other minor failures could be fixed, and some parts of the failed buoys were used as spares for the healthy buoys. There are more than 100 solder points at each buoy and to achieve a more robust solution the circuit should be laid out on a PCB (Printed Circuit Board) with machine soldered and assembled parts.

Sufficient wireless range could not be achieved for sending position, status and data from the far stations. In some cases there was sporadic contact over a distance as far as 2.5 km, where the position and status of the buoys were transmitted. The horizontal flat beam radiation pattern of the omni-directional antenna makes range sensitive to vertical antenna orientation. It was difficult to mount it sufficiently accurate with the current setup.

Together with a higher antenna and a way to easily align the antenna a better range should be possible. A lower frequency (currently 2.4 GHz) could also improve range as it would be less attenuated.

The closest station (next to *RH Sabvabaa*) could transmit the recorded data in real-time and we could monitor events as they were recorded. The network protocol worked very well on the short range. By calculating the position of the buoys from our own drift we were able to recover the stations without problems.

After resolving the GPS problems for the third deployment the buoys logged accurate timing and position. No humidity could be seen on any of the deployments during the total of 23 days.

A small spike was sometimes present on the recorded signal, it was very short (1/10 second) and was possibly related to writing the data to the SD card. It was characteristic and easy to identify during analysis. Under heavy load, while writing to the SD card or transferring the data over the network, the data was in some cases not written fast enough to the SD card. The extensive use of checksums makes identifying these problematic portions of the samples easy. Only the first batch (1024 samples) at the beginning of each data file (40960 samples) were potentially affected. These software bugs were solved by the last deployment.

Deployment and pickup of each station could be done quickly, and by marking the stations with flags they could relatively easily be found and recovered despite the lack of position information.

Chapter 5

Data Analysis

The processing and interpretation focus on the data from the third and last deployment, G3. This drift had the best timing and positioning and the largest aperture. 41 events recorded during the 7 days of deployment have initially been sorted out as strong and clear enough to warrant attempts to locate them. Finally three events have been located.

5.1 Preparation and organization of recorded data

The recorded data from the buoys were loaded from the SD cards to a regular computer. To be able to use existing tools to organize and analyze the field data it was converted to the standard miniSEED format.

The *libmseed* C-library (Trabant, 2012) was interfaced with MATLAB and any pre-processing could be done there first. Some timing failures (from temporary loss of GPS fix) could cause timing jumps. As the GPS drifts and no synchronization pulse is available, the GPS in some cases provided invalid times and positions which had to be removed.

To a large degree these timing errors could be automatically fixed by discarding the invalid or problematic time references and interpolate new references from the previous and following good references. However, some manual revision was necessary.

Most of the the timing errors were only present for short periods and by extracting only the relevant datafiles for an event, the final traces without timing errors were acquired.

Hourly miniSEED files were created for all stations. SEISAN (Ottemöller *et al.*, 2011) was used to create a database with the hourly files and to plot and analyze the combined traces. Each miniSEED file is accompanied by a reference file which contains the additional positioning and status information of the original data. A file which maps the id of the original data files to each hourly file is also saved. This makes automated manipulation of the database simpler.

The data was then scanned manually by going through each hourly file, zooming in on 20 minute segments and apply a set of predefined frequency filters (1 - 5 Hz, 5 - 10 Hz, 10 - 15 Hz, 8 - 25 Hz, 15 - 25 Hz, 20 - 50 Hz). If a possible event could be seen it was copied to a new database.

The sorted events were then more rigorously examined to try to discriminate whether it was a real event or a cryogenic signal. Very impulsive (relatively weak) signals with no sign of a second phase were also not further examined as there would be no hope of locating them. Finally only the needed datafiles for the event were re-extracted to miniSEED with tools we developed using the OBSpy package (also interfaced to *libmseed*) (Beyreuther *et al.*, 2010; Trebbin, 2010) before phases were picked.

5.2 Data overview

Table 5.1 shows an overview of the final number of the sorted events (from drift G3). The identification number follows the standard S-file convention used for the Nordic event file format (Ottemöller *et al.*, 2011) constructed by the date and time of the event as well as a number which is incremented to distinguish events that occur in the same hour. Table 5.2 and 5.3 shows the arrival times for the P-phase at each station for the events. Note that unless location has been attempted the pickings are not very accurate.

The seismometer data has not been corrected for instrument response. The Nanometrics Trillium 120P has an approximately flat frequency response to velocity in the frequencies (1 – 100 Hz), and a flat response to acceleration above that. The digitizer for the seismometer samples at 250 Hz which maps to a Nyquist frequency of 125 Hz.

| Initial sorting | | Final sorting | |
|-----------------|----|---------------|----|
| Date | # | Date | # |
| 2012-09-01 | 6 | 2012-09-01 | 1 |
| 2012-09-02 | 15 | 2012-09-02 | 4 |
| 2012-09-03 | 12 | 2012-09-03 | 9 |
| 2012-09-04 | 12 | 2012-09-04 | 10 |
| 2012-09-05 | 15 | 2012-09-05 | 13 |
| 2012-09-06 | 5 | 2012-09-06 | 4 |
| 2012-09-07 | 1 | 2012-09-07 | 0 |
| Total | 66 | Total | 41 |

Table 5.1: Initial number (left) and final number (right) of events for drift GAK3

| | Event name | GAK2 / GAKS | GAK3 | GAK4 |
|-------------------------|---------------------|---------------------|---------------------|---------------------|
| Arrival time of P-phase | 01-1700-00L.S201209 | 2012-09-01 17:46:54 | 2012-09-01 17:46:54 | 2012-09-01 17:46:54 |
| | 02-0800-00L.S201209 | 2012-09-02 08:14:40 | 2012-09-02 08:14:40 | 2012-09-02 08:14:40 |
| | 02-1000-00L.S201209 | 2012-09-02 10:06:50 | 2012-09-02 10:06:57 | 2012-09-02 10:06:48 |
| | 02-2000-00L.S201209 | 2012-09-02 20:03:05 | 2012-09-02 20:03:04 | 2012-09-02 20:03:05 |
| | 02-2100-00L.S201209 | 2012-09-02 21:36:27 | 2012-09-02 21:36:27 | 2012-09-02 21:36:28 |
| | 03-0100-00L.S201209 | 2012-09-03 01:07:14 | 2012-09-03 01:07:13 | 2012-09-03 01:07:15 |
| | 03-0300-00L.S201209 | 2012-09-03 03:35:41 | 2012-09-03 03:35:41 | 2012-09-03 03:35:40 |
| | 03-0700-01L.S201209 | 2012-09-03 07:20:25 | 2012-09-03 07:20:26 | 2012-09-03 07:20:26 |
| | 03-1000-00L.S201209 | 2012-09-03 10:32:46 | 2012-09-03 10:32:48 | 2012-09-03 10:32:43 |
| | 03-1000-01L.S201209 | 2012-09-03 10:29:31 | 2012-09-03 10:29:32 | 2012-09-03 10:29:30 |
| | 03-1400-00L.S201209 | 2012-09-03 14:19:25 | 2012-09-03 14:19:25 | 2012-09-03 14:19:26 |
| | 03-1500-00L.S201209 | 2012-09-03 15:57:40 | 2012-09-03 15:57:41 | 2012-09-03 15:57:40 |
| | 03-2200-00L.S201209 | 2012-09-03 22:33:00 | 2012-09-03 22:33:00 | 2012-09-03 22:33:00 |
| | 03-2300-00L.S201209 | 2012-09-03 23:34:30 | 2012-09-03 23:34:30 | 2012-09-03 23:34:30 |
| | 04-0700-00L.S201209 | 2012-09-04 07:55:40 | 2012-09-04 07:55:38 | 2012-09-04 07:55:37 |
| | 04-0900-00L.S201209 | 2012-09-04 09:25:06 | 2012-09-04 09:25:07 | 2012-09-04 09:25:06 |
| | 04-1000-00L.S201209 | 2012-09-04 10:26:01 | 2012-09-04 10:26:02 | 2012-09-04 10:26:01 |
| | 04-1400-00L.S201209 | 2012-09-04 14:08:17 | 2012-09-04 14:08:18 | 2012-09-04 14:08:17 |
| | 04-1400-01L.S201209 | 2012-09-04 14:24:01 | 2012-09-04 14:24:02 | 2012-09-04 14:24:01 |
| | 04-1400-02L.S201209 | 2012-09-04 14:26:38 | 2012-09-04 14:26:39 | 2012-09-04 14:26:38 |
| | 04-1600-01L.S201209 | 2012-09-04 16:52:43 | 2012-09-04 16:52:45 | 2012-09-04 16:52:44 |
| | 04-1700-00L.S201209 | 2012-09-04 17:07:33 | 2012-09-04 17:07:34 | 2012-09-04 17:07:33 |
| | 04-1900-00L.S201209 | 2012-09-04 19:09:30 | 2012-09-04 19:09:31 | 2012-09-04 19:09:30 |
| | 04-2000-00L.S201209 | 2012-09-04 20:42:09 | 2012-09-04 20:42:09 | 2012-09-04 20:42:06 |
| | 05-0100-00L.S201209 | 2012-09-05 01:16:02 | 2012-09-05 01:16:03 | 2012-09-05 01:16:03 |
| | 05-0100-01L.S201209 | 2012-09-05 01:18:29 | 2012-09-05 01:18:29 | 2012-09-05 01:18:30 |
| | 05-0200-00L.S201209 | 2012-09-05 02:00:48 | 2012-09-05 02:00:49 | 2012-09-05 02:00:48 |
| | 05-0300-00L.S201209 | 2012-09-05 03:13:34 | 2012-09-05 03:13:36 | 2012-09-05 03:13:35 |

Table 5.2: Event P-arrival times for drift G3, continued below in table 5.3.

| Arrival time of P-phase | Event name | GAK2 / GAKS | GAK3 | GAK4 |
|-------------------------|---------------------|---------------------|---------------------|---------------------|
| | 05-0400-00L.S201209 | 2012-09-05 04:57:04 | 2012-09-05 04:57:03 | 2012-09-05 04:57:04 |
| | 05-0500-00L.S201209 | 2012-09-05 05:01:02 | 2012-09-05 05:01:02 | 2012-09-05 05:01:02 |
| | 05-0600-00L.S201209 | 2012-09-05 06:18:46 | 2012-09-05 06:18:45 | 2012-09-05 06:18:45 |
| | 05-0900-00L.S201209 | 2012-09-05 09:00:44 | 2012-09-05 09:00:44 | 2012-09-05 09:00:44 |
| | 05-0900-01L.S201209 | 2012-09-05 09:05:24 | 2012-09-05 09:05:24 | 2012-09-05 09:05:24 |
| | 05-1500-00L.S201209 | 2012-09-05 15:24:23 | 2012-09-05 15:24:22 | 2012-09-05 15:24:21 |
| | 05-1700-00L.S201209 | 2012-09-05 17:15:20 | 2012-09-05 17:15:18 | 2012-09-05 17:15:19 |
| | 05-1700-01L.S201209 | (unclear) | 2012-09-05 17:36:06 | 2012-09-05 17:36:06 |
| | 05-1900-00L.S201209 | 2012-09-05 19:58:43 | 2012-09-05 19:58:42 | 2012-09-05 19:58:42 |
| | 06-0100-00L.S201209 | 2012-09-06 01:57:13 | 2012-09-06 01:57:12 | 2012-09-06 01:57:11 |
| | 06-1900-00L.S201209 | 2012-09-06 19:34:17 | 2012-09-06 19:34:24 | 2012-09-06 19:34:19 |
| | 06-2100-00L.S201209 | 2012-09-06 21:50:17 | 2012-09-06 21:50:17 | 2012-09-06 21:50:15 |
| | 06-2200-00L.S201209 | 2012-09-06 22:59:08 | 2012-09-06 22:59:09 | 2012-09-06 22:59:08 |

Table 5.3: Event P-arrival times for drift G3 continued.

5.3 Event discrimination and phase identification

Potential events were discriminated from cryogenic events and noise by checking whether it was present on all three stations and whether secondary phases could be identified. Also, if the seismometer was functioning, a stronger vertical component than horizontal would indicate an event from below and not originating in the sea ice (as also Schlindwein *et al.* (2007) assumes).

A lot of noise from the hovercraft and movement around the hovercraft can be seen on stations GAK2 and GAKS (section 5.6.1). It is either characteristic engine noise or impulsive signals. Both are easy to identify. Neither the engine noise nor noise from activity around the hovercraft can be identified on the other stations.

Because of the large velocity contrast between water and seafloor, the rays of the phases travel almost vertically through the water column. As can be seen from figure 5.3.1 the water depth may vary considerably between the stations and their different ray paths. The traveltime difference between P (blue line) and SP (red line) will not change considerably after the seafloor interface, however the onset times for the first phase at the stations may still be significantly affected by the roughly 1000 m difference in travel distance in the water column between the stations. Since the velocity contrast is large also for the SP phase

at the seafloor the intersection points for the ray paths of both P and SP phases at the seafloor are close.

Figure 5.3.1 shows the solution for event 04-1400-02L with ray paths P, SP and first multiple. The water multiples are considerably scattered by the rough seafloor so that tracing rays for these phases between stations and possible locations is difficult. A good coverage of station to grid cell mappings is required to establish a reliable global minimum in the error between calculated and observed travel times over the grid cells. Only two interfaces below the seafloor are plotted in this figure.

A strong velocity gradient in the water column below the surface in the Arctic causes a wave guide. For events at some distance a T-phase (tertiary wave, see Figure 5.4.3) traveling in this channel could be observed. It develops as the signal is scattered at the ice and is reflected back up to the ice in this low velocity layer (Keenan & Dyer, 1984). In the open ocean a similar SOFAR channel is located at approximately 700 m depth (Kristoffersen, 2011) and the name T-phase is also used to describe the wave trapped in this layer (Dziak *et al.*, 2012). Läderach & Schlindwein (2011) observed this phase for events located more than ca. 50 km away.

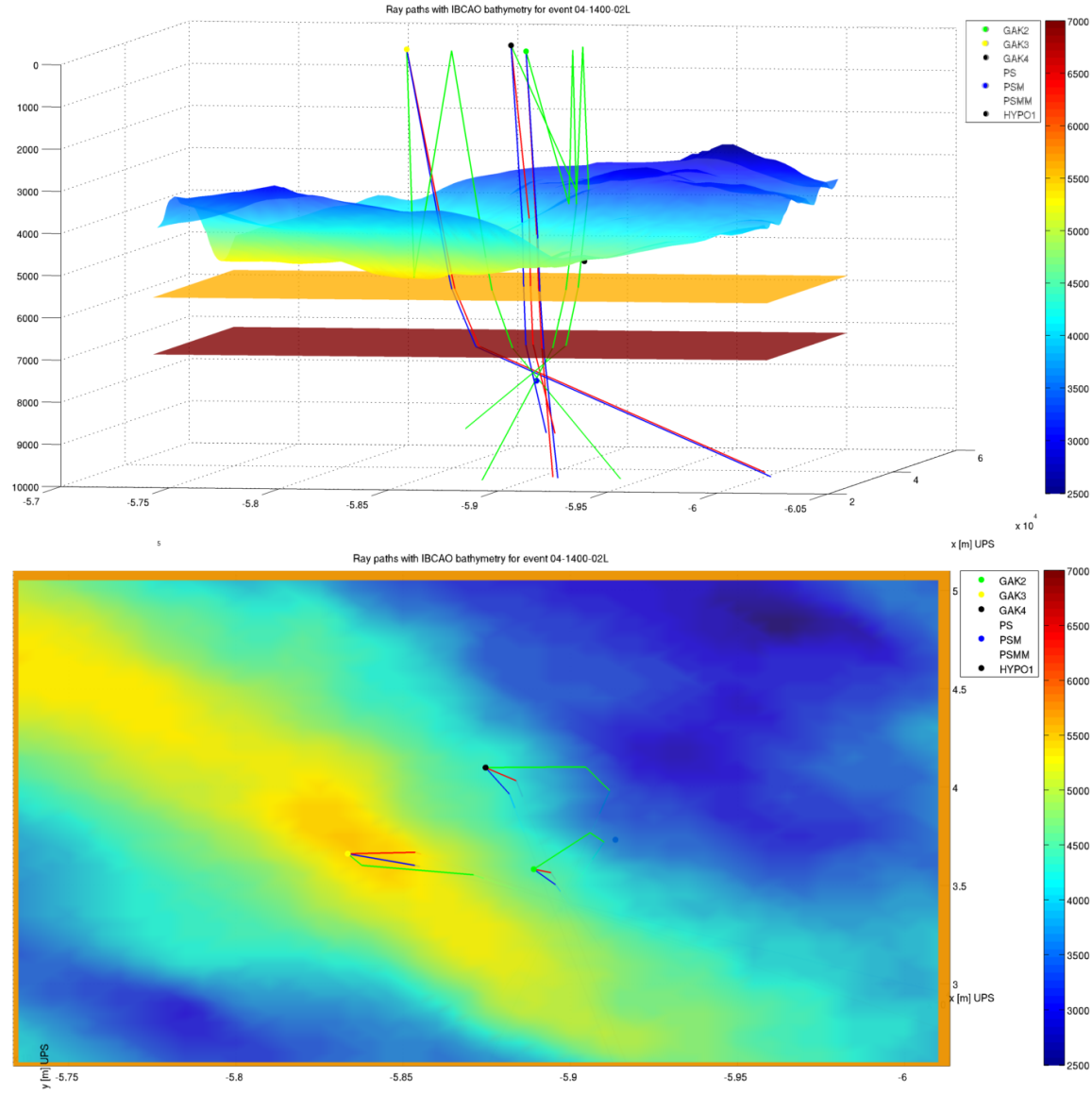


Figure 5.3.1: Ray paths for event 04-1400-02L with IBCAO bathymetry from the side (top) and the top (bottom).

Except for the strongest signals, most events are identified by their frequency content above 20 Hz as can be seen in the weak event 03-2200-00L.201209 (Figure 5.4.1). The event is completely hidden in the ambient noise levels in the lower frequencies (< 10 Hz). A spectrogram of the event on all stations is plotted in figure 5.4.2.

5.4 Event types

5.4.1 Weak event

Event 03-2200-00 (Figure 5.4.1) is an example of a weak event. It was recorded on all stations, and although the lower frequency content drown in the ambient noise, it is clearly visible in frequencies above 20 Hz. Whether the second peak is a multiple or a new event is not clear. The spectrogram of the event at all stations is given in figure 5.4.2.

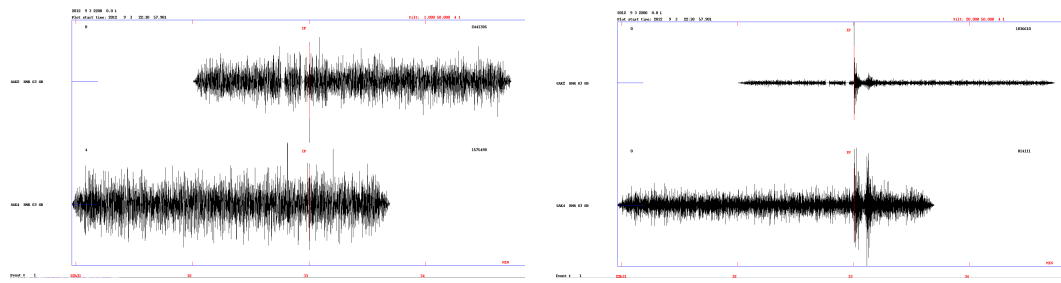


Figure 5.4.1: Event 03-2200-00L filtered between 1 - 50 Hz (left) and 20 - 50 Hz (right) on stations GAK2 (top) and GAKS (bottom).

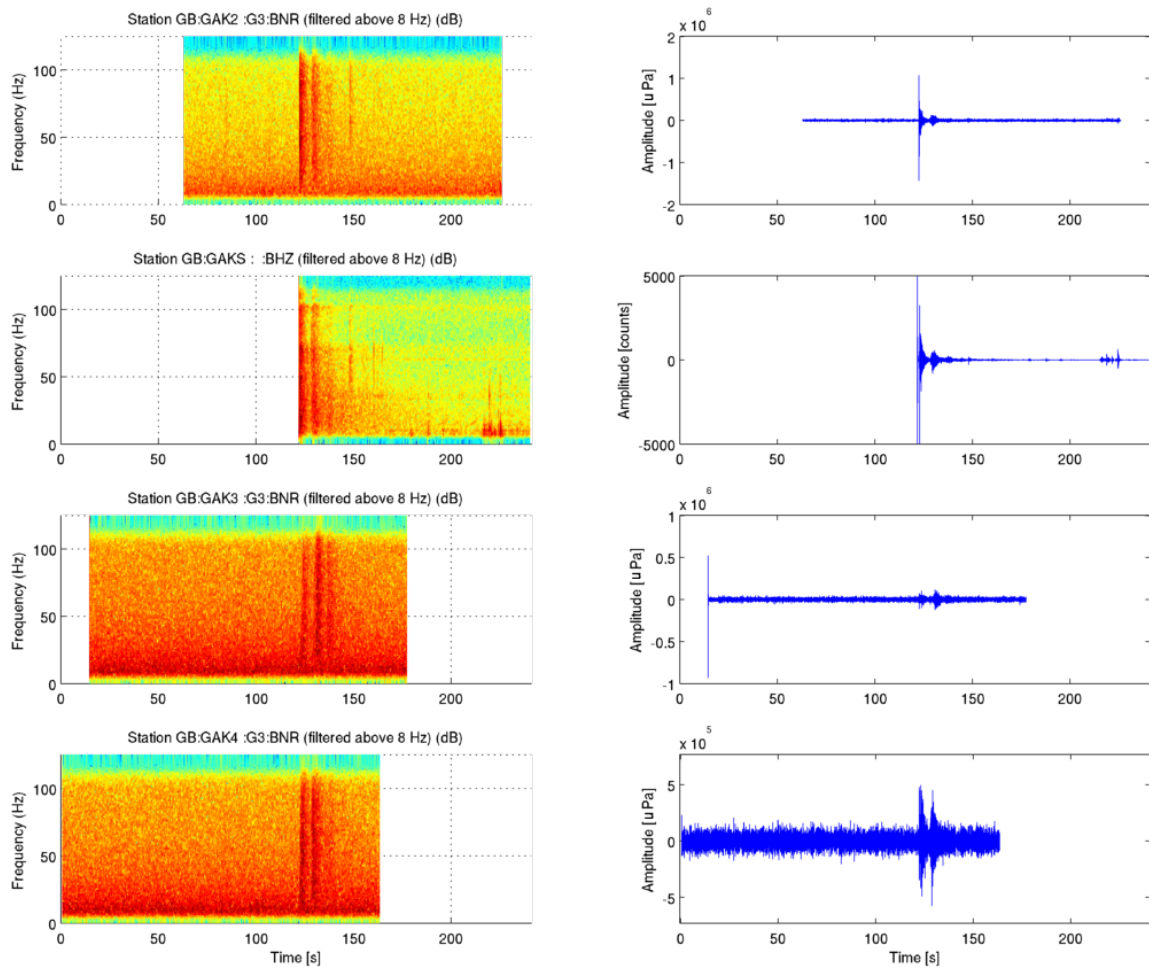


Figure 5.4.2: Spectrogram of event 03-2200-00L for the individual stations (filtered above 8 Hz).

A trace of an event with a possible T-phase is shown in the trace of event 04-2000-00L.S201209 (Figure 5.4.3). For the T-phase to develop the event presumably originates more than 50 km away from the recording station.

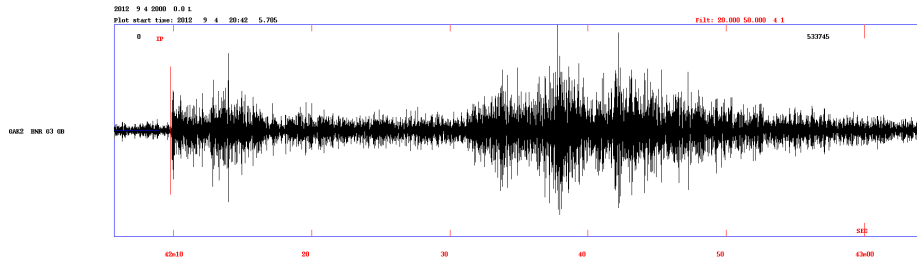


Figure 5.4.3: Trace from station GAK2 of event 04-2000-00L.S201209 showing a possible T-phase tail.

5.4.2 Strong event

Figure 5.4.4 shows the strongest signal recording. The event could be felt on board the hovercraft as slight rattling. Figure 5.4.5 is a plot of the spectrograms for the stations. For station GAK2 (top) the subsequent event 04-1400-02L can be seen. This event had a similar waveform as the previous. However it was much weaker, and the energy had higher frequency.

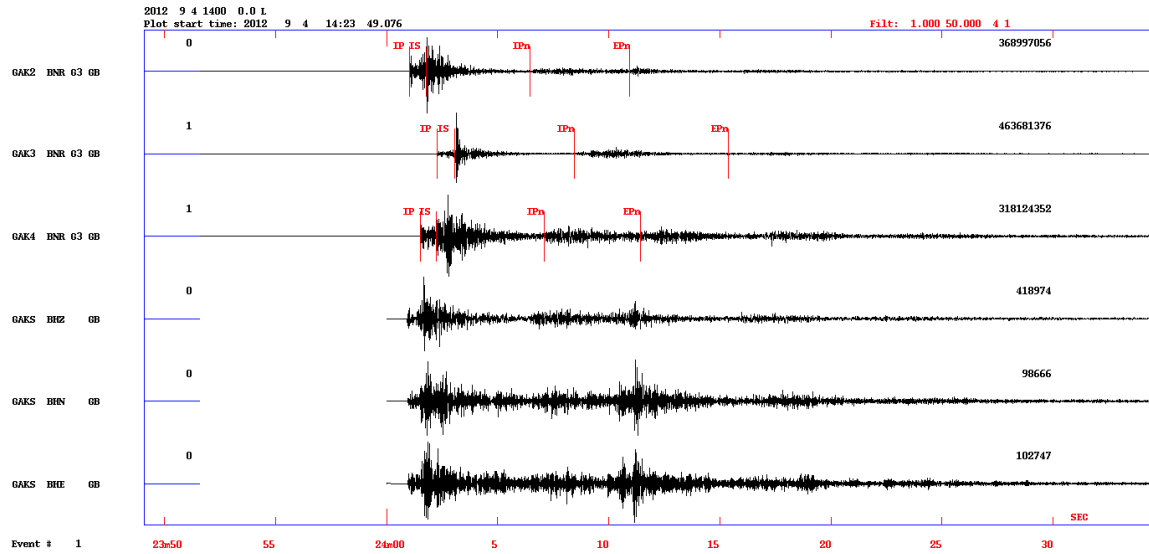


Figure 5.4.4: Trace of event 04-1400-01L.S201209, filtered between 1 - 50 Hz. Phase pickings are shown for the buoys. Station GAKS (the seismometer, bottom three traces) is located a few meters from station GAK2.

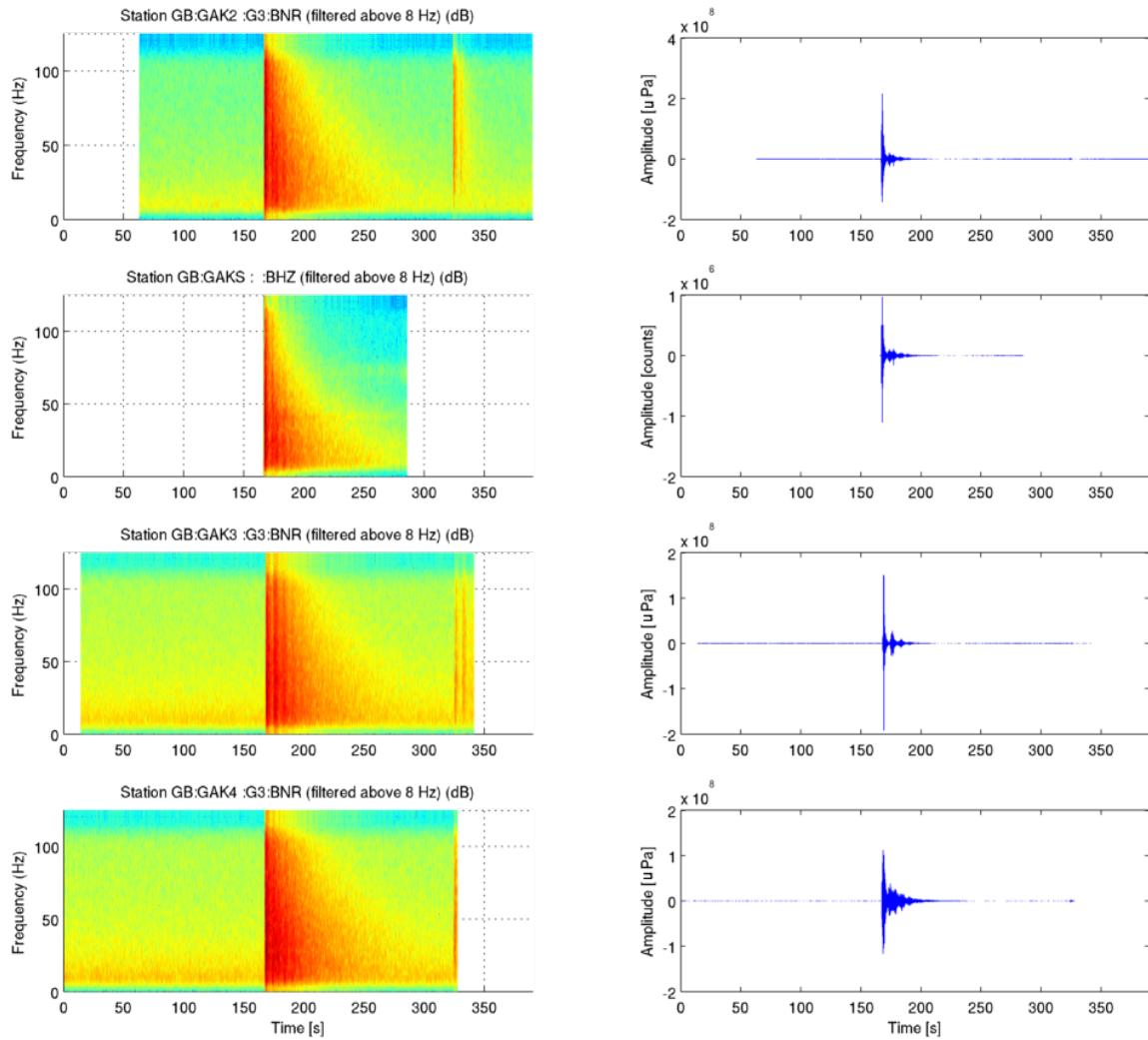


Figure 5.4.5: Spectrogram of event 04-1400-01L (filtered above 8 Hz) for all stations.

5.5 Seismometer

Based on comparing the onset times for the adjacent stations GAK2 and GAKS, there seems to be a systematic timing error where station GAK2 is about 0.1 second behind the seismometer (GAKS). Since there is no seismometer located with the other stations it is not possible to say whether the error is constant between the stations.

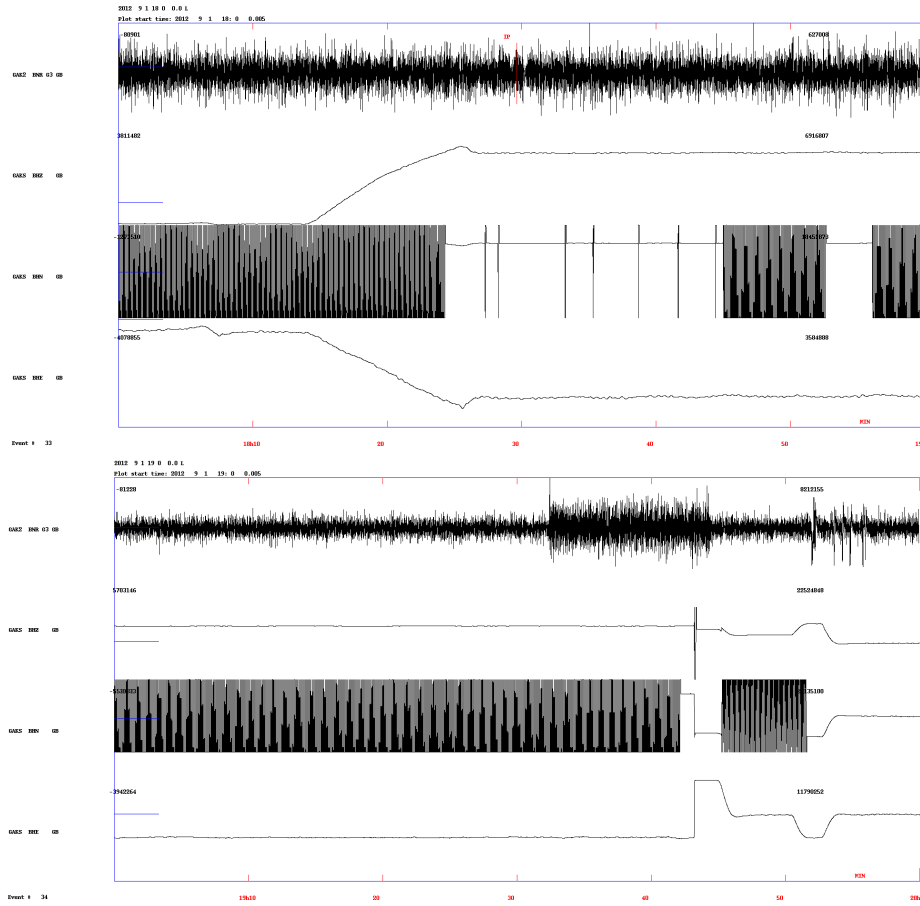


Figure 5.5.1: Seismometer failure, top: Seismometer failure due to drift or tilting. One of the horizontal components is unable to recover (the digitizer was resetting the seismometer if the output passes a set level for a predefined time). Bottom: Seismometer has been re-balanced manually and all components recover.

Figure 5.5.1 shows the output from the seismometer as it is influenced by ice drift and tilt due to melting. One of the horizontal components are unable to recover, most likely because of tilt. The digitizer was configured to reset the mass if it was above a set level for a predefined time. If the failure was due to ice drift alone the seismometer should recover by itself after being reset. The bottom figure shows the output as the seismometer is being re-balanced manually. Although the vertical component shows drift (possibly due to tilting and then influence from ice drift) it still produces usable output when the lower frequencies have been filtered away.

5.6 Ambient noise levels

The ambient noise levels in the Arctic are largely dependent on the ice movement and thus on wind and ocean currents. Noise levels build up and decay with changing surface conditions during periods on the order of more than a day. Wind on the surface of the ice and currents on the subsurface, together with ice deformation and ridge forming contribute to the ambient noise (Kristoffersen, 2011). Sound can travel great ranges in the Arctic because of the upward refraction from the SOFAR channel and the downward reflection from the ice (Kutschale, 1961).

Figures 5.6.1, 5.6.3 and 5.6.4 shows the calculated probability density functions (PDF) for the power density spectrums (PSD) calculated for 2 minute segments of a sample day. In general these PDFs agree well with the expected ambient noise distribution in the Arctic (Makris & Dyer, 1986; Kristoffersen, 2011). A second PDF for station GAK2 (figure 5.6.2) show a small peak around 20 Hz which could be observed for some periods. Fin and blue whales communicate at these frequencies (Klinck *et al.*, 2012) and even though it is far from the ice edge, they could be a possible source of this because of the long range of the sound energy. Changing propagation parameters and local sensitivity between the stations could explain the difference in amplitude between the stations.

A peak at 70 Hz for station GAK4, but less persistent than the 20 Hz peak, could be related to changing ambient noise levels. This station was located closer to open water and this might explain the difference from the other stations. Notice that the general noise levels are higher for this station than the others. Otherwise the distribution is generally still the same.

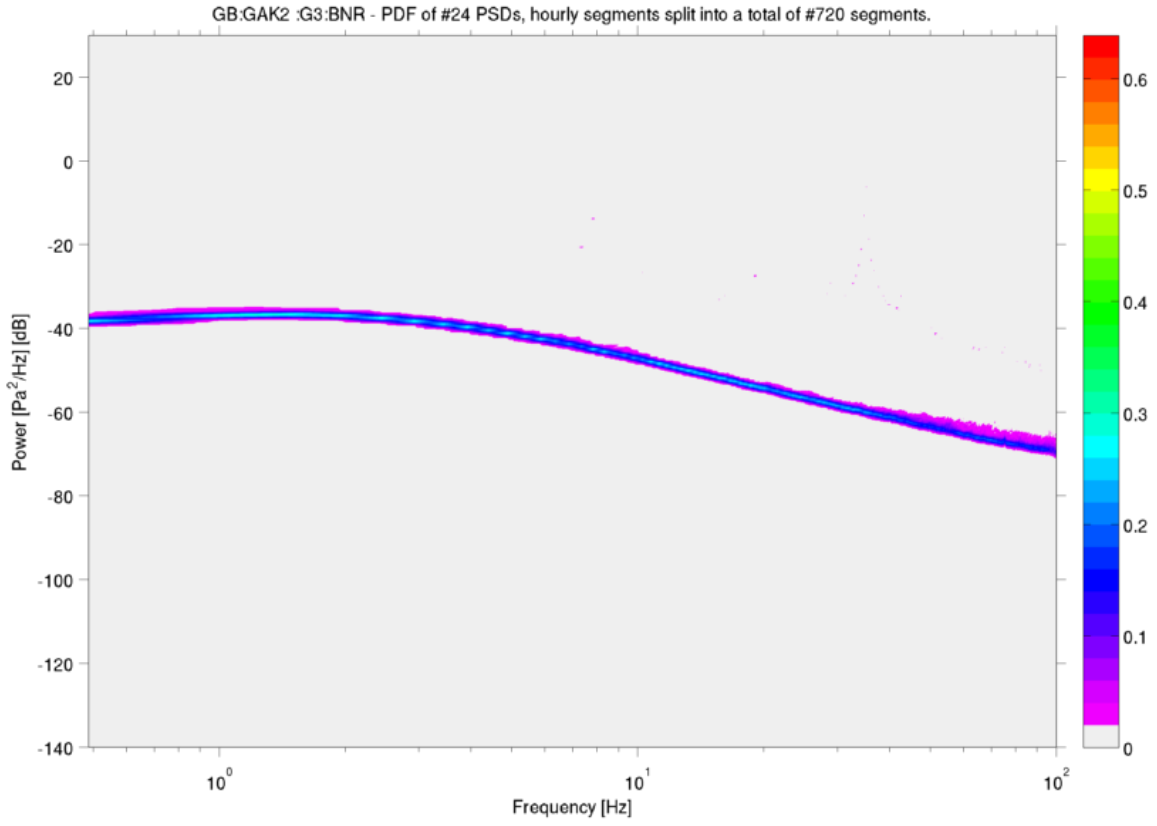


Figure 5.6.1: PDF of power spectrum density for station GAK2 (2012-09-03).

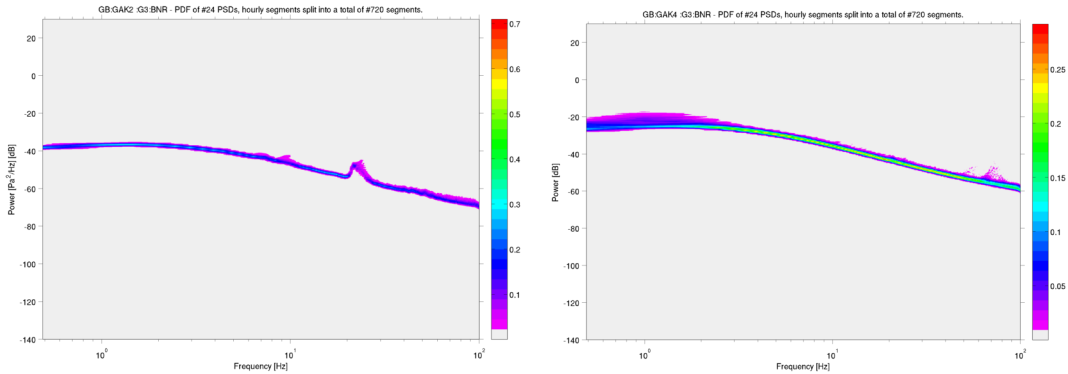


Figure 5.6.2: PDF of power spectrum density for station GAK2 (left) (2012-09-05) showing a 20 Hz peak and GAK4 (right) (2012-09-01) showing a small peak around 70 Hz .

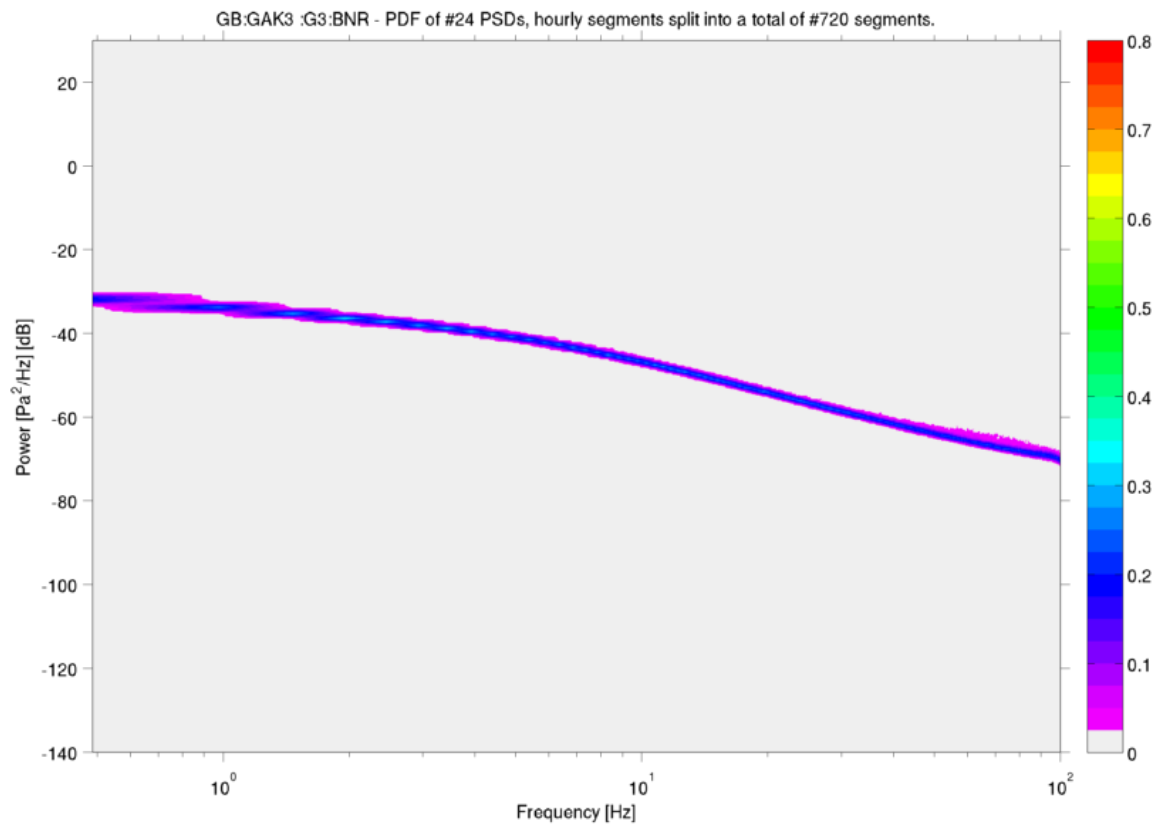


Figure 5.6.3: PDF of power spectrum density for station GAK3 (2012-09-02).

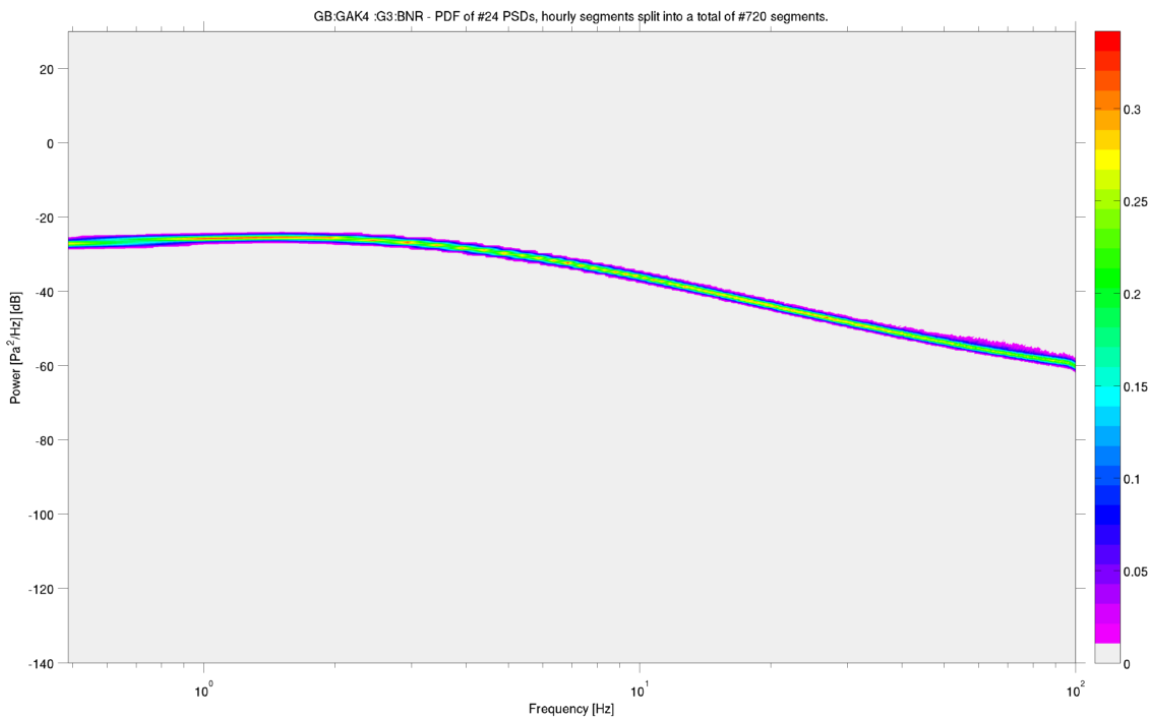


Figure 5.6.4: PDF of power spectrum density for station GAK4 (2012-09-02).

5.6.1 Noise from Hovercraft

Figure 5.6.5 shows the trace and frequency spectrogram with the engine of the hovercraft running (for charging hovercraft batteries). No signal can be seen on the far stations. A spike appears on the seismometer roughly in the middle of this time series, probably related to the hovercraft noise, but it is hard to determine the exact source for it.

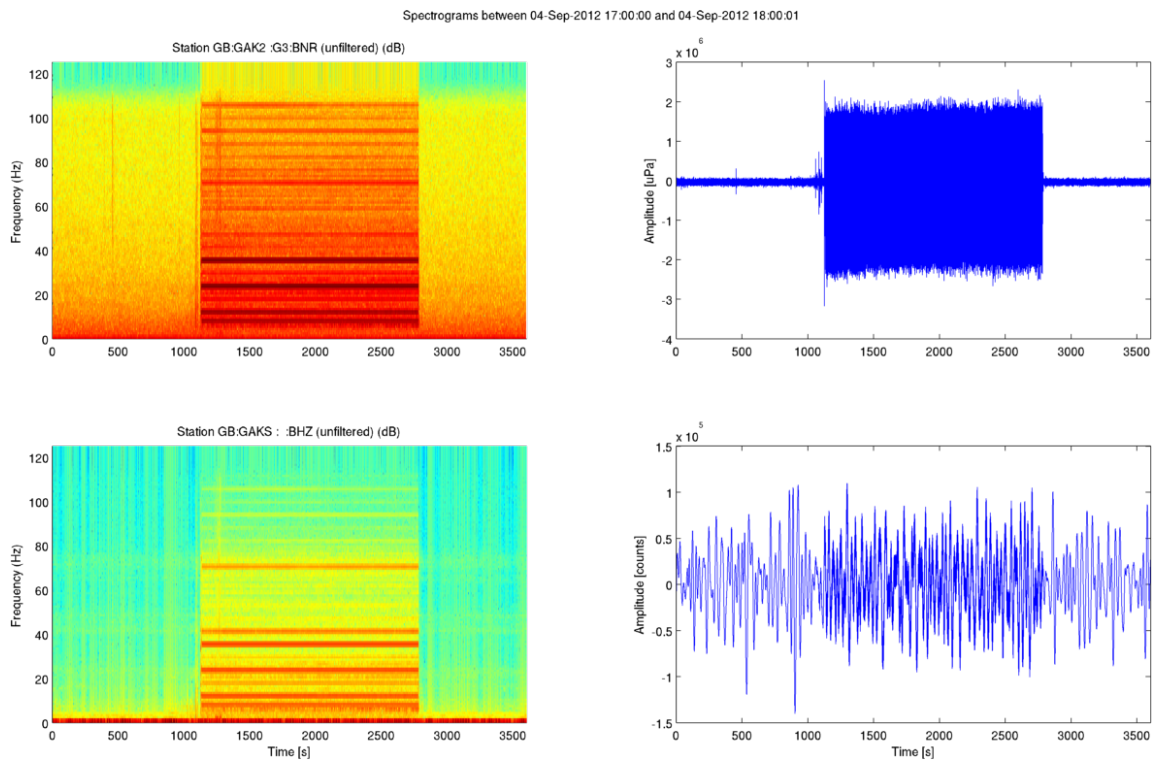


Figure 5.6.5: Hovercraft engine noise spectrogram and trace.

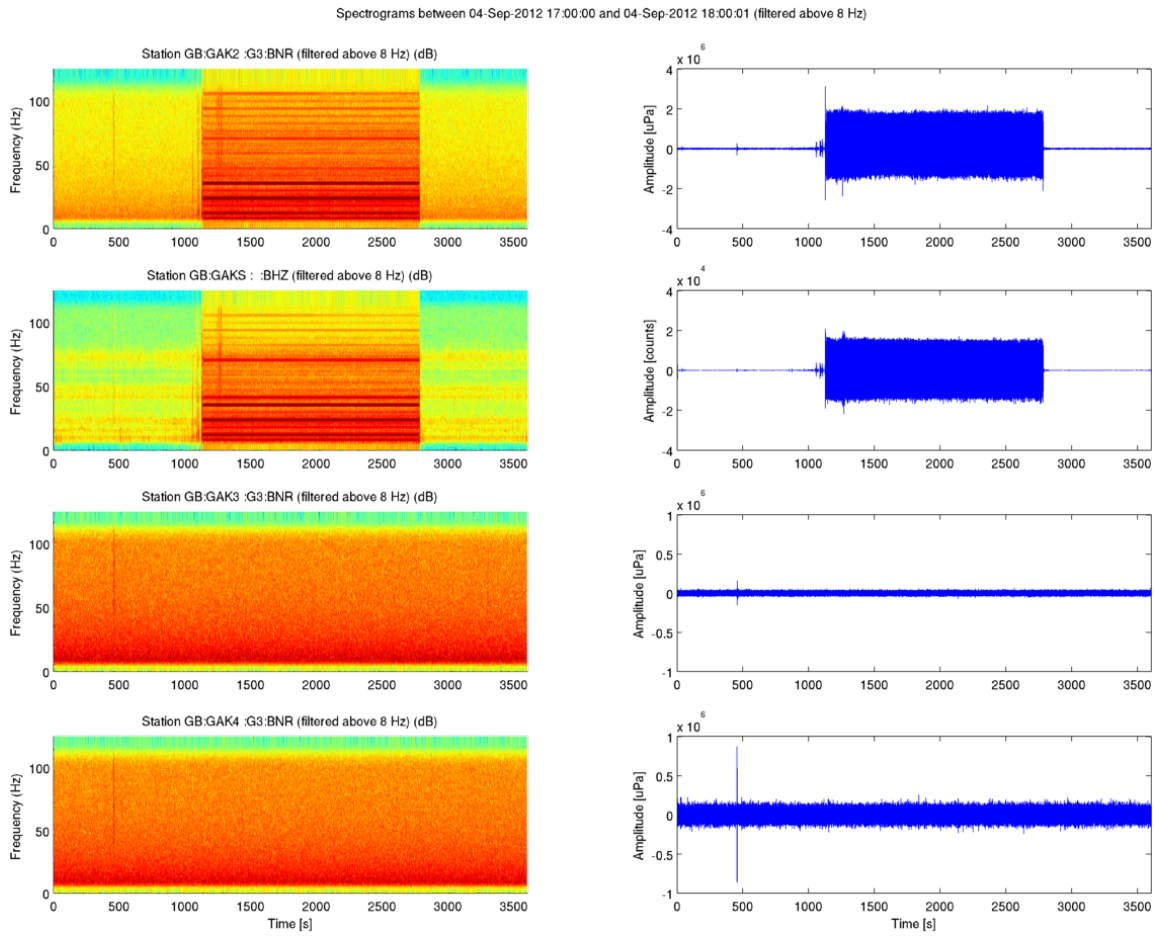


Figure 5.6.6: Hovercraft engine noise spectrogram and trace for all stations (both filtered above 8 Hz).

5.6.2 Cryogenic, human and discarded events

For the seismometer station and station GAK2 which were placed next to the hovercraft, noise that is likely to originate from walking on the ice or activity around the hovercraft can be seen in figure 5.6.7. It is often difficult to distinguish these from potentially cryogenic signals only visible on this station. No man made signals can be seen on the far stations.

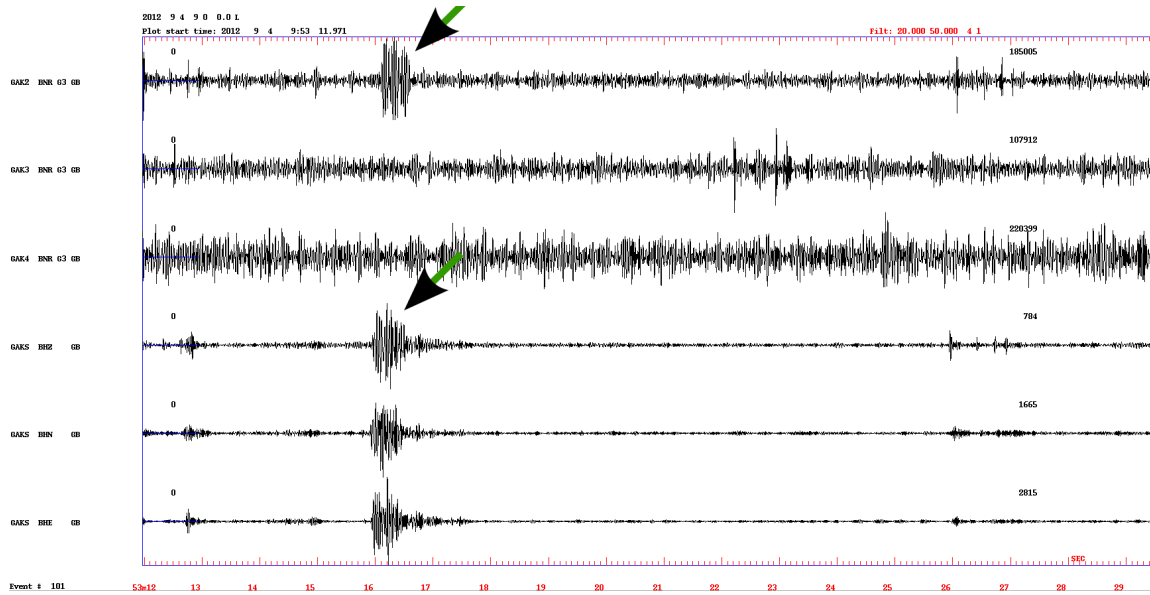


Figure 5.6.7: Man-made noise, most likely man-made noise (green arrows) only recorded on seismometer and station GAK2 next to the hovercraft.

Noise likely to originate from ice movement can be seen in figure 5.6.8, two (probably cryogenic) events that could be related are seen on station GAK4 and the seismometer and GAK2 stations next to the hovercraft. A time gap results in an apparent spike because of filtering on station GAK3.

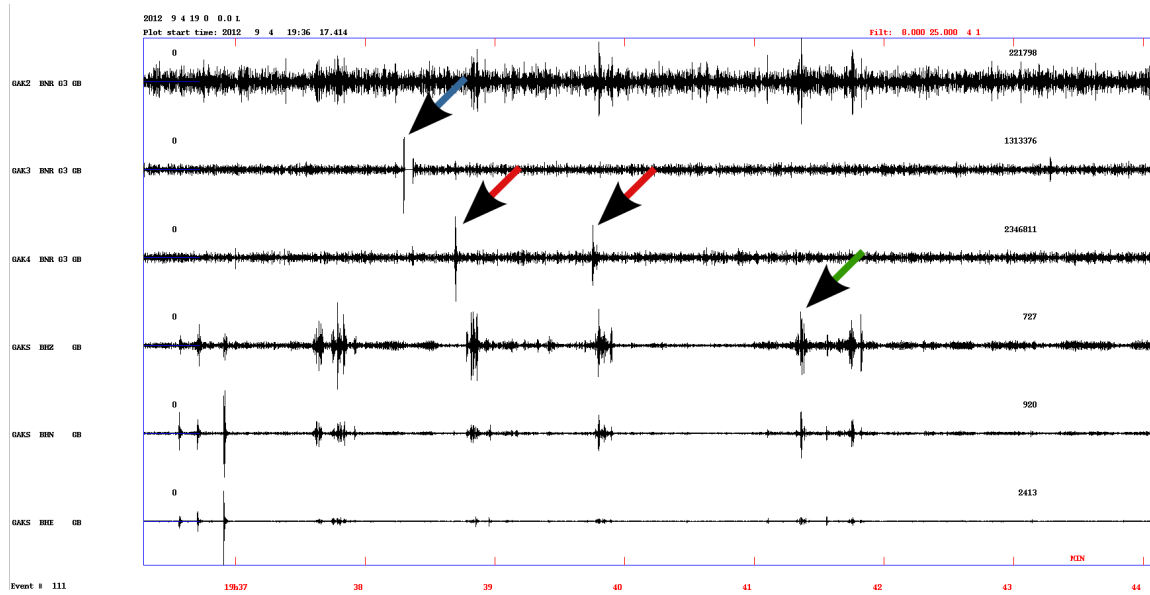


Figure 5.6.8: Cryogenic and man-made noise, red arrows show cryogenic signals, green either man-made or cryogenic while blue is a time glitch resulting in a spike in the filtered data. The two events at the red arrows could be the same as are recorded slightly later on stations GAKS and GAK2, they are however not visible on station GAK3. The horizontal components of the seismometer show higher amplitude than for the vertical.

The exact origin of these impulsive signals are not easy to determine, but they are filtered out either because they are not present on all stations or do not show secondary arriving phases like a seismic event would.

5.7 Locations

Schlindwein *et al.* (2007) compiled a velocity model for the Sparsely Magmatic Zone from refraction seismic profiles shot during AMORE 2001 (Jokat *et al.*, 2003; Jokat & Schmidt-Aursch, 2007). In this thesis a slightly modified version (linear interpolated values) shown in table 5.4 is used. For all locations the depths of the velocity interfaces are kept constant. In the HYPOSEARCH routine, the seafloor interface is defined by the IBCAO bathymetry (Jakobsson *et al.*, 2012) (although the IBCAO can be several hundred meters off (Schlindwein *et al.*, 2007)). A constant water depth of 4.3 km is used as guess

for the depth of the seafloor layer for the 1D location routines. The simplicity and lack of constraints in the velocity model is a source of considerable uncertainty.

| Depth [m] | V_P [m/s] | V_S [m/s] | |
|-------------|-------------|-------------|------------|
| 0 | 1500 | 0 | (water) |
| 4300 | 3500 | 2020 | (seafloor) |
| 5650 | 5400 | 3120 | |
| 7000 | 7400 | 4500 | |
| 10000 | 8100 | 4680 | |
| below 40000 | 8250 | 4760 | |

Table 5.4: Velocity model used for locating events

The events below have been located using the HYPOCENTER routine as well as our HYPOSEARCH routine. HYPOSAT (Schweitzer, 2001) was found to calculate mismatching traveltimes for the short distance synthetic tests we made with the TauP package (Crotwell & Owens, 1999) and our own calculations.

For the locations we have only used picks from station GAK2 and not the seismometer (GAKS) since they are located next to each other.

5.7.1 Event: 03-2300-00L.S201209

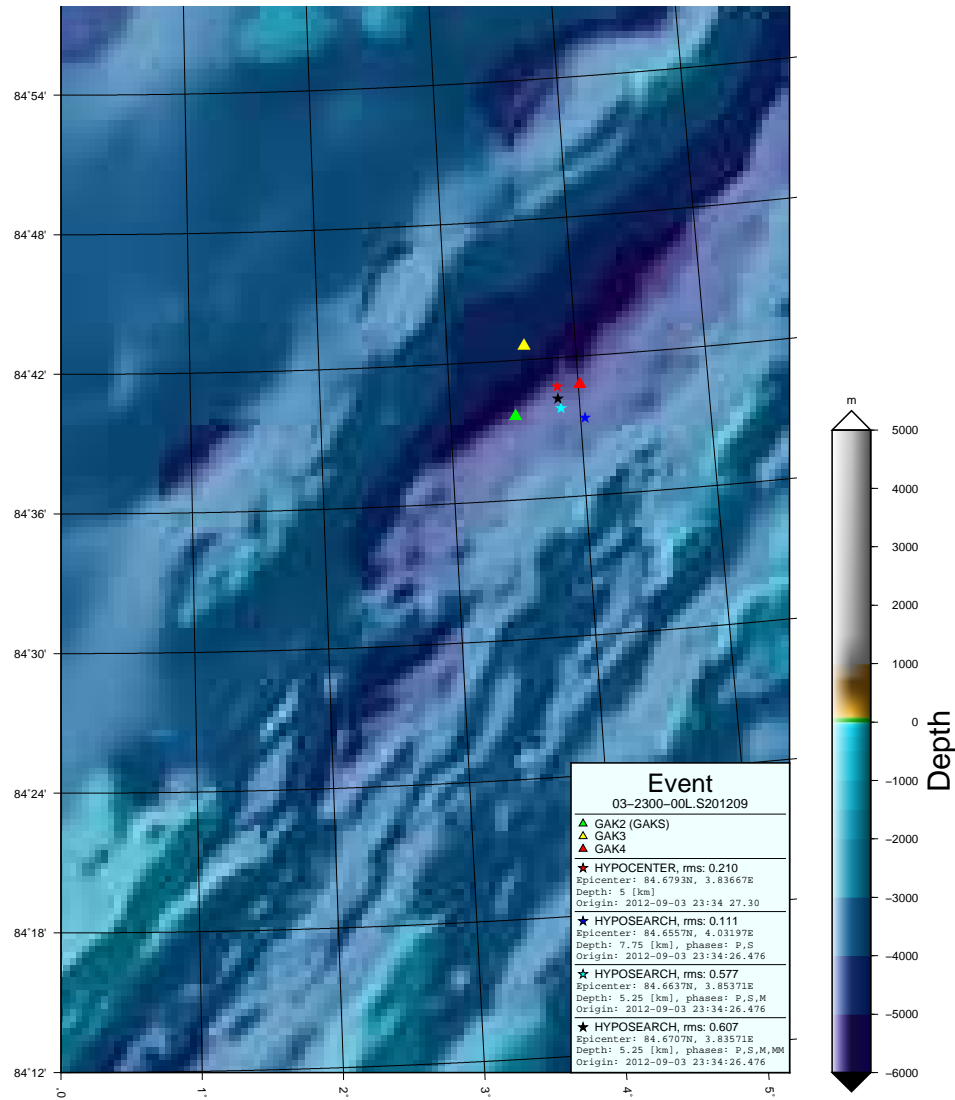


Figure 5.7.1: Location for event 03-2300-00L. The triangles show the station locations at the time of recording, the stars show the solutions for the same event using HYPOCENTER (red), HYPOSEARCH (only considering P and SP phase) (blue), HYPOSEARCH (only considering P, SP and M phases) (cyan) and HYPOSEARCH (considering all phases) (black).

Figure 5.7.1 show the results of locating event 03-2300-00. HYPOCENTER (red star) places the source below the array. The HYPOSEARCH routine, taking water multiples into account, places the earthquake nearby (cyan and black star).

HYPOSEARCH will however be affected by the difficulty of tracing the multiples (rough topography causing complex ray paths), since ray path solutions for these phases are hard to find at steeper take off angles. Also, the picking of the multiples are less accurate. The solution based only on P and S phases (blue star), using HYPOSEARCH, are therefore more trustworthy.

The solution stands and falls with correct identification and picking of the SP-phase (S to P at seafloor), which is not at all straight forward. It is both unclear whether the phase really is SP and it is difficult to pinpoint the exact onset of the often emergent signal (Figure 5.7.3).

5.7.2 Event: 04-1400-01L.S201209 and 04-1400-02L.201209

The event *04-1400-01L.S2012* was the strongest event recorded during the experiment. It was so strong that it could be felt aboard the hovercraft as a slight rattling. Figure 5.4.4 shows the recorded traces.

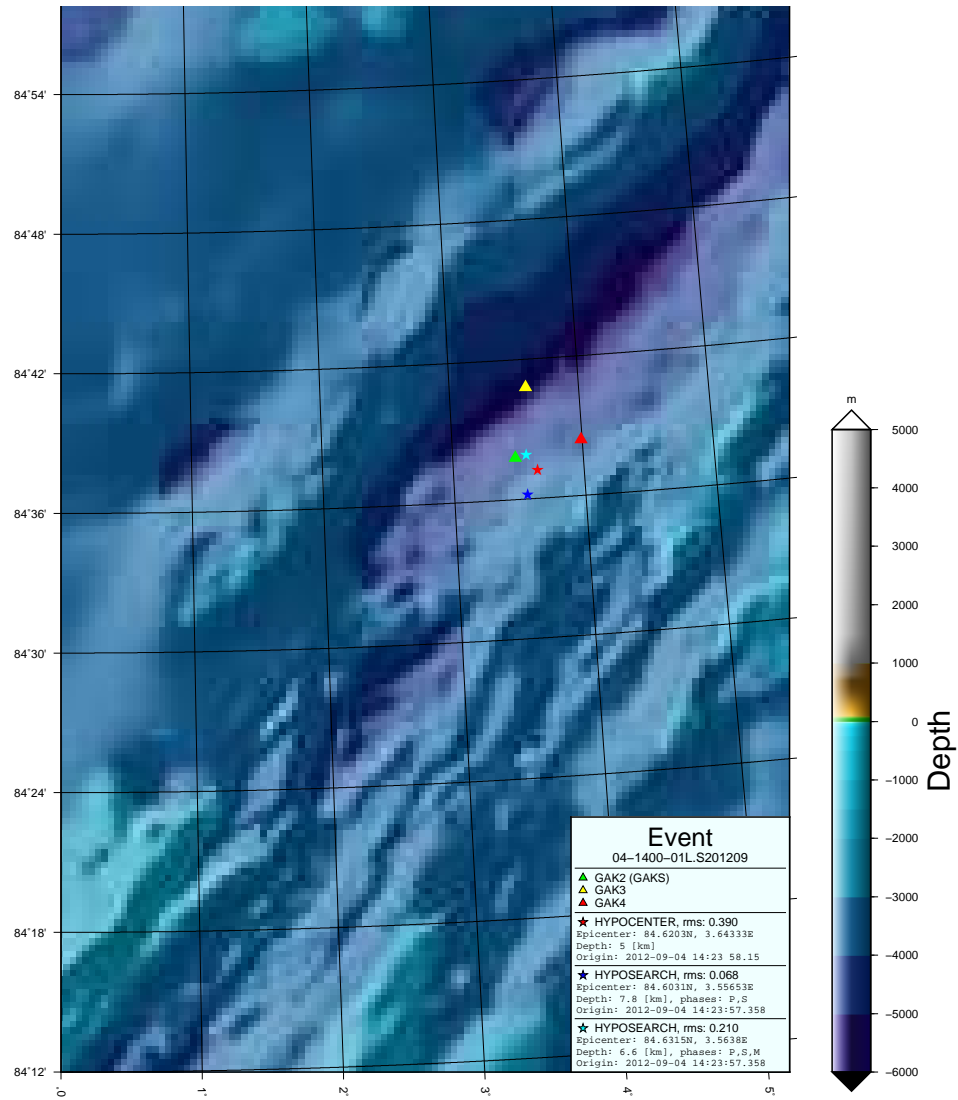


Figure 5.7.2: Location for event 04-1400-01L. The triangles show the station locations at the time of recording, the stars show the solutions for the same event using HYPOCENTER (red), HYPOSEARCH (only considering P and SP phase) (blue) and HYPOSEARCH (only considering P, SP and M phases) (cyan).

As can be seen from the traces, the onset times differ although the differences (SP - P) are fairly similar. This may be a timing error, but it can also be explained by the difference in

water depth between the stations. Since the ray paths are near vertical in the water column the difference of more than 1000 m depth should be observable in different onset times. Since the ray paths are similar, the differences ($SP - P$) will no longer change considerably after the phases have entered the water column. The HYPOSEARCH solution only considering the P and SP phase is plotted as a blue star while the HYPOCENTER solution is plotted as a red star (figure 5.7.2).

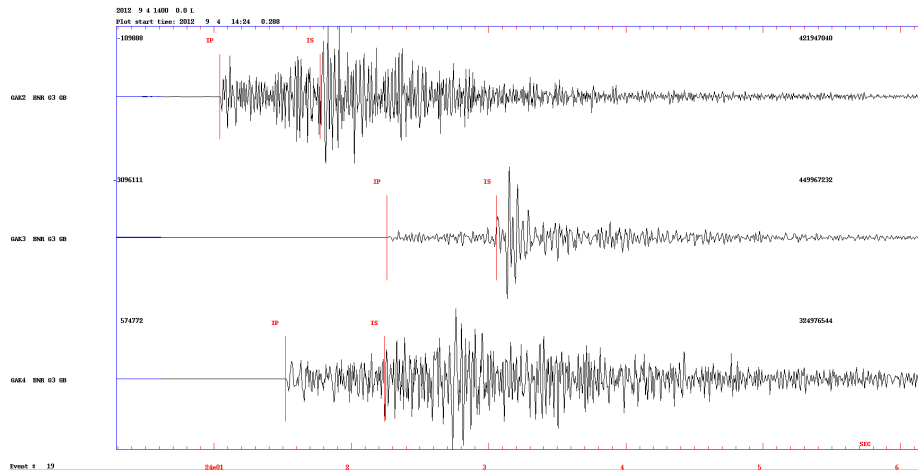


Figure 5.7.3: Traces for the hydrophone stations of event 04-1400-01L.S201209 with phase pickings. The emergent character of the assumed SP phase is particularly visible in the top (GAK2) and bottom (GAK4) traces.

Figure 5.7.3 shows a zoomed in section for the traces on the three hydrophone stations for event 04-1400-01L, the difference in onset time for the P phase does not match the almost equal SP-P time for a flat bathymetry. The emergent second phase of particularly the top and bottom traces illustrates the difficulty in determining the SP phase onset.

| | Observed | | (absolute times are relative 14:24:00) | |
|------|-------------------|-------|--|----------------|
| | P [s] | S [s] | SP-P [s] | GAK2 P - P [s] |
| GAK2 | 1.04 | 1.77 | 0.73 | 0.00 |
| GAK3 | 2.26 | 3.06 | 0.80 | -1.22 |
| GAK4 | 1.52 | 2.24 | 0.72 | -0.48 |
| | HYPOSEARCH | | (absolute times are relative 0) | |
| | P [s] | S [s] | SP-P [s] | GAK2 P - P [s] |
| GAK2 | 3.76 | 4.39 | 0.63 | 0.00 |
| GAK3 | 4.92 | 5.68 | 0.76 | -1.16 |
| GAK4 | 4.05 | 4.92 | 0.87 | -0.29 |

Table 5.5: Observed onset times and travel times calculated with HYPOSEARCH.

Table 5.5 shows observed travel times for phases as picked in figure 5.7.3 and traveltimes for the best solution found by HYPOSEARCH.

Event 04-1400-02L (figure 5.7.4) occurred only a few minutes later, with a very similar signal shape, and also displaying the same onset difference as event 04-1400-01L. Although the solution for epicenter location do not match exactly, they could be related.

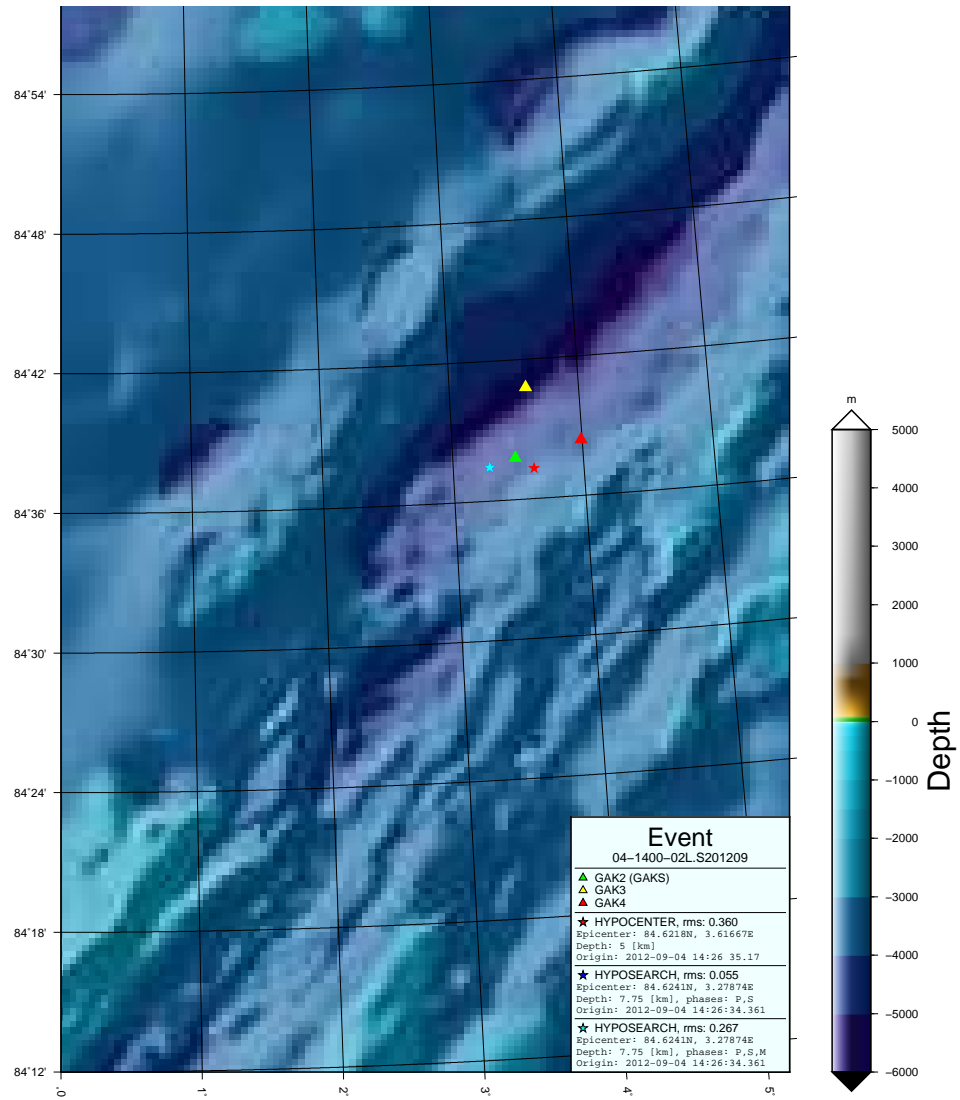


Figure 5.7.4: Location for event 04-1400-02L. The triangles show the station locations at the time of recording, the stars show the solutions for the same event using HYPOCENTER (red), HYPOSEARCH (only considering P and SP phase) (blue) and HYPOSEARCH (only considering P, SP and M phases) (cyan). The blue and cyan star (HYPOSEARCH solutions) coincide and only the cyan star is displayed.

5.7.3 Summary

Figure 5.7.6 and 5.7.5 shows all three located event plotted together above the IBCAO bathymetry.

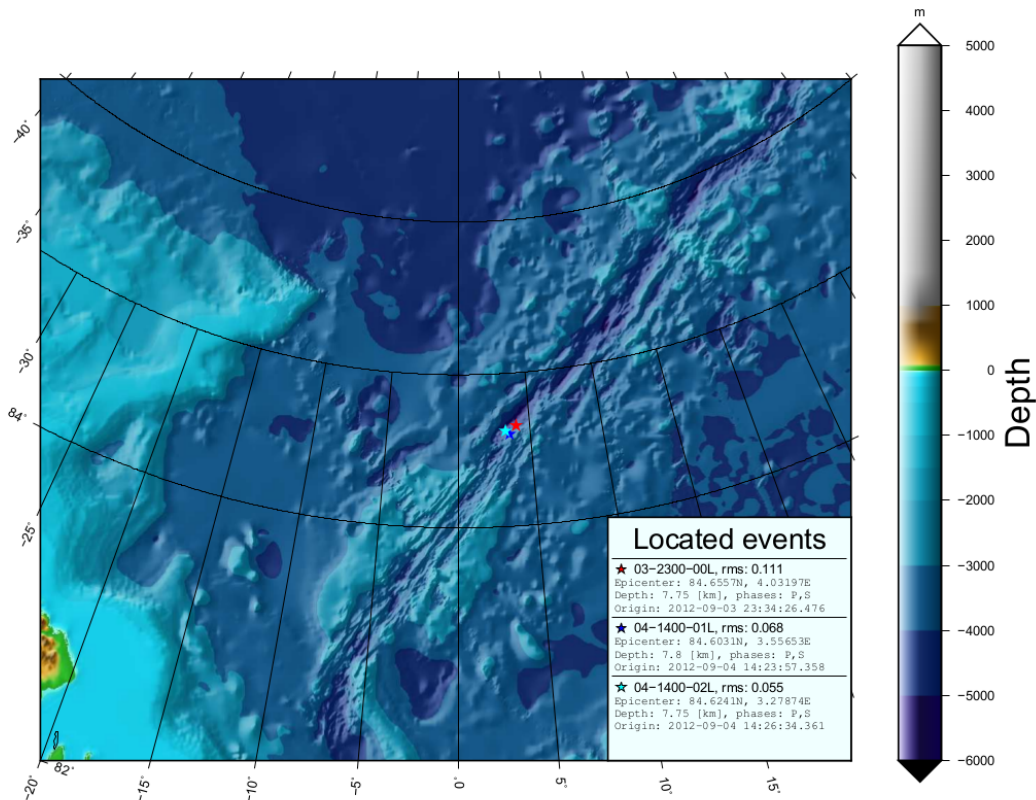


Figure 5.7.5: All three located events, different color signifies different event (regional map).

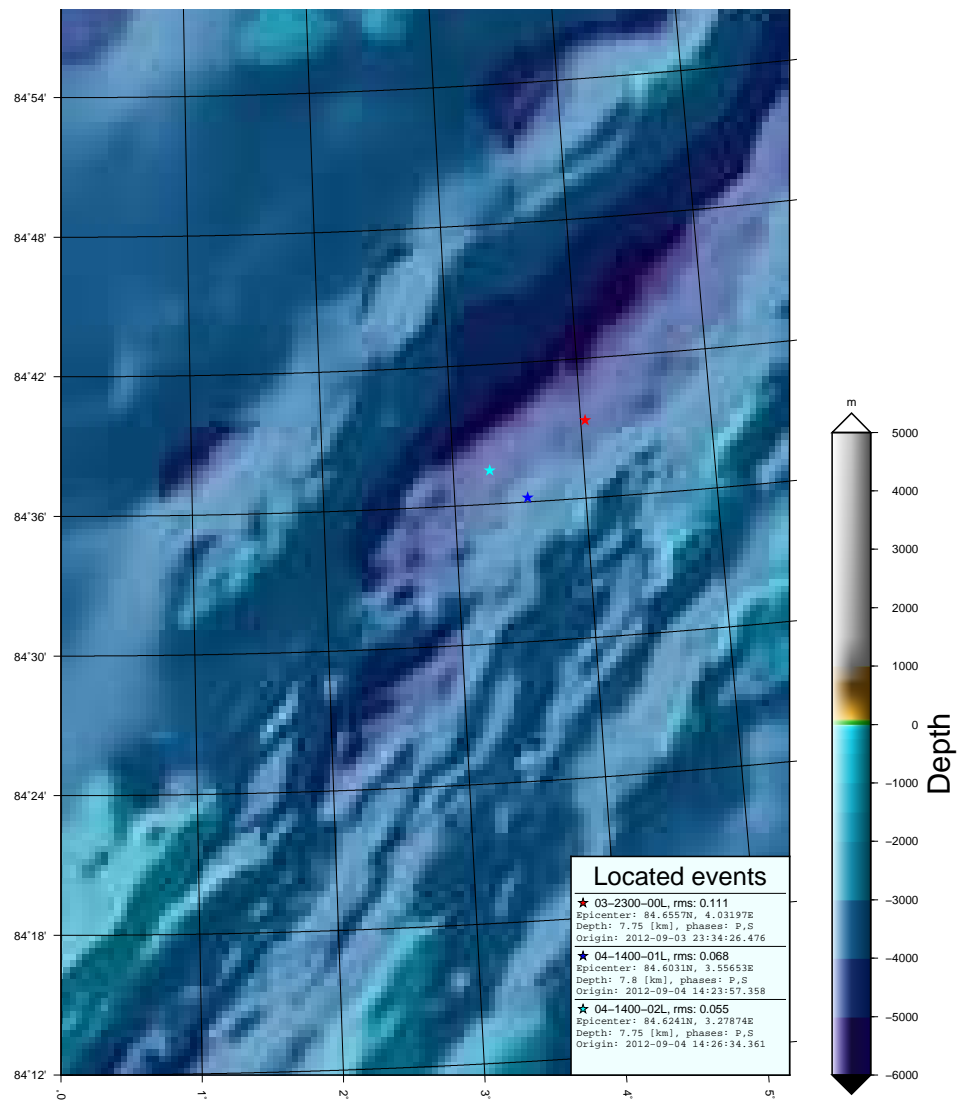


Figure 5.7.6: All three located events, different color signifies different event.

Chapter 6

Discussion and Conclusion

6.1 Evaluation of equipment and experiment

The seismic network developed as part of this thesis was deployed over the Gakkel Ridge for a total of 23 days. Two of the five original stations had permanent failures which became evident during the first deployment. During the following two deployments the network consisted of three stations in addition to one seismometer. Initial problems with the GPS connection and minor software issues were fixed during the first and second deployments.

Consequently, the last deployment of 7 days was the most successful with functional recording, positioning and timing for the duration of the deployment. The wireless network range was insufficient, but worked well on short range.

To aid in recovering the stations, the stations were marked with flags. Furthermore, since the hovercraft was drifting with the array, the pickup position of the stations could be estimated from the drift of the hovercraft with surprising efficiency. The longest drift distance between deployment and recovery was more than 80 km.

With a better wireless range, the problematic buoys would most likely have been discovered earlier during the first deployment, so that they could either have been fixed or replaced. However, due to limited fuel reserves for the hovercraft, neither of the stations that required travel could be serviced manually during each deployment.

The high frequency of the wireless network (2.4 GHz) was quickly attenuated and the

antenna range was sensitive to tilt because of a flat radiation pattern. If the wireless system is replaced with a lower frequency system, these issues should improve. A system that makes it possible to more easily adjust the antennas vertically and to mount them higher would also improve the radio range.

Quick and easy deployment is important because the weather often changes rapidly, and continuous southward drift requires longer travel. An efficient set-up was achieved, with set-up of a single station requiring only 15 minutes, and deployment of the entire network with side lengths of more than 5 km completed within 5 hours. Such efficiency in set-up is important, since time and fuel is very valuable in the Arctic, regardless of the logistical platform available.

To scale the experiment up with more stations over a larger area, the network must either be deployed further north, in order to obtain a greater time margin, or a more efficient deployment process (e.g. helicopter) must be used.

Once a station was connected to the battery, it started and worked reliably. The humidity, the wind and the repeated freezing and thawing presented no problems. A 12 V, 72 Ah car battery was sufficient to power a station during an entire deployment. Low power usage also simplifies setup and reduces the total weight of the station considerably.

The hydrophone based stations had no problems with failures caused by ice drift or melting ice surface. The seismometer that was placed next to the hovercraft had to be re-balanced periodically to avoid failures due to seismometer tilting from melting. Frequent temporary failures still occur between the re-balancing due to low-period horizontal ice drift changes. However, only on rare occasions did the vertical channel of the seismometer fail.

Data indicates that the hydrophone is less sensitive to cryogenic signals than the seismometer, while still maintaining a reasonable signal to noise ratio for seismic signals. To be able to determine a detection threshold better, more locations must be found for which magnitudes can be calculated.

By placing the hydrophone directly below the ice or just inside the ice, the periodic signal, most likely related to strumming (Makris & Dyer, 1986), was avoided.

The network was first deployed at $11^{\circ}E$ over the Gakkel Ridge, in an area where seismicity was expected and the prototype setup would be tested. Due to the extended time available, because of the circumstances around the expedition, and the generally southwestern ice

drift, the network could be re-deployed two times. The general drift direction caused a westwards movement of the network, eventually into an area above some of the deepest parts of the Gakkel Ridge, where very little or no seismicity had previously been recorded. Eventually, the last deployment in the western part of the sparsely magmatic zone proved to be the most successful.

6.2 Results from acquisition

The data was organized in a database as miniSEED files together with status and position files. Tools were developed to manipulate the database and events so that SEISAN could be used to organize the continuous data and event databases, to search for events, to discriminate between seismic events and unwanted noise and to pick phases. However, SEISAN is not made for working with a microseismic array that is continuously moving. In order to be able to process and analyze the events, a set of tools were developed to manipulate the data and correlate them with position and status.

By scanning through a set of pre-defined filters for 20 minute segments of the data, events were detected manually. The strongest signal to noise ratio was generally found in frequencies above 10 Hz. Only the strongest events had a high enough signal to noise ratio for the frequencies below 10 Hz. 41 events were identified for the last 7 days of deployment.

The events were discriminated from unwanted noise or signals by verifying that the event was present on all stations and that several phases could be detected in the signal. Additionally, the horizontal components of the seismometer was inspected. However, events that were present on all hydrophone stations seldom had stronger horizontal components on the seismometer. It was still useful to inspect the components, although it only served for discrimination purposes. The angle of incidence will be almost vertical for all phases because of the strong velocity contrast between water and seafloor, thus it can be expected that the horizontal components will be weak so that they badly constrain direction for real seismic events.

None of the strongest events located could be related to events in the earthquake catalogues for the stations on land (neither NNSN or NORSAR catalogues). These events were located close to the network and must be too weak to have been recorded on teleseismic distances,

and illustrates the importance of a microseismic survey to gain a better image of the earthquake distribution. If other events in the data set can be related to events detected telesismically, they can aid in determining the magnitude of the events.

Smaller (probably close) events were impulsive, with a short waveform, while other weak signals (possibly further away) showed an emergent T-phase and a less impulsive shape. This is related to the fact that as the distance and angle of incidence increase more of the energy will be trapped in the water column.

For presumably close events, that were strong enough, water multiples were identified. The strong topography of the Gakkel Ridge and the few numbers of stations make reliable identification of phases difficult, but identification of the SP converted phase was nonetheless attempted in order to be able to locate some of the events.

The seismometer and the adjacent hydrophone outputs show similar waveforms. It appears that the seismometer data is more sensitive to cryogenic noise, but that the hydrophone and seismometer have a similar detection level for the final catalogue of seismic events. Additionally, the effects of ice drift and tilt due to melting have riddled the seismometer data with failures and drifting signals. A more robust setup for this kind of study might consist of a shorter period geophone (1 Hz) as well as a hydrophone.

The ambient noise levels observed during the last deployment match those expected in the ice-covered Arctic.

A systematic timing difference between hydrophone data and seismometer data (where they were co-located) of about 0.1 seconds seems to be present (based on comparing onset for events). Although the timing algorithm is very simple and direct for the buoy and although the GPS unit reports full synchronization, this discrepancy with the well-tested Taurus digitizer is a serious concern. Accurate timing is imperative for any seismic station. However, given that the error seems to be fairly constant (for the buoy co-located with the seismometer station), it is reasonable to think that it is also relatively constant for the other stations.

When picking phases in SEISAN, the picks are, in default mode, not stored with greater accuracy than 0.01 seconds. Additionally, pick uncertainty further contributes to the error in the phase pick. Therefore, while the systematic timing error is a an important concern, the phase picks are still assumed to be usable for determining the location. Due to the

difficulty in pinpointing the SP phase it is not so useful to mitigate this absolute timing error by weighing travel time differences heavier while locating the event.

6.3 Location algorithm

Despite uncertainties in the velocity structure (Schlindwein *et al.*, 2007; Jokat & Schmidt-Aursch, 2007), which is very poorly constrained, and the difficulty in correctly identifying and pinpointing the phases at each station, location of three events by the use of a location algorithm was attempted.

The rough topography of the Gakkel Ridge greatly influences the ray paths and arrival times, so that, especially for the nearby events, the use of traditional 1D iterative algorithms is not optimal. It was therefore necessary to develop a new 3D routine, which takes the bathymetry into account and defines the velocity structure as a layered model. With the new 3D routine, the delayed onset time of the first arrival could be predicted, while the SP-P difference remained similar between the stations due to the difference in bathymetry.

The difference in water depth of around 1000 meters between the location of the stations, and near vertical ray paths, caused a delay dependent on depth. However, the SP-P difference no longer changed significantly because the S phase was converted to P at the seafloor and the ray paths are similar.

The algorithm calculates the ray paths for a grid and searches for the best match. Since the stations are continuously moving, the ray paths could not be pre-computed as is sometimes done in similar existing algorithms.

The routine calculated the ray paths and travel times for the water multiples in order to be able to take them into account. However, because of the rough bathymetry, ray behavior is complex and it is difficult to find a complete coverage of solutions for the entire grid. In addition, due to the bathymetry, the ray paths scatter wildly. Ultimately, the constraints gained from the multiples were not very useful, since the travel time was mostly dependent upon the water depth and the ray path on the bathymetry below the station, rather than upon the location of the earthquake.

Correctly identifying the phases is the first step to obtaining an accurate location of the earthquakes. Picking of the converted S to P phase could only be attempted for the suf-

ficiently clear events, and it is still uncertain whether this is indeed the correct phase and whether the actual onset was successfully pinpointed. When visible, to aid in constraining the epicenter, the water multiples of the first arrival were picked.

Three of the clear events have been located using the routine developed as part of this thesis, HYPOSEARCH, as well as with the existing HYPOCENTER. Since the calculated ray coverage is most extensive for the direct phases (P and SP), the location calculated by using only these direct phases (P and SP) for each station appears to be the most trustworthy. Error estimates are hard to quantify since so many unknown factors contribute to the total uncertainty. More stations would assist in estimating the error and increase accuracy, since in this experiment, the discovery of failure in two of the initially deployed stations means the number of stations are at the minimum and the number of phase observations is almost at the minimum needed to calculate a location. As expected the locations found by the different routines do not exactly match, but are similar.

The preference of a location solution below the network when using the water multiples with the HYPOSEARCH routine can be explained by the difficulty in calculating a sufficient ray coverage for larger take off angles. Without rays between the stations and grid cells there will not be a candidate for the grid search to compare with.

For more distant events, an existing, iterative algorithm would be more practical, since the topography contributes less to the total traveltimes. A distant event would require a lot of grid cells and the HYPOSEARCH routine would be too computationally intensive to be practical. In a border case, an initial solution can be sought by an iterative algorithm, then used to constrain the search region before our routine could be applied on this region.

6.4 Interpretation of event locations

The events have been located to the south flank of the westernmost segment of the sparsely magmatic zone on the Gakkel Ridge. The segment is amagmatic (Michael *et al.*, 2003) and has an asymmetrical topography (Cochran, 2008). Escartín *et al.* (2008) suggests that these amagmatic and asymmetrical properties are associated with an accretion mode involving a major detachment fault (Figure 6.4.1). Since no basalt has been recovered from this segment (Michael *et al.*, 2003), the events are likely to be of a tectonic, and not volcanic, origin.

With only three events it is not possible to infer the parameters of the ongoing processes. However, in this mode of accretion it can be suggested that they are likely to be related to either the detachment fault or a fault block from the opposing flank. Whatever the configuration of the detachment fault, an asymmetrical distribution of earthquakes across axis would be expected.

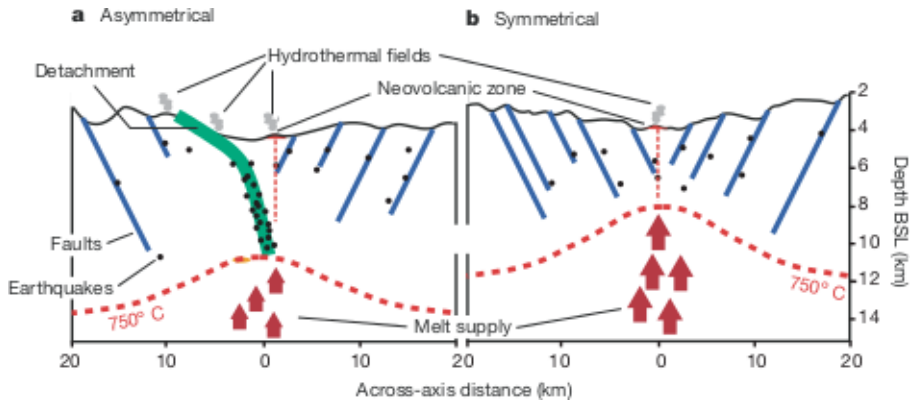


Figure 6.4.1: Cross section of spreading ridge for a) an asymmetrical case and b) a symmetrical case (figure from Escartín *et al.*, 2008).

Schlindwein *et al.* (2007) has previously noted a slight tendency to asymmetrical distribution with a preference for the north flank of earthquakes further east, between $15^{\circ} E$ and $19^{\circ} E$. These earthquakes have also been related to tectonic faulting.

The deployment was short term and as such could not give anything more than a glimpse of the ongoing processes. A cumulative longer monitoring time of the seismicity is required, but this was also the case for the previous deployments by Schlindwein *et al.* (2007); long term deployments are difficult to achieve in the Arctic.

If the remaining collected events can be located with some accuracy they can contribute to determining the distribution of earthquakes for this segment.

6.5 Conclusion

The perennial sea ice cover and inaccessibility of the Arctic Ocean required seeking out new approaches to enable one to perform a study of the microseismicity of the Gakkel

Ridge. Kristoffersen *et al.* (1982) and Schlindwein *et al.* (2007) have used hydrophone and seismometer based stations respectively to monitor the seismicity from the drifting sea ice. The goal of this project was a further development of these approaches: a network of stations was built and deployed above the Gakkel Ridge, the recorded data was analyzed and a 3D location algorithm was developed, with which three of the events were located. The conclusions from the deployment and data analysis are:

- Five buoys were made, of these three were undamaged and working throughout the experiment. Initial problems with the GPS unit were solved for the last deployment. The wireless network range was insufficient to span the deployed network, but the communication worked well on a short range.
- The network and seismic stations recorded microseismicity for a total of 23 days, of which the last 7 days were the most successful.
- The network was easy and quick to deploy. Neither humidity, repeated freezing and thawing nor wind presented any problems for the equipment.
- The last and most successful deployment of 7 days was subjected to further analysis. The network drifted above the western part of the sparsely magmatic zone and one of the deepest parts of the Gakkel Ridge. From the data on this segment, 41 events were identified as likely seismic events. Ambient noise levels matched expected levels.
- To locate the events, the rough bathymetry of the Gakkel Ridge had to be taken into account, thus a routine using a simplified 3D model was developed to account for the bathymetry. With this routine, three events were located to the south flank of the Gakkel Ridge. This routine was able to model the observed traveltimes as they were affected by the bathymetry. However, the largely unknown velocity structure below the Gakkel Ridge and the difficulties in determining the exact phase onsets contribute to considerable uncertainties in the locations.
- The prototype network is a viable approach, but several issues must be solved. A station using a hydrophone and a geophone may be the most robust setup. Additionally, a larger network with more stations will improve location accuracy. A longer monitoring time is required, but long, uninterrupted sessions are difficult to achieve in the

Arctic conditions. Therefore, an updated version of the station, with the main issues solved, would be a good alternative for this kind of experiment.

- Three located events are insufficient to implicate the ongoing processes, but together with more locations from this experiment and further monitoring they can contribute to determining the distribution of seismicity in this area, and thus the understanding of the processes of the Gakkel Ridge.

6.6 Further work

The goal of this project was the further development of the methods for studying the microseismicity of the Gakkel Ridge. Therefore, the focus of this project has been to take the approach from concept, through development, building, data acquisition and then to explore the potential of the acquired data. In this way the entire method could be evaluated and a glimpse could be caught of the ongoing processes of the Gakkel Ridge. In this section steps to further complement this work and to improve the method are suggested.

Now that the concept and method have been tested, the next steps would be to search the complete, existing, data set for events, and locate as many events as possible. Then, a more comprehensive study of the data quality, as well as more extensive testing of the equipment would be useful to rigorously establish the method as a trustworthy source, and to determine what improvements should be made to the equipment.

For further development of the method, the experiences gained in the prototype deployment must be taken into account. For the equipment these include solving the timing issues, extending the network range and improve the mechanical robustness of the buoy.

Additionally, improvements could include adding a geophone as well as the hydrophone to each station so that events can be better discriminated. The method would also benefit from deploying a larger network with more stations, as this would significantly increase the accuracy of earthquake location and increase detection sensitivity.

Several steps can be taken to further develop the location algorithm, including optimizations made in order to improve ray coverage, ray parameter interpolation and initial guesses so that the algorithm can be run more automatically on arbitrary events.

To determine the distribution and characteristics of the seismicity of the Gakkel Ridge, more monitoring must be done. With a longer cumulative monitoring time, the recorded seismicity can be used to infer the properties of ongoing processes.

The challenge of making longer term, uninterrupted, deployments still remains.

Bibliography

- AKI, K., & RICHARDS, P. 1980. *Quantitative seismology*. Freeman San Francisco.
- BEYREUTHER, M., BARSCH, R., KRISCHER, L., MEGIES, T., BEHR, Y., & WASSERMANN, J. 2010. ObsPy: A Python Toolbox for Seismology. *Seismological Research Letters*, **81**(3), 530–533.
- BURR-BROWN. 1989. *OPA627 - Precision High-Speed Difet; Operational Amplifiers*. Texas Instruments.
- BURR-BROWN. 1993. *OPA633 - High Speed Buffer Amplifier*. Texas Instruments.
- BURR-BROWN. 1996. *BUF634 - 250mA High-Speed Buffer*. Texas Instruments.
- CERVENY, V. 2005. *Seismic Ray Theory*. Cambridge University Press.
- COCHRAN, J. R. 2008. Seamount volcanism along the Gakkel Ridge, Arctic Ocean. *Geophysical Journal International*, **174**(3), 1153–1173.
- CROTWELL, H. P., & OWENS, T. J. 1999. *The TauP Toolkit: Flexible Seismic Travel-Time and Raypath Utilities*.
- DE BERG, M., CHEONG, O., VAN KREVELD, M., & OVERMARS, M. 2008. Delaunay Triangulations. Pages 191–218 of: *Computational Geometry: Algorithms and Applications*, 3 edn. Springer-Verlag.
- DE GREVE, B. 2006. *Reflections and Refractions in Ray Tracing*. URL http://users.skynet.be/bdegreve/writings/reflection_transmission.pdf (accessed 2013-05-30).

- DEMETS, C., GORDON, R. G., & ARGUS, D. F. 2010. Geologically current plate motions. *Geophysical Journal International*, **181**(1), 1–80.
- DICK, H. J. B., LIN, J., & SCHOUTEN, H. 2003. An ultraslow-spreading class of ocean ridge. *Nature*, **426**(6965), 405–12.
- DIETZ, R. S., & SHUMWAY, G. 1961. Arctic Basin Geomorphology. *Geological Society of America Bulletin*, **72**(September 1964), 1319–1330.
- DZIAK, R., BOHNENSTIEHL, D., & SMITH, D. 2012. Hydroacoustic monitoring of oceanic spreading centers: Past, present, and future. *Oceanography*, **25**(1), 116–127.
- EDWARDS, M. H., & COAKLEY, B. J. 2003. SCICEX Investigations of the Arctic Ocean System. *Chemie der Erde - Geochemistry*, **63**(4), 281–328.
- EDWARDS, M. H., KURRAS, G. J., TOLSTOY, M., BOHNENSTIEHL, D. R., COAKLEY, B. J., & COCHRAN, J. R. 2001. Evidence of recent volcanic activity on the ultraslow-spreading Gakkel Ridge. *Nature*, **409**(February).
- ELMENDORF, C. H., & HEEZEN, B. C. 1957. Oceanographic Information for Engineering Submarine Cable Systems. *The Bell System Technical Journal*, **XXXVI**(5).
- ENGDAHL, E. R., VAN DER HILST, R., & BULAND, R. 1998. Global teleseismic earthquake relocation with improved travel times and procedures for depth determination. *Bulletin of the Seismological Society of America*, **88**(3), 722–743.
- ENGEN, O. Y., & ELDHOLM, O. 2003. The Arctic plate boundary. *Journal of Geophysical Research*, **108**(B2).
- ESCARTÍN, J., SMITH, D. K., CANN, J., SCHOUTEN, H., LANGMUIR, C. H., & ESCRIG, S. 2008. Central role of detachment faults in accretion of slow-spreading oceanic lithosphere. *Nature*, **455**(7214), 790–4.
- EVJENTH, D. 2000. *Veien blir til mens du går deg vill*. Schipsted.
- FEDEN, R., VOGT, P., & FLEMING, H. 1979. Magnetic and bathymetric evidence for the “Yermak hot spot” northwest of Svalbard in the Arctic Basin. *Earth and Planetary Science Letters*, **44**(1979), 18–38.

- GLOBALSAT. 2012. *Product User Manual GPS Receiver Engine Board EM-406A*.
- GREIMAN, W. 2013. *Arduino SdFat library (sdafatlib)*. URL <http://code.google.com/p/sdfatlib/> (accessed 2013-05-28).
- HEEZEN, B. C., & EWING, M. 1961. The Mid-Oceanic Ridge and its extension through the Arctic Basin. *Pages 622–642 of:* RAASCH, G. (ed), *Geology of the Arctic*. Univ. of Toronto Press.
- JAKOBSSON, M., MAYER, L., COAKLEY, B., DOWDESWELL, J. A., FORBES, S., FRIDMAN, B., HODNESDAL, H., NOORMETS, R., PEDERSEN, R., REBESCO, M., SCHENKE, H. W., ZARAYSKAYA, Y., ACCETTELLA, D., ARMSTRONG, A., ANDERSON, R. M., BIENHOFF, P., CAMERLENGHI, A., CHURCH, I., EDWARDS, M., GARDNER, J. V., HALL, J. K., HELL, B., HESTVIK, O., KRISTOFFERSEN, Y., MARCUSSEN, C., MOHAMMAD, R., MOSHER, D., NGHIEM, S. V., PEDROSA, M. T., TRAVAGLINI, P. G., & WEATHERALL, P. 2012. The International Bathymetric Chart of the Arctic Ocean (IBCAO) Version 3.0. *Geophysical Research Letters*, **39**(12).
- JOHNSON, G., & ECKHOFF, O. B. 1966. Bathymetry of the north Greenland Sea. *Deep Sea Research and Oceanographic Abstracts*, **13**(6), 1161–1173.
- JOHNSON, G., GRANTZ, A., & WEBER, J. 1990. Bathymetry and morphology of the Arctic Ocean. *Chap. Bathymetry, pages 63–78 of:* GRANTZ, A., JOHNSON, G., & SWEENEY, J. F. (eds), *The Arctic Ocean Region*. Boulder, Colorado: Geological Society of America.
- JOKAT, W., & SCHMIDT-AURSCH, M. C. 2007. Geophysical characteristics of the ultra-slow spreading Gakkel Ridge, Arctic Ocean. *Geophysical Journal International*, **168**(3), 983–998.
- JOKAT, W., WEIGELT, E., KRISTOFFERSEN, Y., RASMUSSEN, T., & SCHÖNE, T. 1995. New geophysical results from the south-western Eurasian Basin (Morris Jesup Rise, Gakkel Ridge, Yermak Plateau) and the Fram Strait. *Geophysical Journal International*, 601–610.
- JOKAT, W., RITZMANN, O., SCHMIDT-AURSCH, M. C., DRACHEV, S., GAUGER, S., & SNOW, J. 2003. Geophysical evidence for reduced melt production on the Arctic ultraslow Gakkel mid-ocean ridge. *Nature*, **423**(6943), 962–5.

- KEENAN, R. E., & DYER, I. 1984. Noise from Arctic Ocean earthquakes. *Acoustical Society of America*, **75**(May 2013), 819–825.
- KEERS, H., DAHLEN, F. A., & NOLET, G. 1997. Chaotic ray behaviour in regional seismology. *Geophysical Journal International*, **131**(2), 361–380.
- KLINCK, H., NIEUKIRK, S. L., MELLINGER, D. K., KLINCK, K., MATSUMOTO, H., & DZIAK, R. P. 2012. Seasonal presence of cetaceans and ambient noise levels in polar waters of the North Atlantic. *The Journal of the Acoustical Society of America*, **132**(3), EL176–81.
- KRISTOFFERSEN, Y. 2011. Chapter 45 Geophysical exploration of the Arctic Ocean: the physical environment, survey techniques and brief summary of knowledge. *Geological Society, London, Memoirs*, **35**(1), 685–702.
- KRISTOFFERSEN, Y., HUSEBYE, E., BUNGUM, H., & GREGERSEN, S. 1982. Seismic investigations of the Nansen Ridge during the FRAM I experiment. *Tectonophysics*, **82**, 57–68.
- KUTSCHALE, H. 1961. Long-Range Sound Transmission in the Arctic Ocean. *ARCTIC*, **66**(7).
- LÄDERACH, C., & SCHLINDWEIN, V. 2011. Seismic Arrays on Drifting Ice Floes: Experiences from Four Deployments in the Arctic Ocean. *Seismological Research Letters*, **82**(4), 494–503.
- LEAFLABS. 2012. *Leaflabs Libmaple manual*.
- MAKRIS, N. C., & DYER, I. 1986. Environmental correlates of pack ice noise. *Acoustical Society of America*, 1434–1440.
- MICHAEL, P. J., LANGMUIR, C. H., DICK, H. J. B., SNOW, J. E., GOLDSTEIN, S. L., GRAHAM, D. W., LEHNERT, K., KURRAS, G., JOKAT, W., MÜHE, R., & EDMONDS, H. N. 2003. Magmatic and amagmatic seafloor generation at the ultraslow-spreading Gakkel ridge, Arctic Ocean. *Nature*, **423**(6943), 956–61.
- MÖLLER, T., & TRUMBORE, B. 1997. *Fast, Minimum Storage Ray/Triangle Intersection*. URL <http://www.graphics.cornell.edu/pubs/1997/MT97.pdf> (accessed 2013-05-30).

- MÜLLER, C., & JOKAT, W. 2000. Seismic evidence for volcanic activity discovered in central Arctic. *Eos, Transactions American Geophysical Union*, **81**(24), 265.
- NARYSHKIN, G. 1987. Middle ridge of the Eurasia Basin of the Arctic Ocean. Translated from Sredinney Khrebet Yevraziyskogo Basseyna Severnogo Ledovitogo Okeana. Translated by Translation Division, Foreign Technology Division, WPAFB, Ohio. *Nauka Publishing House*, 1–71.
- OBSIP. 2013. *OBSIP - The Ocean Bottom Seismograph Instrument Pool*. URL <http://www.obsip.org/instruments/long-period/> (accessed 2013-05-30).
- OLMEXINO LTD. 2011. *Olimexino STM32 H103 development board - Users manual*.
- OTTEMÖLLER, L., VOSS, P., & HAVSKOV, J. 2011. *Seisan earthquake analysis software for Windows, Solaris, Linux and Mac OS X, Version 9.0.1*.
- OYE, V., & ROTH, M. 2003. Automated seismic event location for hydrocarbon reservoirs. *Computers & Geosciences*, **29**(7), 851–863.
- PARKINSON, C. L., & COMISO, J. C. 2013. On the 2012 Record Low Arctic Sea Ice Cover: Combined Impact of Preconditioning and an August Storm. *Geophysical Research Letters*, **40**(April).
- PUJOL, J. 2003. *Elastic wave propagation and generation in seismology*. Cambridge University Press.
- SCHLINDWEIN, V., MÜLLER, C., & JOKAT, W. 2007. Microseismicity of the ultraslow-spreading Gakkel ridge, Arctic Ocean: a pilot study. *Geophysical Journal International*, **169**(1), 100–112.
- SCHWEITZER, J. 2001. HYPOSAT – An Enhanced Routine to Locate Seismic Events. *Pure and Applied Geophysics*, **158**(1), 277–289.
- SHEARER, P. M. 2009. *Introduction to Seismology*. 2nd edn. Cambridge University Press.
- STMICROELECTRONICS. 2012. *STM32F10RBT6 Datasheet Rev. 3*.
- SYKES, L. 1965. The seismicity of the Arctic. *Bulletin of the Seismological Society of America*, **55**(2), 519–536.

- SYNAPSE WIRELESS. 2011. *Synapse RF Engine 200 Series*.
- TELEDYNE BENTHOS. 2012a. *AQ-18 suggested decoupling (unpublished)*.
- TELEDYNE BENTHOS. 2012b. *Benthos Hydrophones Brochure*. URL <http://www.benthos.com/index.php/product/hydrophones/aq-18-molded-hydrophone> (accessed 2013-05-30).
- TELEDYNE BENTHOS. 2012c. *Plot of frequency response for AQ-18, communications with Benthos by email (1. nov 2012)*.
- TEXAS INSTRUMENTS. 2002. *Fully Differential Amplifiers*.
- TEXAS INSTRUMENTS. 2007. *ADS1282 - High Resolution Analog-to-Digital Converter*.
- TEXAS INSTRUMENTS. 2009. *ADS1282EVM and ADS1282EVM-PDK User's Guide*.
- TEXAS INSTRUMENTS. 2010. *OPA1632 - High-Performance, Fully-Differential Audio Operational Amplifier*.
- TOLSTOY, M., BOHNENSTIEHL, D., EDWARDS, M., & KURRAS, G. 2001. Seismic character of volcanic activity at the ultraslow-spreading Gakkel Ridge. *Geology*, **29**(12), 1139.
- TRABANT, C. 2012. *Libmseed manual and source code*. Version 2. edn. IRIS Data Management Center.
- TREBBIN, N. 2010. *Seismic Data Analysis with ObsPy*. BSc, Ludwig-Maximilians-University Munich.
- TUSZYNSKI, J. 2011. *Triangle / Ray intersection*. URL <http://www.mathworks.com/matlabcentral/fileexchange/33073-triangleray-intersection> (accessed 2013-04-22).
- VOGT, P. R., TAYLOR, P. T., KOVACS, L. C., & JOHNSON, G. L. 1979. Detailed aeromagnetic investigation of the Arctic Basin. *Journal of Geophysical Research*, **84**(B3), 1071.
- VREELAND, J. 2013. *Maple SdFat library*. URL <http://code.google.com/p/maple-sdfat/> (accessed 2013-05-28).

Appendices

Appendix A

The Buoy and Network - Concept and Specification

This chapter describes the technical specifications and the implementation of the buoys and the network.

A.1 Overview

System A hydrophone was chosen to measure the acoustic pressure. The hydrophone was let through a hole drilled in the ice and leveled just below the ice. A seismometer with a standard commercial digitizer was placed at one of the stations. Five stations were built. A digitizer based on a small main board was connected to a GPS for positioning and timing, wireless radio (RF) for communication with the central logging base, a SD card for local storage and an analog interface to the hydrophone. The entire setup should be simple and robust since deployment time always will be a limit. Operation must require no manual interaction and even without any working network communication recording, timing and positioning should be fully functional.

Network The prototype network consisted of five stations deployed in a triangle or rectangle configuration of side lengths up to above 5.5 km. Exact array geometry and station

placement would be strongly limited by ice conditions and should avoid broken up ice, fissures and cracks for keeping ice induced noise minimal. An area with larger ice floes (diameter above 2-3 km) with normally flatter ice was chosen, as maintaining geometry and deploying and recovering the stations would be easier. A diagram of the network setup is shown in figure 3.2.1.

Power Power was supplied by a regular car battery (72 Ah) and it should be sufficient for more than two weeks of continuous operation.

Operating system The main board with an operating system with drivers for the devices was carefully programmed to fit the program on the boards limited flash memory and RAM. Data processing, recording and storage must run fast to fit all in the limited buffer and to be able to communicate with the central logging point at the same time.

Wireless communication A network protocol was implemented on top of the built-in mesh network of the wireless radio (RF) unit allowing remote control, data transmission and status messages to be sent back to the central logging point. A local server was running on a regular laptop connected to a wireless radio unit receiving status and data from the stations, allowing position and status to be transmitted as well as near real time data transmission for monitoring the recorded signal on all stations.

A.1.1 Prototype and Goals

A.1.1.1 Prototype

The experiment and equipment must be considered to be in a prototype state.

A.1.1.2 Goals

The network and buoy goals are a system:

- Sufficiently sensitive and good signal quality

- Robust and stable
- Quality of data and storage
- Based on one hydrophone as sensor and a seismometer at one of the stations
- Continuous, independent and accurate enough timing and positioning to be able to locate recorded events
- Continuous up-time of more than 14 days on a car battery
- A fully specified and sound instrument response
- Easy and quick to deploy
- A complete system
- Communication to transmit position, status and data back to logging point
- Local storage of data - full functionality for an isolated buoy
- A system that could be modified and repaired during the experiment and for future experiments
- Simple in design and use - but complex enough to solve the task

A.2 Specification

The ready assembled buoy can be seen in figure 3.3.1 with the main board with the central processing unit, the input terminals and cable throughputs, the radio unit, the GPS unit, the AD converter and the buffer and decoupling stage which is the analog interface connected to the hydrophone, sampling at 250 Hz.

A.2.1 Analog components

Figure A.2.1 shows the wiring diagram for the buoy.

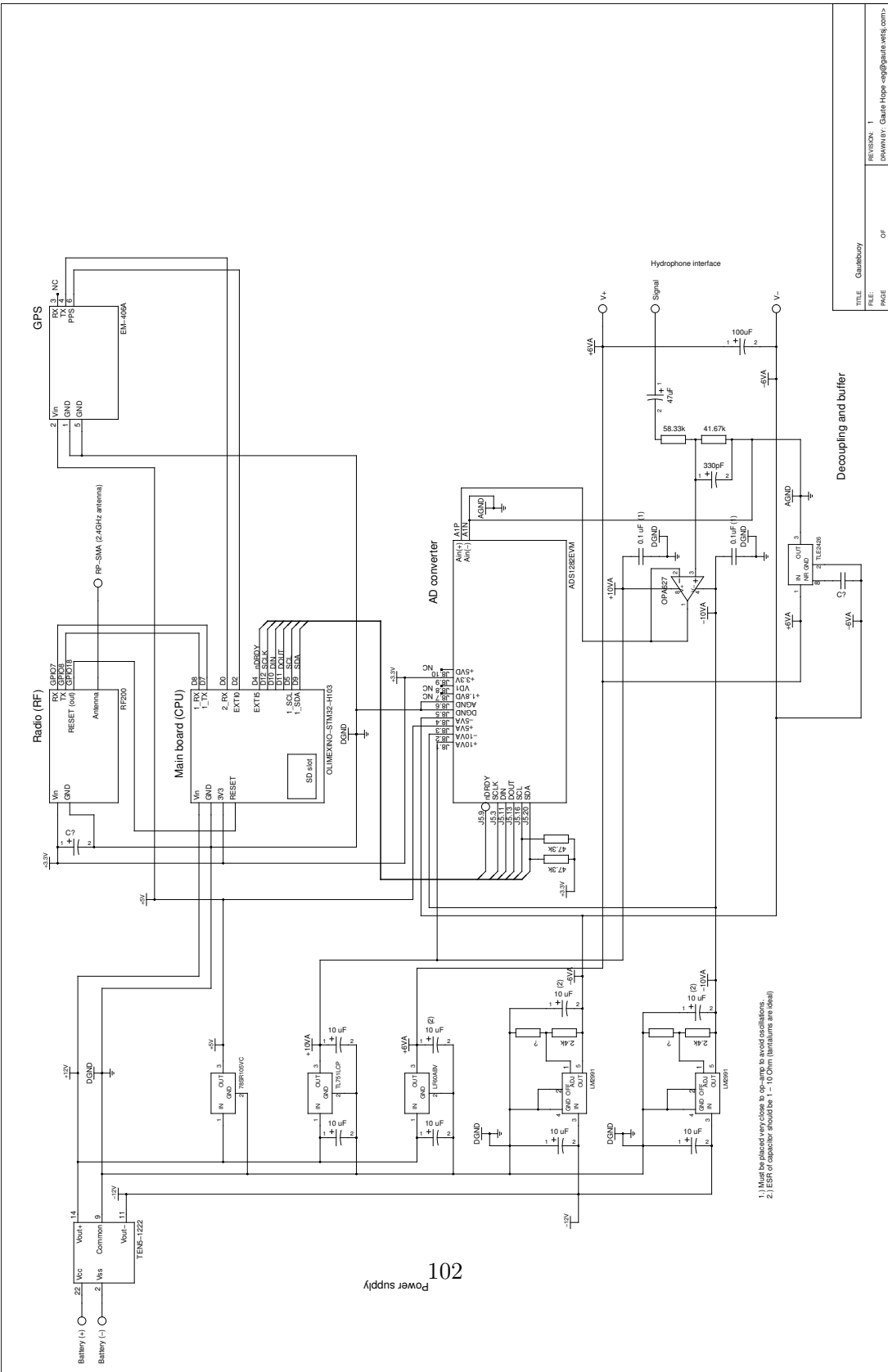


Figure A.2.1: Complete wiring diagram for buoy, component symbols have only relevant pins drawn.

The analog parts of the buoy consisted of the power supply and the interface to the hydrophone and parts of the analog to digital converter. The power supply had to be designed to minimize noise and to separate digital and analog systems as much as possible. As far as practically feasible this separation should avoid noise from digital communication and power surges to affect the analog signal. Although we could not hope to achieve the levels of noise free signal of a professionally built system, some techniques could be used. Under the assumption that the buoy will be powered from a quiet power source like a battery and that there will be no AC powered equipment nearby to create interference we can reach a reasonably good signal to noise ratio, above that generated by the (relatively high) ambient noise.

A.2.1.1 Power supply

The buoy accepted an input voltage range from 9 V to 36 V DC. The input should be from a quiet source, e.g. a battery. Converted AC, or nearby AC power sources, would result in noise from the power source to propagate onto the analog signal. In a lab with a lot of equipment a strong 50 Hz component could be seen on the recorded signal - even when the buoy is powered by a battery, this was ignored since there would be no problematic sources of electromagnetic noise in the field.

As can be seen in figure A.2.1 the initial DC/DC, switched regulator, outputs $\pm 12V$ as well as a common ground D_{GND} , there were additionally 6 different voltage levels required: $\pm 10V$, $\pm 6V$, $+5V$, $+3.3V$. The CPU board was powered by the $12V$ and provides $3.3V$, switched, regulated output. The GPS was powered by $5V$, the radio (RF) by $3.3V$, the ADS1282EVM required $\pm 10V$, $\pm 5V$ (where $+5V$ and $-6V$ suffices) and $3.3V$. The decoupling and buffer required $\pm 6V$ and a separate balanced ground was provided for analog ground to avoid digital noise to propagate onto the analog signal. By powering all analog parts of the buoy through low drop-out regulators (LDO), with correctly chosen bypass capacitors, noise on the power line and from the regulators could to a large degree be isolated. The analog-digital converter, ADS1282EVM (Texas Instruments, 2009), was internally regulated and the switched voltage (as well as the switched ground, D_{GND}), which can have a high amount of ripple and noise, was regulated through internal LDOs before being used. This means that switched regulators, with the advantage of very high power-efficiency regulation, were used for digital parts where they do not affect the analog signal. Low drop out

regulators, which are slightly less efficient, but very quiet, were used on the analog system without allowing digital noise and only powering the components that need low-noise power. The total consumption is then 210 mA at 12 V, or 2.52 W, for a fully operating buoy transmitting recorded data back to the central at full speed. For comparison a Nanometrics digitizer uses about 4W in normal mode (note that GPS position needs to be updated continuously).

Power budget With a regular 72 Ah, 12 V, battery the following power budget could be made:

| | | | |
|---------------------------|-------|-------|--|
| Buoy usage (@ 12 V) | 210 | mA | Based on measurements from a 12V DC source in lab under full operation |
| Hourly usage | 210 | mAh | |
| Daily usage | 5040 | mAh | |
| Power usage | 2520 | mW | |
| | | | |
| Battery capacity | 72 | Ah | |
| Maximum duration | 14.3 | days | |
| | 342 | hours | |
| | | | |
| Goal duration | 14 | days | Input can be as low as 9V and as high as 36V. |
| | 336 | hours | |
| Required battery capacity | 70.56 | Ah | |

Table A.1: Power budget

As can be seen from table A.1 a 72 Ah battery was sufficient for more than the targeted 14 days of operation, but in the field with temperatures around and below 0° C the capacity might decline. But with the buoy accepting input as low as 9 V it should still be powered by an almost discharged battery (in which case the voltage would fall and the current drain would increase) and use full capacity of the battery.

A.2.1.2 Buffer and decoupling

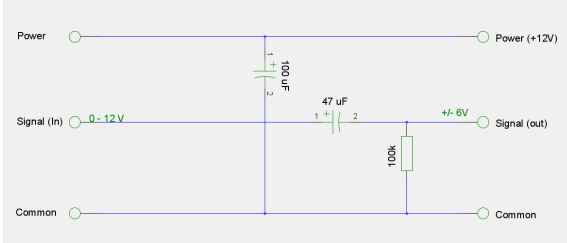


Figure A.2.2: Suggested decoupling for hydrophone (AQ-18) (Teledyne Benthos, 2012a).

Decoupling was based on the suggested decoupling wiring by Benthos (Teledyne Benthos, 2012a) as can be seen in figure A.2.2. The decoupling was modified so that it centers on A_{GND} , or +6V, referenced to common ground for the hydrophone, so that the signal could be scaled down to $A_{GND} \pm 2.5V$ before being fed to the ADS1282EVM inputs.

The ADS1282EVM first passed the signal through an operational amplifier (op-amp) with 100kΩ in parallel over the input terminals (Texas Instruments, 2009).

To scale the signal to a suitable level for the ADS1282EVM and preserve the suggested input impedance, the hydrophone signal was decoupled as suggested, but terminated at A_{GND} . The signal was divided with high precision resistors with an equivalent resistance of the suggested 100kΩ (a 330μF capacitor did initial low pass filtering). The output of the decoupling stage was fed through a buffer operational amplifier which provided high impedance and did not draw any significant current from the hydrophone (Figure A.2.1 shows the final buffer and decoupling wiring, while section A.2.2 analyzes the signal path and frequency response in detail).

The buffer op-amp easily drove the 100kΩ load of the ADS1282EVM (OPA627 Burr-Brown, 1989). The 100μF capacitor stabilized power supply and the 47μF capacitor decoupled the hydrophone and high pass filters out erroneous and potentially damaging DC drift.

A.2.1.3 Analog to digital converter

An ADS1282EVM (Texas Instruments, 2009) prototype board was used for analog to digital conversion. It was based on the delta-sigma ADS1282 (Texas Instruments, 2007) and was

an AD converter suitable for recording seismic signals and supports sampling frequencies from 250 Hz to 4 kHz. It had a theoretical maximum dynamic range of 130 dB with 250 Hz sample rate at full power mode¹. The ADS1282 was configured to sample at 250 Hz.

A.2.1.4 Hydrophone

A Benthos AQ-18(Teledyne Benthos, 2012b) hydrophone was used. The hydrophone was specified to have a flat frequency band (± 1.5 dB) from 1 Hz to 10 kHz (Teledyne Benthos, 2012b).

A.2.1.5 Antenna

Each station was equipped with an 15 dB(isotropic) omni-directional antenna of about 1,5 m length. The antenna was connected to the RF200 with a 1 m N-connector to RP-SMA connector cable. The central logging point had an 1W amplifier connected to an identical antenna mounted on top of the hovercraft. There was no amplifier for the wireless network on the stations because of power limitations.

¹Table 1, p. 13, (Texas Instruments, 2007)

A.2.2 Instrument response and analog analysis

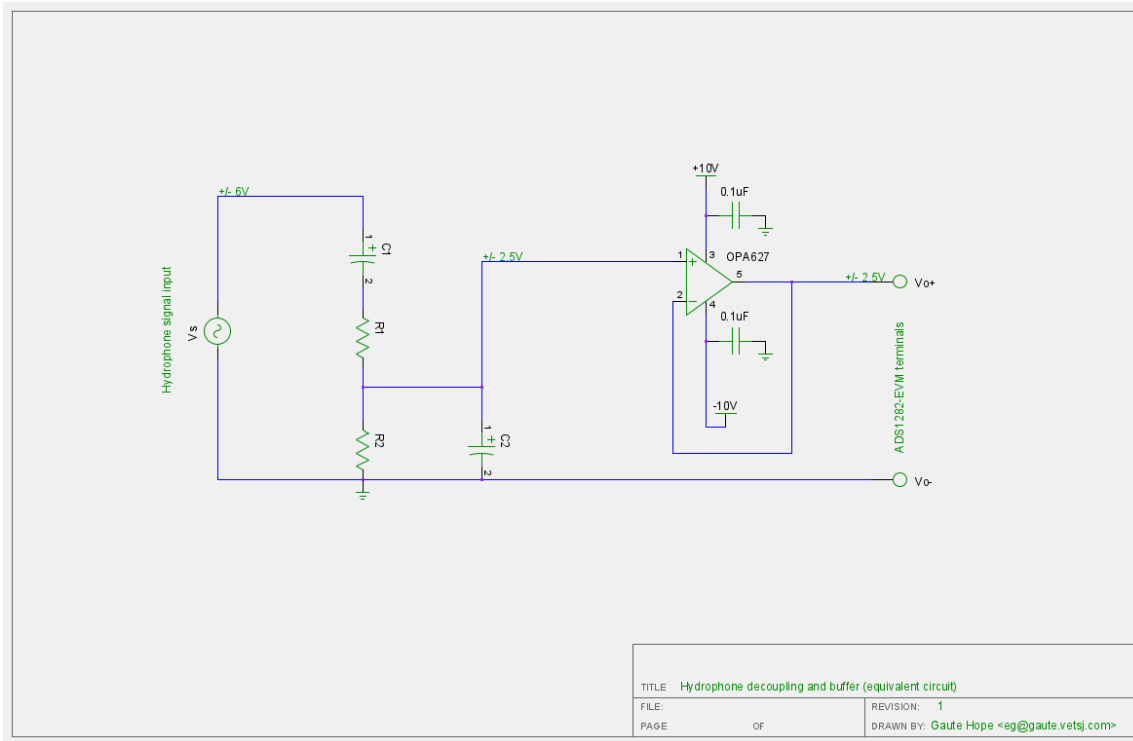


Figure A.2.3: Hydrophone decoupling and buffer (equivalent circuit)

Figure A.2.3 shows an equivalent circuit of the decoupled hydrophone input and buffering. The original circuit can be seen in the schema in figure A.2.1. Details can be found in section A.2.1.2.

A.2.2.1 Derivation of transfer function

The impedances of the circuit had the following values:

$$C_1 = 47\mu F$$

$$C_2 = 330pF$$

$$R_1 = 58.33k\Omega$$

$$R_2 = 41.67k\Omega$$

in analyzing the circuit, i_1 and i_2 represent the current loops passing through respectively left and right current loops. Using Kirchhoff's equation:

$$V_s = i_1(Z_{C_1} + Z_{R_1}) + (i_1 - i_2)Z_{R_2} \quad (\text{A.2.1})$$

$$0 = (i_2 - i_1)Z_{R_2} + i_2 \cdot Z_{C_2} \quad (\text{A.2.2})$$

V_s is the signal source, the hydrophone; V_o , output, is measured at the terminals T_+ and T_- .

$$V_o = i_2 Z_{C_2} \quad (\text{A.2.3})$$

$$H(s) = \frac{V_o}{V_s}, s = i\omega \quad (\text{A.2.4})$$

Solving for $H(s)$ gives:

$$H(s) = \frac{51951s}{(s + 1.2470 \times 10^5)(s + 0.2128)} \quad (\text{A.2.5})$$

A Bode plot of the transfer function of the decoupling and buffer stage is shown in figure A.2.4 below.

A.2.2.2 Analysis

The frequency band of interest reached from periods of 20 s (0.05 Hz) to approximately 100 Hz. The analog input part as well as the configuration of the analog-digital converter had

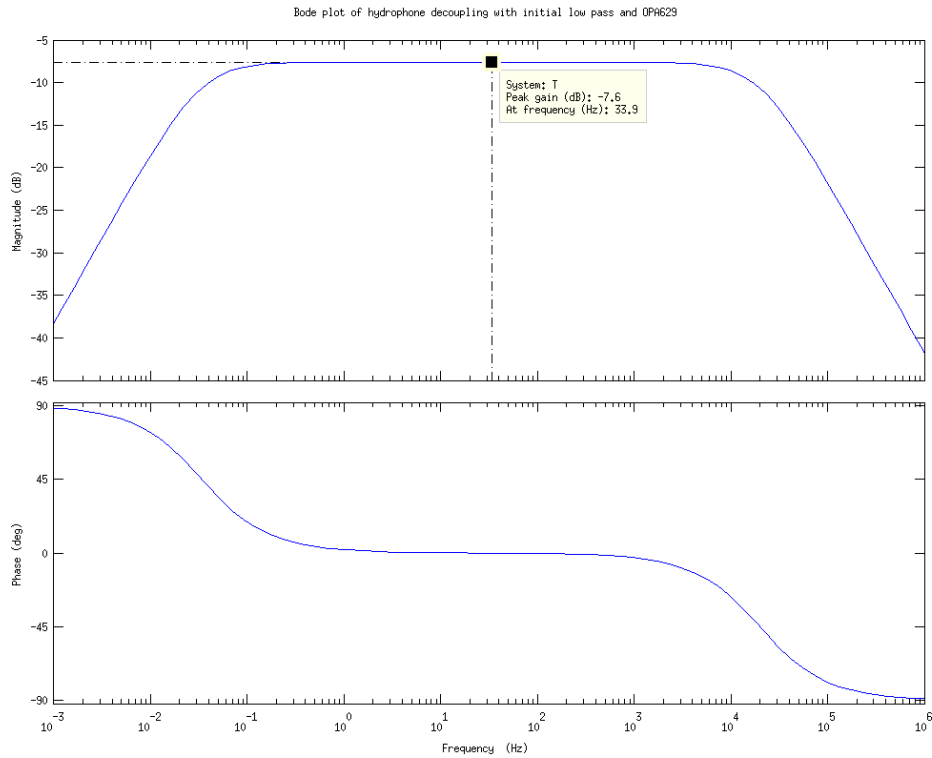


Figure A.2.4: Bode plot of the transfer function for the buffer stage (equation A.2.5), showing peak response at 33.9 Hz.

been configured as best and simple as possible to record signal within this frequency band.

Decoupling and analog high pass filter The transfer function is a bandpass filter in which the suggested decoupling created a high-pass filter with a corner frequency of $f_{HP} = 0.0339$ Hz (a period of 29.4985 s).

Low pass filter and operational amplifier To avoid aliasing due to the speed of the op-amps in the signal path, the OPA627 (see Burr-Brown (1989) and figure A.2.3), which acted as a buffer with unity gain, and then the OPA1632 (Texas Instruments, 2010) at the input terminals of the ADS1282EVM Texas Instruments (2009). An additional low pass

stage was added with a corner frequency of $f_{LP_1} = 17.189$ kHz. The speed of the op-amps is of the order of MHz so this corner frequency should be well within their capabilities.

OPA1632 The OPA1632 Texas Instruments (2010) was set up with a 1 nF capacitor in its feedback loop on the ADS1282EVM Texas Instruments (2009). This low passes the signal with a cut off frequency of $f_{LP_2} = 151.99$ kHz. Its gain bandwidth product was specified to be 180 MHz. Since the gain is 1 and the load is large it should have a well behaved and near ideal response. The OPA1632-setups simplified transfer function is (Texas Instruments, 2002):

$$H_{OPA1632}(s) = \frac{9.551 \times 10^5}{(s + 9.551 \times 10^5)} \quad (\text{A.2.6})$$

OPA627 The OPA627 was used as a buffer with gain 1 to provide a high impedance input and low impedance output. It has a gain bandwidth product of 16 MHz Burr-Brown (1989). With the first low pass filter, f_{LP_1} , well below this it should be able to relay the signal without alias. The transfer function would simply be 1 for this step. It was important that the OPA627 had well mounted bypass capacitors to avoid oscillations when configured for this low gain. A buffer designed for unity gain, like the OPA633 Burr-Brown (1993) or BUF634 Burr-Brown (1996) could be good alternatives, but they use more power.

Analog-Digital Converter (ADC) The ADS1282EVM equipped its ADS1282 with a crystal with the recommended clock frequency of $f_{clk} = 4.096$ MHz (Texas Instruments, 2009). This resulted in a modulator output speed of $f_s = f_{clk}/4 = 1.024$ MHz (Texas Instruments, 2007). The Nyquist frequency is then:

$$f_{Nq} = 1.024 \times 10^6 / 2 = 512 \text{ kHz} \quad (\text{A.2.7})$$

Anti-alias filter The 10 nF capacitor used on the ADS1282EVM (Texas Instruments, 2009), resulted in a low-pass filter with an upper corner frequency of $f_{LP_3} = \frac{1}{2\pi \times 600 \times 10 \times 10^{-9}} = 26525.82$ Hz ².

²Equation (3), p.15, Texas Instruments (2007)

f_{LP_3} is thus well below f_{Nq} and any signal component above f_{LP_3} should be almost completely damped before it reached f_{Nq} , resulting in no or very small aliasing effects.

The following equation represents the upper low pass filter:

$$\begin{aligned} H_{UL}(s) &= \frac{1 \div 600 \times 10 \times 10^{-9}}{(s + 1 \div 600 \times 10 \times 10^{-9})} \\ &= \frac{1.667 \times 10^5}{(s + 1.667 \times 10^5)} \end{aligned} \quad (\text{A.2.8})$$

The complete analog transfer function is then:

$$H_a = \frac{8.2698 \times 10^{15}s}{(s + 9.551 \times 10^5) \times (s + 1.667 \times 10^5) \times (s + 1.247 \times 10^5) \times (s + 0.2128)} \quad (\text{A.2.9})$$

The frequency response is illustrated in figure 3.3.3 in the main thesis.

Output of decoupling and buffer stages The output of the hydrophone was scaled by $-7.6 \text{ dB} = 0.4169 \frac{V}{V}$ so that input was scaled from $\pm 6V$ to $\pm 2.5V$, $0.4169 \approx 5/12 = 0.4167$, which was the input range of the ADS1282EVM (Texas Instruments (2009) and Texas Instruments (2007)) in bipolar mode. The slightly inaccurate scaling is due to the standard available (high precision) resistor values.

The impulse response of the system (equation A.2.9) is plotted in figure A.2.5, the step response is plotted in figure A.2.6.

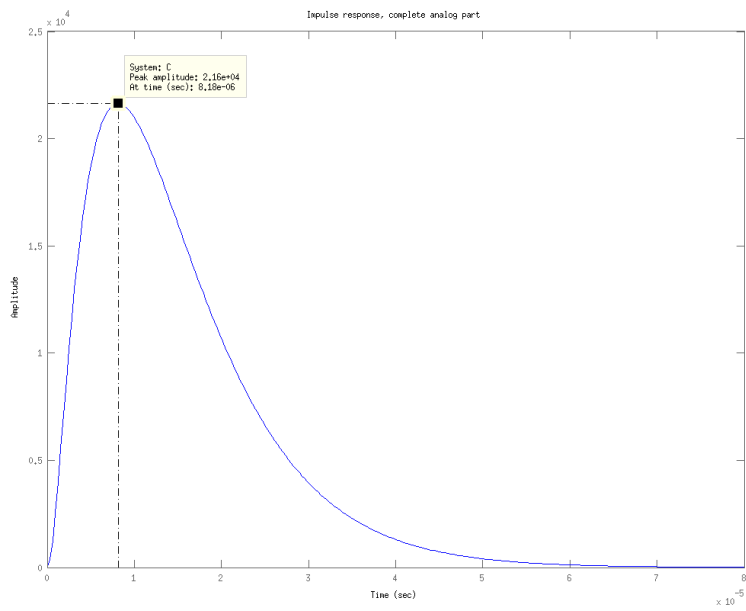


Figure A.2.5: Impulse response of complete analog system, equation (A.2.9).

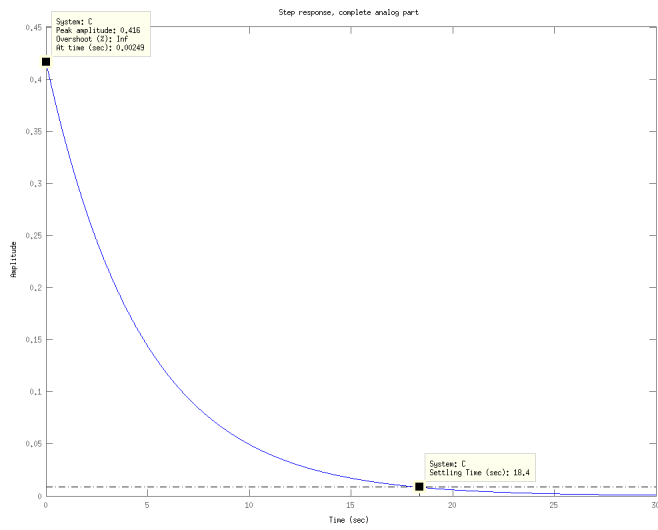


Figure A.2.6: Step response of complete analog system, equation (A.2.9).

A section zoomed in on the first tens of microseconds of the step response is plotted in figure A.2.7:

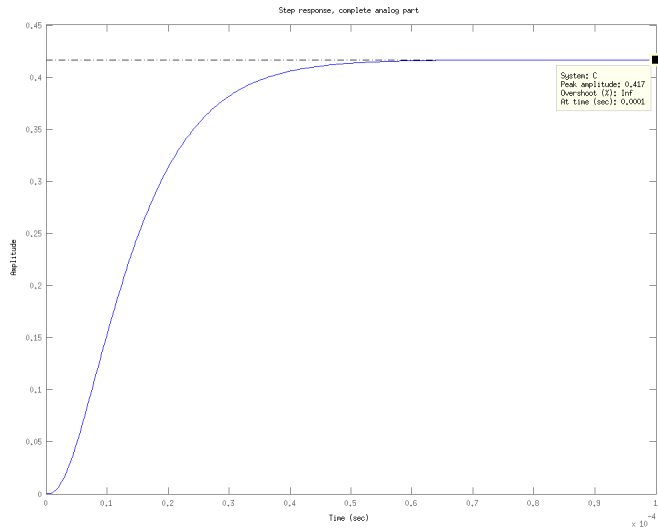


Figure A.2.7: Zoomed in step response of complete analog system, equation (A.2.9).

Stability The system, $H(s)$ from equation (A.2.9) is passive and has all its poles in the left half plane and it is stable. A pole-zero map is plotted in figure (A.2.8).

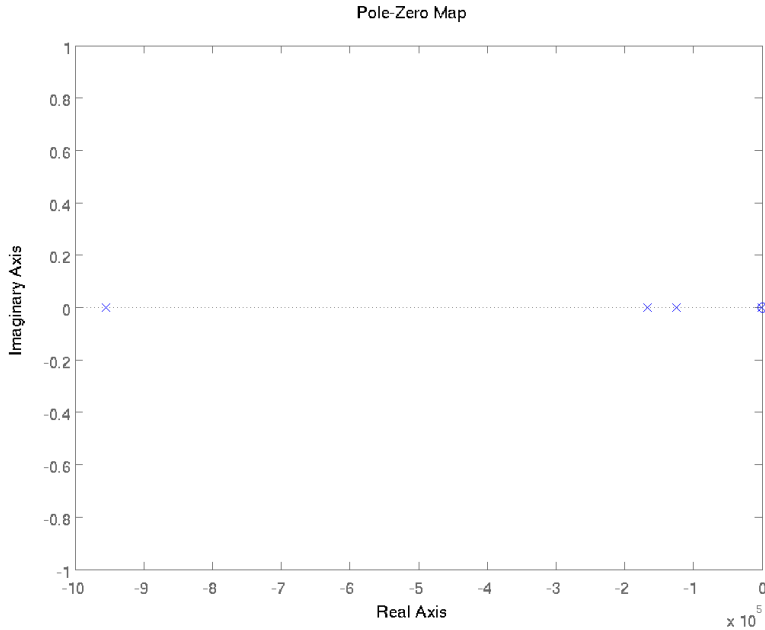


Figure A.2.8: Pole Zero map of the transfer function $H(s)$ from equation (A.2.9).

Attenuation at Nyquist frequency

The attenuation at the Nyquist frequency, 512 kHz, equation (A.2.7) using (A.2.9), was evaluated to be:

$$\begin{aligned} |H_a(512 \times 10^3 \times 2\pi)| &= 0.00023763 \\ &= -72.4821 \text{ dB} \end{aligned} \quad (\text{A.2.10})$$

The theoretical maximum dynamic range was specified to be 130 dB³. But before reaching the frequencies of any signals not attenuated at (A.2.10) that wraps around to the 125 Hz passband of the digital filter (section A.2.2.3) they would be additionally attenuated. The next periods would be increasingly attenuated.

Depending on the noise spectra only a fraction of the noise would be in this passband. Any tones or oscillations from the electrical components or environment were, although unlikely to be entirely in this passband, the biggest cause of concern. Other noise was more likely

³Table 1, p. 13, Texas Instruments (2007)

to have a flatter spectrum, where only a fraction of its energy would wrap into the 125 Hz passband.

A.2.2.3 Digital filter

The ADS1282 was configured to digitally filter the decimation output so that the final output signal of 250 Hz contains no alias below the input Nyquist sample rate (equation (A.2.7)). The built-in sinc and FIR filters were activated (Texas Instruments, 2007). This provided more than 140 dB of attenuation above the Nyquist frequency of the output sample rate Texas Instruments (2007).

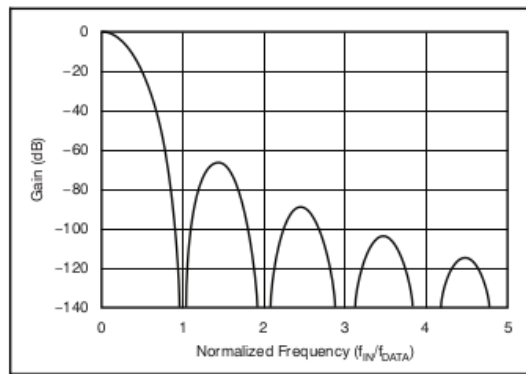


Figure A.2.9: Sinc filter response (from Texas Instruments, 2007).

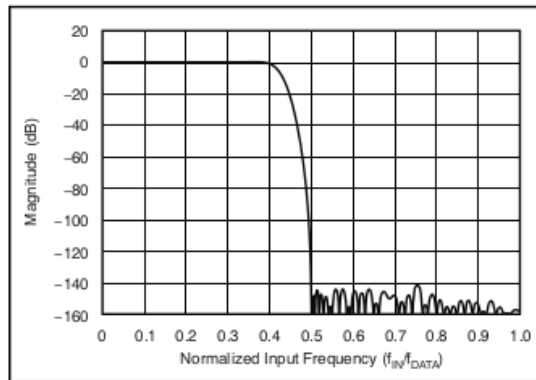


Figure A.2.10: FIR filter response (from Texas Instruments, 2007).

Figure A.2.9 shows the response of the sinc filter. Figure A.2.10 shows the response of the FIR filter.

High Pass Filter (HPF) A high pass filter with corner period as close to 20 seconds as possible was applied. The built in IIR HPF was set according to p. 22 in (Texas Instruments, 2007):

$$HPF[1 : 0] = 65,536 \times \left[1 - \sqrt{1 - 2 \frac{\cos(\omega_n) + \sin(\omega_n) - 1}{\cos(\omega_n)}} \right] \quad (\text{A.2.11})$$

with:

$$\omega_n = 2\pi f_{HP} / f_{DATA} \quad (\text{A.2.12})$$

A corner frequency $f_{HP} = 1/20 = 0.05$ Hz gives an $\omega_n = 0.001256637$ normalized radians. And an $HPF[1 : 0] = 82.3550098$ truncated to $HPF[1 : 0] = 82_{10} = 52_{16}$.

Analog to digital conversion The output of the ADS1282 was 32 bit integers, with a range of $[-2^{31}, 2^{31} - 1]$. The transfer function for the conversion can, for the frequency range 0.05 Hz to 250 Hz, be simplified to:

$$H_D = \frac{2^{32}}{5} \frac{\text{counts}}{\text{V}} \quad (\text{A.2.13})$$

Otherwise it was assumed, on the basis of the analog and digital filters, to be zero.

A.2.2.4 Hydrophone characteristics

The hydrophone used, Benthos AQ-18, was specified to have a flat frequency response within ± 1.5 dB at the band 1 Hz - 10 kHz Teledyne Benthos (2012b), with a sensitivity of -171 dBv re 1 uPa at 20° C.

The frequency response for the AQ-18 is plotted in figure A.2.11.

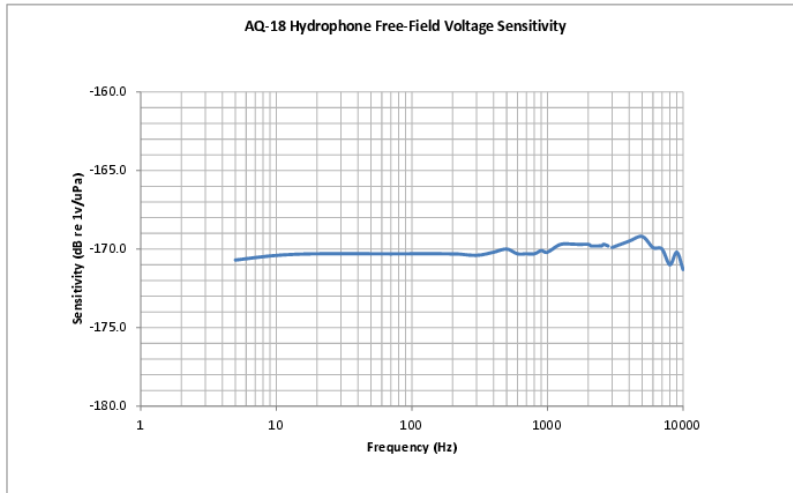


Figure A.2.11: Frequency response plot of hydrophone (from 7 Hz, the hydrophone is however specified from 1 Hz), AQ-18, figure from Benthos (Teledyne Benthos, 2012c).

A simplified transfer function for the hydrophone in the flat band (1 Hz - 10 kHz):

$$H_{Hyd} = -171 \text{ dBv re } 1 \text{ uPa} = 10^{8.55} \frac{\text{V}}{\text{uPa}} \quad (\text{A.2.14})$$

A.2.3 Digital components

A.2.3.1 Main board with Central Processing Unit

As can be seen from the wiring diagram (figure A.2.1) the different devices were all connected to the main board, an *Olimexino STM32 H103* (Olmexino Ltd., 2011). At its core it was run by a STM32 ARM7 (STMicroelectronics, 2012) processor of 72 MHz, with 168 KB of flash memory and 20 KB of RAM. The board was equipped with a SD card slot which was accessible via the STM32 hardware SPI. The board was designed for prototyping, it

is industrial standard, highly power efficient and had sufficient pins and features necessary for driving and controlling the necessary devices for the buoy, logging data continuously as well as accurately time it and transmitting the stored data back over the network. It is compatible with the Leaflabs libmaple library (LeafLabs, 2012) which provided a more accessible layer on top of the STM32 internals. The board operating system was programmed in C++ for the GCC ARM compiler. There was limited flash memory for storing the operating system and RAM for working with data. However the 72 MHz CPU is capable of handling the data throughput fast enough to avoid reaching the memory limit. Careful programming and strict size optimization have kept memory usage at a minimum and made it possible to fit all drivers and the desired functionality on the board.

A.2.3.2 GPS

An *EM-406A* based on the *SiRF III* GPS device was used. This was interfaced with USART and a pulse-per-second (PPS) with a accuracy of up to $1 \mu s$ (GlobalSat, 2012).

A.2.3.3 Radio (RF)

The wireless communication was done through a Synapse Wireless setup using the Synapse RF200 units (Synapse Wireless, 2011). The Synapse SNAP network had a built-in mesh network protocol and the devices could be interfaced with USART and GPIO pins. The RF200 was programmed with a Python-like language (“snappy”). The RF200 was programmed so that it remotely, from the central logging point, could be activated, have its transmission speed adjusted (higher speed requires better signal), be reset, be programmed and reset the main board using a GPIO output connected to the hard reset pin of the Olimexino STM32 H103.

The mesh network setup allowed the transmitted messages to follow any path along the nodes to its destination (generally the central logging point). In our setup with the nodes spread out in a triangle this did not provide a great advantage, but for future setups (multi-layered arrays or line setups) this would greatly improve network connectivity.

The RF200, when in active mode, passed communication between the Olimexino main board and the central logging point, any further protocol was implemented on the Olimexino. The

messages are based on ASCII telegrams, but data (recorded seismic trace) are transmitted in binary.

A.2.3.4 AD converter

The ADS1282EVM exposes the SPI interface of the ADS1282 as well as some trivial on-board circuits (interfaced over an I_2C bus) that needed to be configured to do the hardware configuration of the ADS1282 (bipolar, hard reset, power). The main board configured sample rate and filters and read the ADS1282. A DRDY (data ready) signal line was pulled down (logical low) when a new sample was ready. The sample could then be read using a SPI protocol (Texas Instruments, 2007).

A.2.3.5 SD card

The on-board SD card slot on the Olimexino STM32 H103 could be interfaced with one of the hardware SPIs. The card may then be used in SPI mode (SD mode is faster, but is more complex and unavailable on this slot). The SD card was formatted with an FAT32 file system and a FAT32 driver (slightly modified from the Maple SdFat library by Vreeland (2013), which in turn was a port of the Arduino SdFat library by Greiman (2013)).

A.2.3.6 Pin map

Table A.2 shows the pin and wire mapping for the Olimexino STM32 H103 main board to the other components, as well as power requirements and the jumper and switch configuration.

Olimexino pin map

| Olimexino | | | |
|-----------------------------|-----------------|---------------------------|---|
| GND | DGND | | |
| Vin | +12V | | |
| RST | Reset | | 20 RF200, GPIO18 Active LOW, break out to shield and to RF200 |
| | | | |
| RF200 | | | |
| Pin | Pin name | Pin | Pin name |
| GPIO8 | TX (XBTX) | 8.1_RX | |
| GPIO7 | RX (XBRX) | 7.1_TX | |
| GPIO18 [20] | RST | Reset | |
| Vdd | +3.3V | | |
| GND | DGND | | |
| | | | |
| GPS | | | |
| Pin | Pin name | Pin | Pin name |
| 1, Black | DGND | | |
| 2, White | +5V | | |
| 3, Yellow | RX | NC | |
| 4, Blue | TX | 0_2_RX | 5V tolerant |
| 5, Red | DGND | | |
| 6, Green | PPS | 2 Interrupt, EXTI0 | 5V tolerant |
| | | | EXTI: D2, D15, D27 |
| | | | |
| SD | | | |
| Pin | Pin name | Pin | Pin name |
| MOSI | | 33.2_MISO | 5V-tolerant |
| MISO | | 34.2_MOSI | |
| SS | | 25 | |
| SCK | | 32.2_SCK | |
| | | | Onboard |
| ADS1282EVM | | | |
| Pin | Pin name | Pin | Pin name |
| J5.9 | nDRDY | 4 Interrupt, EXTI5 | |
| | | | EXTI: D4, D13, D20 |
| J5.3 | SCLK | 12 | |
| J5.11 | DIN | 10 | |
| J5.13 | DOUT | 11 | |
| J5.16 | SCL | 5.1_SCL | Pullup to 3.3V |
| J5.20 | SDA | 9.1_SDA | Pullup to 3.3V |
| | | | I2C |
| <i>Analog inputs</i> | | | |
| J6.1 | A1N | Vref | TLE2426 |
| J6.2 | A1P | Vs | Opamp output |
| | | | Agnd |
| | | | Agnd +/-2.5V |
| | | | |
| Power | | | |
| J8.1 | +10VA | +10VA | |
| J8.2 | -10VA | -10VA | |
| J8.3 | +5VA | +5VD | (max. +5V) (min. -10V) |
| J8.4 | -5VA | -6VA | |
| J8.5 | DGND | DGND | Is not used for |
| J8.6 | AGND | | Avss internally |
| J8.7 | +1.8VD | NC | |
| J8.8 | VD1 | NC | |
| J8.9 | +3.3V | +3.3V | Vcc (3.3V) |
| J8.10 | +5V | NC | |
| | | | Power-supply |
| <i>Jumpers and switches</i> | | | |

Side 1

Table A.2: Pin and wire map of components to the Olimexino STM32 H103 main board.

A.2.4 Construction and assembly

The buoy was built into a box with IP67 classification, waterproof to at least 1 m. Three cable holes are made (power, radio and hydrophone).

A.3 Operating system (OS)

The operating system was written in C++ using an object-oriented approach with one class for each component. A main class set up the other classes and run the main loop which executes the iterations of the components on each run. Sampling and GPS timing is interrupt driven and the routines are run almost instantly when a new sample is ready or a new GPS time is ready. The other less critical tasks are checked at each main loop so that the data queue is stored on the SD card and emptied, radio communication is parsed or a new position is calculated.

The critical tasks (checking whether the queue was full) is run more often during routines that can take some time (e.g. transferring a batch over the wireless network). A layout of the system hierarchy is shown in figure 3.3.2, a more detailed description of the OS is given in the main thesis in the section 3.3.

A.3.1 Storage

A FAT32 file system implementation (Vreeland, 2013) working with the hardware communication interface (SPI) available on the Olimexino was used. The file format and file layout are described in appendix B.

A.4 Positioning and timing (GPS)

All timing was based on the GPS unit (*EM-406A*). The GPS provided the OS with time and position information through ASCII telegrams over a serial USART interface. A PPS (pulse-per-second) signal was emitted and attached to an interrupt handler in the OS. The $1 \mu\text{s}$ accuracy of the GPS represents the limit for how good the timing accuracy for the references could be. The PPS pulse was dependant on a good enough GPS fix, which should not be a problem in the open air in the arctic. Timing and position status were stored along with the samples with the status flags: HAS_TIME, POSITION, HAS_SYNC and HAS_SYNC_REFERENCE.

A.4.1 Time representation

The time is represented as UNIX time (seconds since the UNIX epoch 1 Jan 1970). The GPS time was used directly and *no* additional leap seconds were added. When needed the time was represented as microseconds since the UNIX epoch, i.e. for the batch reference. All these operations require 64 bit wide unsigned integers. This is the same type as the *hptime_t* type used in the miniSEED specification (Trabant, 2012).

A.4.2 Determining time

The current second was determined using the following steps (implemented in buoy/gps.cpp):

1. Receive time and date telegram (and position)
 - (a) Disable PPS interrupt handler
 - (b) Calculate seconds since UNIX epoch (1 Jan 1970)
 - (c) Enable PPS interrupt handler
2. Receive PPS interrupt
 - (a) Increment second - a reference is available.
 - (b) Record output of *micros()*, the internal CPU time in microseconds, this is called the *microdelta*.

To get a time resolution of microsecond accuracy (ignoring CPU clock drift) append the delta of a new call to *micros()* and the value stored in *microdelta* (at the time of the PPS interrupt) to the reference second (set at the time of the PPS interrupt).

A.4.2.1 Assumptions

1. When time and date is fixed the next PPS interrupt is for the next second, otherwise the time would already also be one second later.

2. There will be a good enough fix, under normal conditions, for the PPS signal often enough that *micros()* will not overflow and cause a backwards jump in time before a new reference has been set.
3. There cannot be a PPS pulse without a valid time and date.

A.4.3 Determining a new reference

A reference is used at each batch of 1024 samples, all the samples are timed relative to this assuming that the frequency (250 Hz) is constant. Every time there is a PPS interrupt a new reference is made available with a fresh *microdelta*. The continuously refreshed reference is not used before a new batch is started. With a batch length of 1024 samples and a sample rate of 250 Hz it takes approximately 4 seconds before it is rotated (implemented in buoy/ads1282.cpp and buoy/gps.cpp).

A.4.4 Accuracy

The drift of the CPU clock is bounded by the CPU crystal accuracy and drift as well as a systematic error due to the CPU instructions that need to be done to get the time (note that the output of *micros()* does not change while handling an interrupt). The C++ instructions are on the order of 10s of lines, with a CPU running at 72 MHz this should be fairly insignificant. Any drift of the crystal used on the ADS1282EVM may also cause a drift in the sampling frequency. The time will however be reset at each reference point with the batch beginning, roughly every 4 seconds.

A.5 Communication and network

A.5.1 Central logging point

The central logging point consisted of a regular Linux laptop connected via USB to an RF200. The RF200 radio unit was programmed as a counterpart to the radio units on the stations. It could address and adjust the speed of the other nodes, it was controlled by the logging program on the laptop. When a unit has been addressed further communication is

relayed to the logging program and the system running on the Olimexino on the current station.

The logging point looped through the active stations trying to retrieve status and position, and if configured, data. It kept track of what data had already been received and loaded any missing chunks of batches or data files from the buoys. The Python program exposes the current state through a local network protocol so that the logging server could be controlled asynchronously and several buoys could be monitored simultaneously. Figure A.5.1 shows a typical session with the server receiving data, a client monitoring and MATLAB showing a trace of the received data.

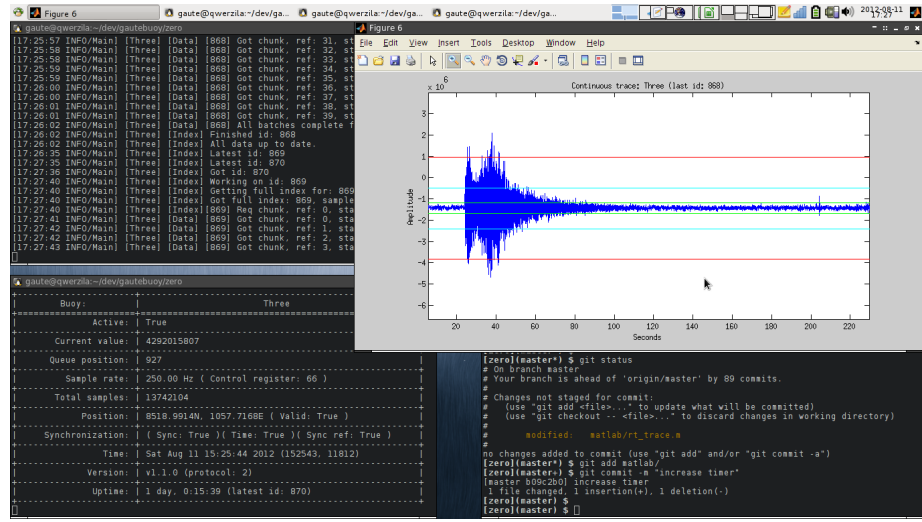


Figure A.5.1: Screenshot of central logging point server, a client monitoring one buoy and MATLAB showing data as it is received.

A.5.2 Network Protocol

Most of the protocol was implemented on the main board, but addressing, speed control and hard reset were implemented on the RF unit.

Once a connection had been established a direct transparent link was set up between the controlling software and the main board and further communication were handled there.

The table A.3 shows an overview of the messages which make up the protocol.

| Buoy, receive (central, transmit) | | | | |
|--|--------------|---|-----------------|-------------------|
| <i>Command</i> | <i>Token</i> | <i>Arguments</i> | | |
| GETSTATUS | GS | | | |
| GETINFO | GIF | | | |
| GETIDS | GIDS | id | | |
| GETLASTID | GLID | | | |
| GETBATCH | GB | id | reference no | start (sample) |
| | | length (samples) | | |
| Buoy, transmit (central, receive) | | | | |
| <i>Command</i> | <i>Token</i> | <i>Values</i> | | |
| AD status | AD,S | queue position | batch fill time | current value |
| GPS status | GPS,S | last type | received tlg. | latitude |
| | | N/S | longitude | E/W |
| | | time [s] | time | date |
| | | valid | HAS_TIME | HAS_SYNC |
| | | HAS_SYNC_REF | uptime [ms] | |
| INFO | I | bouy id | bouy version | protocol version |
| | | store version | | |
| LAST ID | LID | current id | | |
| INDEX (header) | IND | id | store version | samples |
| | | no. of ref | sd lag flag | |
| <i>GETBATCH</i> | | | | |
| Start batch | AD,D | id | reference no | start (sample) |
| | | length | reference (s) | reference status |
| | | latitude | longitude | checksum (32 bit) |
| Start of data | \$ | Binary transfer | | |
| End of data | AD,DE | Checksum | (8 bit) | |
| | | | | |
| <i>ERROR</i> | ERR | bouy id | error code | |
| Error codes: | | | | |
| E_CONFIRM | 0 | Not used | | |
| E_BADCOMMAND | 1 | Bad arguments have been given or the command cannot be executed | | |
| E_UNKNOWNCOMMAND | 2 | Command unknown | | |
| E_SDUNAVAILABLE | 3 | The SD card is not available | | |
| E_NOSUCHID | 4 | The requested ID does not exist | | |
| E_NOSUCHREF | 5 | The requested reference does not exist | | |
| E_NOSUCHSAMPLE | 6 | The sample does not exist, the data file does not contain enough samples | | |
| E_NOSUCHDAT | 7 | The DAT file does not exist or cannot be opened | | |
| E_BADDAT | 8 | There was an error reading and sending DAT file | | |
| E_SDLAG | 9 | SD card could not write queue fast enough, sample may be lost | | |
| E_MAXIDREACHED | 10 | The highest ID has been reached, no more files can be stored on the SD Card | | |

Table A.3: Network protocol telegrams

Appendix B

File Format

B.1 Data structure and file format

There are two file formats, one for storing data on the buoy and one for the central logging point. The versions are currently **10 for buoy storage (DAT)** and **3 for central storage (DTT)**. The formats have been designed to allow quick writing and sequential storage, with numerous checksums and files to detect data corruption and avoid loss of data in case one file should be corrupted.

B.1.1 Entities

The data consists of:

1. Sample: Values returned from AD converter (32 bit)
2. Timestamps
3. Position
4. Status (Validity of timing and position)

The formats are designed to represent these entities.

B.1.2 Structure

The data is organized in IDs with a number of batches, each batch has a reference and a set of corresponding values. In this section the terms reference and batch are used interchangeably.

Store

| | |
|----|--------------|
| ID | 1 |
| | Reference 0 |
| | Reference 1 |
| | Sample 0 |
| | Sample 1 |
| | ... |
| | Sample 1023 |
| | Reference 2 |
| | ... |
| | Reference 39 |
| ID | 2 |
| | ... |
| ID | 3 |
| | ... |
| | ... |
| ID | <i>MAXID</i> |

Table B.1: Store structure

There is one set of data and an index file for each ID, the index file contains information about the number of batches (references) and samples. The data file contains the references and the samples. The index acts as a header to the data file with general information and status. Status and information that changes with each batch or reference are stored along with the samples in the data files.

B.1.2.1 Index

The index contains:

1. Version of file format (incremented with buoy updates even when the format stays the same)
2. ID
3. Sample length (always 4 bytes, 32 bits)
4. Number of samples (batch size \times max references)
5. Number of samples per reference (batch size, 1024)
6. Number of references (40)
7. Flag indicating whether there was an error with writing samples fast enough to card

B.1.2.2 Reference: Timing, position and status

Each reference determines the position and status as well as a time reference for its batch of samples. That means that there is not recorded a position, status and timestamp, for each sample - but for a predefined number of samples. The time of each sample is calculated from the reference and the sample rate. The batch size is chosen based on the desired resolution of timestamps and position fixes and limitations of memory of the CPU unit. It is put to 1024 samples per batch, which results in little drift between each reference and provides frequent positioning at every $1024/250\text{Hz} \approx 4\text{s}$.

The time is represented as microseconds since the UNIX epoch (1970-1-1 00:00:00). This is the same as the high precision time format (hptime_t) defined by MiniSEED (Trabant, 2012).

As the data is sampled a 32-bit checksum is calculated the moment a sample is read from the AD unit for each batch. This is stored along with the reference and is used to check whether the stored data has not been corrupted. The checksum is the 32-bit XOR between all samples in the batch.

A reference has the following entities:

1. Reference number
2. Time reference: microseconds since Unix epoch
3. Position (longitude and latitude)
4. Status
5. Checksum

Both formats use this structure, on the buoy's local storage it is stored in the root folder of the SD card and on the central it is stored in a folder dedicated to each buoy.

B.1.2.3 Status

The status is a 16-bit wide unsigned integer with bits set for different conditions, the bit is set if the specified function is working with a optimal status of 15 (0b1111), these are defined in buoy/gps.h:

| Bit | Flag |
|--------|--------------------|
| 0b0 | NOTHING |
| 0b1 | HAS_TIME |
| 0b10 | HAS_SYNC |
| 0b100 | HAS_SYNC_REFERENCE |
| 0b1000 | POSITION |

Table B.2: Status flag bit mapping

NOTHING No flags set.

HAS_TIME A valid time is provided by the GPS unit.

HAS_SYNC A PPS signal is sent and the timing can be determined accurately.

HAS_SYNC_REFERENCE The reference in use was determined at a time when there was a PPS signal available. This can remain true after both time and sync is lost and the accuracy will deteriorate with the drift of the CPU clock.

POSITION The GPS is delivering a valid position fix. This will be true when HAS_TIME is true.

B.1.2.4 Sample

The sample is 32 bits wide and is an integer stored as two's complement. The least significant bit (LSB) indicates whether the full scale range was exceeded and the output has been clipped. If the value is at its maximum and the LSB is set (1) the output has been clipped, if the value is at its minimum and LSB is unset (0) the output has been clipped (Texas Instruments, 2007). For a correct interpretation of the sample the LSB should be set to 0 before attempting to read it as a 32 bit integer.

Throughout processing and storage the values are represented with 32 bits, even though the least significant bit may be cleared after having converted the values to signed integers.

B.1.3 Formats

Since the files are stored in the DAT format and then read either directly from the SD card or sent over the network the DAT format is the master format for the DTT format. The settings for size or batch length in the DAT will be seen in the DTT file.

B.1.3.1 Binary format: DAT

The binary format uses the extension DAT for its data files and IND for its index files. The buoy chooses the next free ID number on start up and continues to pick the next free ID when a data file is filled. This puts a limit at the maximum number of IDs since the FAT32 file system has a limit on the maximum number of characters.

Endianness The buoy runs on an ARM7 CPU and values are stored in little endian byte format (least significant byte first).

Version The version number, stored in the index, is updated whenever there is an upgrade of the buoy so that the data quality or integrity changes. The buoy version is not stored.

Implementation The implementation and latest version of the DAT file format is to be found in the source: *bouy/store.h* and *bouy/store.cpp*.

Limit of IDs The SD card is formatted using the FAT32 file system and the file names are limited by the 8.3 format, that leaves 8 digits for the ID number and a maximum ID of $10^8 - 1 = 99999999$. With a maximum number of 40 references (batches) per data file and a batch size of 1024 values there will be 164 seconds of recording in each file. This means that for 14 days of continuous recording 7383 IDs are needed, in other words well below the limit (see the data capacity budget in table B.7).

Data file size The number of references (batches) and the data file size has been chosen to be in this order so that in case of data corruption in one file not too many samples will be lost, but still to be balanced against the overhead of more IDs and metadata. The more specific a batch of samples can be addressed the easier it is to retrieve them with the minimum disturbance of other batches or IDs. To avoid any interference with the current logging a data file is not transmitted before it is closed. This means that there is a lag equal to the length of the data file when watching the data in real time. The chosen length is a reasonable compromise between these.

Structure: Index The index file for ID is named *ID.IND* and is written when a data file is full, the file structure is:

| Start | Field | Type | Size |
|-------|---------------------|----------|-----------|
| 0 | Version | uint16_t | 2 |
| 2 | Id | uint32_t | 4 |
| 6 | Sample length | uint16_t | 2 |
| 8 | No of samples | uint32_t | 4 |
| 12 | Batch size | uint32_t | 4 |
| 16 | No of references | uint32_t | 4 |
| 20 | SD lag flag | uint8_t | 1 |
| | Total length | | 21 |

Table B.3: Binary index file, fields, start and size are given in bytes.

Structure: Data file The data file is made up of batches, consisting of first one reference then a sequence of samples. The batches are concatenated after each other without spacing as described in table B.1. The structure of the reference is:

| Start | Field | Type | Size |
|-------|---------------------|----------|-----------|
| 0 | Padding | 0 | 12 |
| 12 | Reference id | uint32_t | 4 |
| 16 | Time (reference) | uint64_t | 8 |
| 24 | Status | uint32_t | 4 |
| 28 | Latitude | char[12] | 12 |
| 40 | Longitude | char[12] | 12 |
| 52 | Checksum | uint32_t | 4 |
| 56 | Padding | 0 | 12 |
| | Total length | | 68 |

Table B.4: Binary reference, fields, start and size are given in bytes.

The reference is padded with zeros ($3 \times$ sample length = 12) in both ends so that it will be easier to recover parts of a corrupt data file as well as making it possible to detect a reference when none is expected. The reference id starts at 0 for each data file reaching up to 40 which is the number of batches before a data file is considered full.

Sample Each sample is an **uint32_t** with size 4.

Batch The structure of one batch is given in table B.5:

| Start | Field | Count | Size |
|-------|---------------------|-------|-------------|
| 0 | Reference | 1 | 68 |
| 68 | Samples | 1024 | 4096 |
| | Total length | | 4164 |

Table B.5: Binary batch, fields, start and size are given in bytes.

A data file is given as shown in table B.6:

| Start | Field | Count | Size |
|--------------|---------------------|--------------|---------------|
| 0 | Reference 0 | 1 | 68 |
| 68 | Samples | 1024 | 4096 |
| 4164 | Reference 1 | 1 | 68 |
| 4232 | Samples | 1024 | 4096 |
| ... | ... | ... | ... |
| 162396 | Reference 39 | 1 | 68 |
| 162464 | Samples | 1024 | 4096 |
| | Total length | | 166560 |

Table B.6: Binary data file, fields, start and size are given in bytes.

B.1.3.2 ASCII format: DTT

The ASCII format uses the extension DTT for its data file and ITT for its index files, they are created by the central logger (Zero) as they are transmitted from the buoy. A file may be incompletely downloaded and still be readable. The index file stores a list of all references and tells how much of it has been downloaded (chunks) from the buoy. Normally a whole reference is downloaded at the time, but the logger may be configured to download only parts (chunks) of the batch at the time. All line endings are UNIX line endings '\n'.

The logger is written in Python so the file format has been influenced by this. It is read directly by MATLAB scripts which plot and do simple processing and quality checks.

The central logger also keeps another index file, *indexes*, with a list of available IDs on the buoy and whether they are enabled (file exists and is valid on buoy).

The implementation and latest version is to be found in the source code: zero/data.py for index and data, and zero/index.py for the index of all available ids.

Structure: Index of ids This is a list with one line per id of the format:

ID,enabled

1. ID: integer value id
2. enabled: 'True' or 'False', whether this ID exists on the buoy.

Structure: Index There is one field per line with the following fields:

1. Local version (version of DTT format) (integer)
2. Remote version (version of DAT format on buoy) (integer)
3. ID (integer)
4. Number of samples (integer)
5. Number of references (integer)
6. HasFull, 'True' or 'False', whether a complete index has been received.
7. SD lag flag, 'True' or 'False', whether data could *not* be written fast enough to card.

After that there is one line for each received reference, with a comma separated list of the following fields:

1. Reference number (integer)
2. Reference timestamp (integer), microseconds since Unix epoch.
3. Status (integer)
4. Latitude (string)
5. Longitude (string)
6. Checksum (integer)
7. Line (integer), specifying where this batch starts in data file.
8. Comma separated list of finished chunks (integers, variable length)

If the chunk size equals the batch size, there is only one chunk per reference. Thus, if the reference (batch) has been retrieved there should be one '0' in the last comma separated list. There cannot be a chunk size greater than the batch size and the batch size must be a multiple of the chunk size.

Structure: Data file The data file is built up in a similar way as the binary data file, where all the batches follow each other. A batch consists of a reference followed by a sequence of samples, so that the timing of each sample can be determined from the previous reference.

The reference is one line of a comma separated list of the fields:

1. R (the character 'R' to indicate a reference)
2. Batch length (integer), value: 1024
3. Reference number (integer)
4. Reference timestamp (integer)
5. Status (integer)
6. Latitude (string)
7. Longitude (string)
8. Checksum (integer)

After this follows 1024 samples (integers), one on each line. The references are sorted in ascending order, but there may be missing references (batches) until the file is completely downloaded.

B.1.4 Data capacity budget

A data capacity budget for local storage is, table B.7:

| Entity | Size | | |
|---------------------------------|-------------|---------|-----------------------------|
| Sample | 4 | B | |
| Reference | 68 | B | |
| Index | 21 | B | |
| | | | |
| Quantities | # | | |
| Batch size, samples | 1024 | samples | |
| File size, samples | 40960 | samples | |
| References per file | 40 | | |
| Samples per seconds (frequency) | 250 | Hz | |
| | | | |
| File size | Size | | |
| Samples | 163840 | B | |
| References | 2720 | B | |
| Index | 21 | B | |
| Total size per file | 166581 | B | |
| | | | |
| Seconds per file | 163.84 | s | |
| Goal duration (14 days) | 1209600 | s | |
| Total storage needed | 1229836290 | B | |
| | 1172.2 | MiB | |
| Files needed | 7383 | | |
| MAX ID | 99999999 | | (limited by FAT filesystem) |

Table B.7: Local data capacity budget